The Effect of Stratification and Bathymetry on Internal Seiche Dynamics

by

Paul David Fricker

B.Sc. in Chemistry, Dalhousie University (1989)
M.Sc. in Physics, University of Toronto (1991)

Submitted to the Department of Civil and Environmental Engineering
in partial fulfillment of the requirements for the degree of

Doctor of Philosophy in Civil and Environmental Engineering

at the

MASSACHUSETTS INSTITUTE OF TECHNOLOGY

September 2000

Signature of Author .....
Department of Civil and Environmental Engineering
26 July 2000

Certified by .....
Heidi M. Nepf
Associate Professor, Civil and Environmental Engineering
Thesis Supervisor

Accepted by .....
Daniele Veneziano
Chairman, Department Committee on Graduate Students

The Effect of Stratification and Bathymetry on Internal Seiche Dynamics

by

Paul David Fricker

Submitted to the Department of Civil and Environmental Engineering
on 26 July 2000, in partial fulfillment of the
requirements for the degree of
Doctor of Philosophy in Civil and Environmental Engineering

Abstract

Internal seiches are basin-scale standing waves which oscillate within the body of a stratified lake or bay. In thermally stratified mid-latitude lakes, for which the surface-to-bed density difference is typically $\mathcal{O}\left(1 - 3\text{kg/m}^3\right)$ during summer, buoyancy within the water column supports relatively large amplitude waves, with horizontal and vertical fluid displacements as large as $\sim$10% of the lake dimensions, depending on the strength of wind forcing. In strongly-stratified lakes, seiching is often the only dynamic process occuring in the hypolimnion, since direct wind-driven motions are constrained to the epilimnion, and small-scale (i.e. progressive) internal waves cannot propagate outside the pycnocline. Internal seiches therefore provide the principal conduit for converting wind energy into boundary, hypolimnetic, and effective diapycnal mixing.

We begin by investigating the dependence of internal seiche structure (i.e., the velocity field) on lake bathymetry and stratification, using a two-dimensional linear, inviscid model to compute numerical seiche solutions for a series of idealized configurations. This is followed by an analysis of the fundamental seiche (V1H1) in the Upper Mystic Lake (UML; Winchester, Massachusetts), including a comparison of model results to field observations (thermistor chain temperature time series), and an assessment of the seasonal evolution of bed velocity distribution. We next evaluate the viscous damping of internal seiches by modifying the inviscid formulation with the addition of a benthic boundary layer flow. A generalized expression for the decay rate (α) is derived through a perturbation analysis using the solvability condition on the combined inviscid/first-perturbation-order system. The resulting α is equivalent in form to the integral of seiche kinetic energy at the bed (as for surface waves), weighted by an additional coefficient which accounts for effects of buoyancy and bathymetry. Comparison to other, physically-based derivation methods reveals that α can be interpreted equivalently as the rate of stress working by the seiche on the bed boundary. Finally, using numerical solutions for the three dominant seiches in the UML, we find that buoyancy effects generate roughly an order of magnitude increase in α for each mode. The estimated relative damping rates account for the apparent rapid decay of the fundamental (V1H1) seiche, and are consistent with the observed persistence of the dominant higher mode (V3H1). Buoyancy effects therefore appear to be an important factor governing seiche climate in the UML.

Thesis Supervisor: Heidi M. Nepf
Title: Associate Professor, Civil and Environmental Engineering

Acknowledgments

First I must thank my supervisor, Professor Heidi M. Nepf, for allowing me to freely explore new ideas and avenues of research, even though I couldn't always explain where they were leading. Heidi endured my enthusiasm for equations, and constantly reminded me that a clear, well-developed presentation of information is essential for communicating scientific research. I would also like to thank the members of my committee, Professor Harold F. Hemond (who was also my supervisor during my first year at MIT) and Professor Chiang C. Mei, for their input and support.

I am grateful for the help and friendship of my fellow students at the Parsons Lab; thanks go especially to Hrund Andradóttir, Chin-Hsien Wu, Laura DePaoli, Marco Ghisalberti, Brian White, Enrique Vivoni, David Senn, Daniel Pedersen, Susan Brown, Gordon Ruggaber, Frederic Chagnon, and all the others I will wish I had added later. A special badge of honor goes to those who survived helping me with field work. I would also like to thank my MIT friends-at-large, Karuna Mohindra, Sally Stiffler, Edmund Carlevale, Janni Moselsky, and Row Selman, as well as those who helped me remember the world outside MIT, Sanjeev Seereeram and Cecilia Mercado, Darren and Teresa Farmer, Phil Trowbridge and Laura Bonk, and my friends at home, George Xidos, Chris White, Phil Gunn, Susan Walsh, Emmanuel and Matina Xidos, Strat and Pat Poulos, Cyril and Peggy White, and John and Cathy Arab. I would also like to acknowledge Russell J. Boyd at Dalhousie University, for being a good scientist, and for making my first efforts in research so enjoyable and rewarding.

Above all, I thank my wife Kamla and my children Alexander and Kristina, for their love, and for the tremendous sacrifices they have made over the past few years. This thesis is truly a group effort. And finally, I thank my family, Aubrey, Joan and Mike Fricker, without whose love and support this work would not have been possible.

Contents

List of Figures

Chapter 1

Internal seiches

1.1 Introduction

Internal seiches are basin-scale standing waves which oscillate within the body of an enclosed or semi-enclosed stratified fluid. In thermally stratified mid-latitude lakes, for which the surface-to-bed density difference is typically $\mathcal{O}\left(1-3\mathrm{kg/m}^3\right)$ during summer, the buoyancy within the water column supports relatively large amplitude waves, with horizontal and vertical fluid displacements as large as $\sim \pm 5\%$ of the lake dimensions (see, for example, Roget *et al.* 1997, Münnich *et al.* 1992, Wiegand and Chamberlain 1987). Seiche-induced vertical motions have been shown to affect the distribution of both plankton (Gaedke and Schimmele 1991) and fish (Levy 1991). The (nearly) horizontal bed motions enhance sediment resuspension (Gloor *et al.* 1994, Pierson and Weyhenmeyer 1994, Shteinman *et al.* 1997) and the dissolution of nutrients and contaminants through pressure-driven porewater exchange. Experimental studies have shown that boundary mixing generates horizontal buoyancy-driven flows (Ivey and Corcos 1982, Phillips *et al.* 1986). This process also occurs in lakes, where homogenized fluid within the seiche-induced benthic boundary layer intrudes into the lake interior (Gloor *et al.* 1994, Goudsmit *et al.* 1997), thererby broadening the pycnocline and enhancing net vertical mixing. Internal seiches therefore provide a conduit for converting wind energy into boundary, hypolimnetic, and effective diapycnal mixing. In fact, in strongly-stratified lakes, internal seiching is essentially the only dynamic process occuring in the hypolimnion, since direct wind-driven motions are constrained to the epilimnion, and since small-scale (i.e. progressive) internal waves

cannot propagate outside the pycnocline.

In principle, the mathematical description of internal seiches is straightforward, since the linear formulation simply corresponds to a spatial boundary value problem. However, these eigensystems are difficult to solve in practice because the equation parameters (i.e. stratification, $\overline{\rho}(z)$) are not constant, and the spatial domain (bathymetry, $z = h(x, y)$) is not regular for real lakes. Analytical solutions can thus only be obtained for simple configurations, which, while adequate for illustrating the principal qualitative features of seiches, are not sufficiently accurate for quantitative analyses. Because of these analytical difficulties, all numerical models developed to date use a simplification or idealization of system configuration. A number of these models are discussed in Section 1.2.2. Throughout this thesis, solutions for longitudinal internal seiches are evaluated numerically using a two-dimensional stream function formulation, which allows longitudinal depth variation and non-uniform stratification. The complete three-dimensional problem, and some of the numerical difficulties associated with it, are outlined in Appendix C.2.

1.1.1 Thesis outline

We begin in the present chapter by reviewing some fundamental concepts, and some of the more popular models for describing and evaluating internal seiches. Each of the remaining chapters has either been published (Chapter 2) or prepared for journal submission (Chapters 3 and 4); the material is therefore presented very concisely, with supplementary information provided in Appendices to the thesis. Chapter 2 is an analysis of the dependence of seiche structure on bathymetry and stratification (i.e., the system configuration), with particular focus on bed velocity distribution. As discussed above, seiche solutions are computed numerically using a two-dimensional stream function formulation. A systematic investigation of seiches is performed using a series of idealized configurations, and the structure, decay, and seasonal variation of seiches in the Upper Mystic Lake (Winchester, Massachusetts) is explored.

Chapter 3 is an analysis of internal seiche damping due to viscous dissipation of energy in the benthic boundary-layer. A generalized expression for seiche decay rates (α) is derived through a perturbation analysis by applying a solvability condition. The mathematical analysis is augmented with an exploration of the underlying physics, revealing that α can equivalently

be derived using several physically-based arguments. The decay rate for internal seiches is similar to the homogeneous fluid result, but includes an additional coefficient which accounts for combined buoyancy and bathymetry effects. Damping rates for the fundamental seiche (i.e., V1H1; see Section 1.2.1) are computed for a series of ideal basins to explore the impact of buoyancy and bathymetry on decay. The boundary-layer structure implied by the analytical model is also explored.

Chapter 4 is an expansion of the analysis of decay and boundary-layer structure for longitudinal seiches. Model predictions of boundary-layer thickness are supported through comparison to recent field observations (Gloor *et al.* 2000). Numerical stream function solutions and decay rates are computed for the three dominant seiches in the Upper Mystic Lake. Results reveal that seiche damping (and therefore climate) in the lake is substantially affected by buoyancy. Predicted decay rates agree well with field temperature data observations.

1.2 Review of Literature and Methods

Surface seiches were first studied by the Swiss engineer de Duillier at Lake Geneva in 1730. In the 1870's, Forel (also at Lake Geneva) identified seiches as standing surface gravity waves, and provided the first theoretical description of the phenomenon (Forel 1876). At the beginning of this century, Chrystal (1905) investigated a series of analytical solutions for surface seiches in regularly-shaped basins. His results matched observations quite well for lakes with simple bathymetry, but broke down for more complex systems. Wedderburn began the study of internal seiching by extending Chrystal's analyses to two-layer systems (Wedderburn and Williams 1911, Wedderburn 1912, Wedderburn and Young 1915), but once again was restricted to simple bathymetries. Beginning with the Defant technique (Defant 1918, 1960), a wide range of numerical internal seiche models have been developed to improve the description of either stratification or bathymetry. (In fact, an improved model of one generally requires an oversimplification of the other.) The most widely-used internal seiche models are outlined in Section 1.2.2.

During the 1980's, field studies began to focus on the observation of higher mode internal seiches (which drove the development of more sophisticated models of stratification) and the

excitation of specific modes through resonance with wind forcing (see, for example, LaZerte 1980, Lemmin 1987, Wiegand and Chamberlain 1987, Münnich *et al.* 1992). The study of modal response has since evolved into a comprehensive investigation of seiche climate (Roget *et al.* 1997, Saggio and Imberger 1998). Numerous laboratory studies have probed seiche-related processes such as boundary and vertical mixing (Ivey and Corcos 1982, Ivey and Nokes 1989, Heinz *et al.* 1990) and internal wave breaking on slopes (Helfrich 1992, Slinn and Riley 1996). This research compliments the extensive body of field studies of seiche-induced resuspension and sediment transport (Sheng and Lick 1979, Hagatun and Eidsvik 1986, MacManus and Duck 1988, Evans 1994) and boundary mixing (Wüest and Gloor 1998, Gloor *et al.* 2000).

1.2.1 Background

The principal qualitative features of internal seiches can be described very easily using simple models such as the two-layer rectangular basin. We begin by reviewing some of the techniques which have traditionally been used to evaluate seiche solutions, begining with a slightly extended analysis of the rectangular basin model, in order to introduce some standard concepts and nomenclature. Later, however, we shall see that such overly-simplistic models are generally inadequate for a quantitative analysis of seiches.

Rectangular basin model

For a two-dimensional formulation (in (x,z)), the velocity field can be written in terms of a stream function $\psi(x,z)$, i.e., $(u,w) = (\partial\psi/\partial z, -\partial\psi/\partial x)$; see Appendix B.4. In a rectangular domain the 2D governing equation for longitudinal seiches (see (B.21) in Appendix B.4) is spatially separable;

$$\psi(x,z) = \chi(z)\sin kx \ , \qquad \overline{\rho}^{-1}\left(\overline{\rho}\chi'\right)' + \left(\frac{N^2}{\omega^2} - 1\right)k^2\chi = 0 \ , \tag{1.1}$$

with $\chi' \equiv d\chi/dz$. For a basin with depth H and length L, the horizontal wavenumber is $k \ (= k_{n_h}) = n_h \pi L^{-1}$, with $n_h = 1, 2, ...$ the mode number.

The first system we consider is the case of constant buoyancy frequency (N), which formally

corresponds to $\overline{\rho}(z) = \overline{\rho}(0)\exp(-N^2 z/g)$. The solution to (1.1) for this stratification is

$$\chi(z) = \left(\frac{\overline{\rho}(z)}{\overline{\rho}(0)}\right)^{-\frac{1}{2}} \sin mz \ ,$$

where $m \ (= m_{n_v}) = n_v \pi H^{-1}$, with vertical mode number $n_v = 1, 2, ...$ The dispersion relation for this system is

$$\frac{\omega^2}{N^2} = \frac{k^2}{k^2 + m^2 + \frac{N^4}{4g^2}} \approx \frac{k^2}{m^2} \ , \tag{1.2}$$

which provides the fundamental scaling $\omega \sim \mu N$ for the seiche frequency, with $\mu \equiv H/L$. This scaling holds for essentially all seiche systems (i.e., basins and stratification). Each mode $\psi_{n_h n_v} \sim \sin kx \sin mz$ can be distinctly labeled using the horizontal and vertical mode numbers, giving rise to the standard nomenclature $\mathrm{V}n_v\mathrm{H}n_h$, which is also used in non-rectangular basins.

After the constant-N case, the second common idealization for stratification is the two-discrete-layer system. This can be considered a limiting case of the continuous stratification model, corresponding to equation (1.1) with the hydrostatic approximation (i.e., $N^2 > \omega^2$) and the step density profile

$$\overline{\rho}(z) = \rho_1 + \triangle\rho\mathcal{H}(z - h_1) \quad \rightarrow \quad \overline{\rho}(z)\, N^2(z) = g\triangle\rho\delta(z - h_1) \ .$$

Here $\triangle\rho = \rho_2 - \rho_1$, h_1 is the upper layer thickness, and $\mathcal{H}(z)$ is the Heaviside function. The governing equation for this profile reduces to

$$\left(\overline{\rho}\chi'\right)' + g\triangle\rho\frac{k^2}{\omega_0^2}\delta(z - h_1)\chi = 0 \ . \tag{1.3}$$

Integrating (1.3) within each layer we find $\phi'(z) =$ constant, and therefore write

$$\chi(z) = \begin{cases} \chi(h_1)\dfrac{z}{h_1} & 0 < z < h_1 \\ \chi(h_1)\dfrac{H - z}{h_2} & h_1 < z < H \end{cases} \ , \tag{1.4}$$

with $h_2 = H - h_1$. Next, integrating (1.3) across the interface gives

$$\rho_2 \chi'(H) - \rho_1 \chi'(0) + g\triangle\rho \frac{k^2}{\omega_0^2} \chi(h_1) = 0 \ ,$$

which, along with (1.4) yields the dispersion relation $\omega_0^2 = k^2 g \triangle\rho h_1 h_2 / (\rho_2 h_1 + \rho_1 h_2)$.

The 2-layer analysis above is appealing because it provides a description of the fluid which is continuous over z. The same results can also be derived using a depth-averaged formulation, based on the (static + dynamic) pressure field $P_1 = g\rho_1 (z + \zeta_1 (x,t))$ in the upper layer and $P_2 = g\rho_1 (h_1 + \zeta_1 (x,t) - \zeta_2 (x,t)) + g\rho_2 (z - h_1 + \zeta_2 (x,t))$ in the lower, where ζ_1 and ζ_2 represent the free surface and interface displacements, respectively. This approach is somewhat more useful for describing the response of the system to wind forcing and friction. Placing P_1 and P_2 into depth-averaged (linear) continuity and momentum equations gives

$$\frac{\partial}{\partial t}(\zeta_1 - \zeta_2) + h_1 \frac{\partial u_1}{\partial x} = 0 \qquad \rho_1 \frac{\partial u_1}{\partial t} = -g\rho_1 \frac{\partial \zeta_1}{\partial x} + \frac{1}{h_1}(\tau_{surf} - \tau_{int}) \tag{1.5}$$

$$\frac{\partial \zeta_2}{\partial t} + h_2 \frac{\partial u_2}{\partial x} = 0 \qquad \rho_2 \frac{\partial u_2}{\partial t} = -g\rho_1 \frac{\partial \zeta_1}{\partial x} - g\triangle\rho \frac{\partial \zeta_2}{\partial x} + \frac{1}{h_2}(\tau_{int} - \tau_{bed}) \ , \tag{1.6}$$

where u_1, u_2 are depth-averaged layer velocities. The boundary conditions for this system are $u(0) = u(L) = 0$, $\partial\zeta/\partial x\,(0) = \partial\zeta/\partial x\,(L) = 0$. Using the fact that $\zeta_1 \ll \zeta_2$, ζ_1 can be neglected in the upper layer continuity relation; adding the two continuity equations and integrating in x then gives $h_1 u_1 + h_2 u_2 = 0$.

The above set of equations can be solved for each of ζ_1, u_1, and u_2 to give

$$\Box^2 \zeta_2 = \frac{1}{g\triangle\rho} \frac{\partial T}{\partial x} \ , \qquad \Box^2 u_1 = -\frac{1}{g\triangle\rho h_1} \frac{\partial T}{\partial t} \ , \qquad \Box^2 u_2 = \frac{1}{g\triangle\rho h_2} \frac{\partial T}{\partial t} \ ,$$

where we have defined

$$\Box^2 \equiv \frac{\partial^2}{\partial x^2} - \frac{1}{c^2} \frac{\partial^2}{\partial t^2} \ , \qquad c^2 \equiv \frac{g\triangle\rho h_1 h_2}{\rho_1 h_2 + \rho_2 h_1} \ , \qquad T \equiv \frac{\tau_{surf}}{h_1} - \left(\frac{1}{h_1} + \frac{1}{h_2}\right) \tau_{int} + \frac{\tau_{bed}}{h_2} \ .$$

The stress term T is comprised of both forcing (τ_{surf}) and damping (τ_{int}, τ_{bed}); in general we

expect $\tau_{int} \ll \tau_{bed}$. A reasonable parametrization for the interfacial shear is

$$\tau_{int} = C_{int}\left(u_1 - u_2\right) = C_{int}\frac{H}{h_2}u_1 = -C_{int}\frac{H}{h_1}u_2 \ ,$$

with C_{int} a friction coefficient. The bed stress can be describe in numerous ways, but perhaps the most convenient analytically is a linear relationship between τ and u,

$$\tau_{bed} = C_{bed}u_2 = -C_{bed}\frac{h_1}{h_2}u_1 \ .$$

Finally, for the forced system the velocities and ζ_2 can be taken as a sum over horizontal modes, for example

$$u_2\left(x,t\right) = \sum_{n_h=1}^{\infty} \widehat{u}_{2n_h}\left(t\right)\sin kx$$

for the velocity in layer 2. This system is therefore equivalent to a sum of forced, damped harmonic oscillators, with, for example, the u_2 governing equation reducing to

$$\left[\frac{d^2}{dt^2} + 2\alpha\frac{d}{dt} + \omega_{0n_h}^2\right]\widehat{u}_{2n_h}\left(t\right) = -\frac{1}{\rho_1 h_2 + \rho_2 h_1}\frac{2}{L}\frac{\partial}{\partial t}\int_0^L \tau_{surf}\sin kx dx \ ,$$

with inviscid (undamped) frequency $\omega_{0n_h} = ck$ and decay coefficient

$$2\alpha = \frac{h_1 h_2}{\rho_1 h_2 + \rho_2 h_1}\left(\frac{C_{int}}{\overline{H}^2} + \frac{C_{bed}}{h_2^2}\right) \ , \qquad \overline{H} = \frac{h_1 h_2}{h_2 + h_1} \ ,$$

which is apparently independent of mode number. The two-layer rectangular basin model thus provides a reasonable (and familiar) qualitative description of the principal characteristics of seiches. Heaps and Ramsbottom (1966) used a form of this method to compute the response of seiches to wind forcing, both with and without friction.

Progressive internal waves: characteristic curves

In an open system, if the stratification does not change over time and space (even, perhaps, as a local approximation), progressive internal waves can be described using the same two-

dimensional stream function equation which applies for seiches (see (B.21) in Appendix B.4):

$$\frac{1}{\overline{\rho}(z)}\frac{\partial}{\partial z}\left(\overline{\rho}(z)\frac{\partial \psi}{\partial z}\right)-\left(\frac{N^2(z)}{\omega^2}-1\right)\frac{\partial^2 \psi}{\partial x^2}=0\,, \tag{1.7}$$

with x the direction of horizontal propagation. Within the water column, free internal waves are confined vertically to the region in which $N^2(z)>\omega$. In this region of space (1.7) is hyperbolic (analogous to the classical wave equation, which is usually expressed in (x,t)), and as such the wave motion can be described along characteristic curves $\xi_{\pm}=z\pm\omega/\sqrt{N^2(z)-\omega^2}x$. In stratified natural water bodies there are typically two depths in the water column at which $N^2(z)=\omega$, i.e. the top and bottom of the pycnocline. Therefore, in an open sytem such as the ocean, the pycnocline acts as a waveguide for internal wave energy. In lakes, even though the waveguide model does not apply for standing waves, many of the associated concepts are extremely useful for describing internal seiches, in particular the interaction of the waves with the boundary.

Consider first the case of uniform stratification, $N^2=$ constant, and constant (or infinite) depth. Recall from section 1.2.1 that (1.7) is separable, and the dispersion relation is

$$\frac{\omega}{N}\approx\frac{k}{|\boldsymbol{\kappa}|}\equiv\cos\theta\,. \tag{1.8}$$

Here θ defines the angle of the wavenumber vector $\boldsymbol{\kappa}=(k,m)$ away from the horizontal (see, eg., Turner, 1973, §2.2.2). The implications of (1.8) become apparent whenever a progressive wave encounters a solid boundary. Since θ is determined solely by the properties of the waves and the fluid, this angle must be maintained upon reflection instead of the angle of the ray with respect to the surface. Internal wave ray reflection therefore differs substantially from optical reflection.

Obviously, the above progressive wave results can be immediately applied to the constant N, rectangular basin model, since the spatial domain of this system is simple (for example, $\psi\sim\sin kx\sin mz\sim\cos m\xi_{+}-\cos m\xi_{-}$, with $\xi_{\pm}\approx z\pm\omega/Nx$; see Section 1.2.1). In addition, Maas and Lam (1995) used the wave ray perspective to study seiches in lakes with constant N, but with non-uniform depth. Their technique is described briefly in Section 1.2.2. Except for a few limited cases, it is not possible to further generalize this method to obtain quantitative

solutions for systems with non-uniform stratification. However, the wave ray picture does at least provide useful qualitative information; in particular, since the slopes of the characteristic curves are $dz/dx \sim \pm\omega/N(z) \sim \pm\mu$ (i.e., the inverse of the wave ray slope $\sim m/k \approx N/\omega$), we can predict that for most (possibly all) lakes there are locations on the lake bed where the local slope ($dh/dx \sim \pm\mu$) matches the incident ray angle. The importance of these points with respect to wave ray focusing is discussed in Chapter 2.

1.2.2 Summary of seiche models

Not surprisingly, since seiches are standing waves, whose features are determined by bathymetry (the shape of the spatial domain) and stratification (coefficients in the governing equation), analytical and numerical models of linear, inviscid seiches invariably have the form of a Sturm-Liouville or eigenvalue problem. We now briefly summarize some of the most important models developed over the past century.

Displacement field eigenvalue method

Wedderburn (1912) developed the first model for internal seiches by generalizing a surface seiche method formulated by Chrystal (1905). Using a two-layer model (depths h_i and densities ρ_i, for $i = 1, 2$), the seiche motion is described as the propagation of coupled dynamic transverse (ζ_i) and longitudinal (ξ_i) displacements. This method is similar to the depth-averaged model in described Section 1.2.1, the main difference being the introduction of width variation. It is also the prototype for other methods, particularly the Defant technique, which is discussed below. We therefore provide a slightly more extensive description of the Wedderburn method.

Consider a vertical slice (with area $A_1(x)$) through and across the lake at horizontal position x, running from the surface (ζ_1 at $z = 0$) to the interface (ζ_2 at $z = h_1$). The volume of water in a small horizontal region dx around x is $V_1 = A_1(x)dx$. If this volume is displaced horizontally a small distance ξ_1, accompanied by a change in the height of both ζ_1 and ζ_2, the volume of water in its new position $(x + \xi_1)$ is

$$\begin{aligned} V_1' &= A_1(x+\xi_1)\,d(x+\xi_1) + B(x)\,(\zeta_1(x) - \zeta_2(x))\,d(x+\xi_1) \\ &= (A_1(x+\xi_1) + B(x)\,(\zeta_1 - \zeta_2))\,dx\left(1 + \frac{d\xi_1}{dx}\right) , \end{aligned}$$

where $B(x)$ is a representative width of the lake at x, measured, for example, at the interface depth. Mass conservation requires that $V_1 = V_1'$; equating the two and rearranging gives

$$B(x)(\zeta_1(x) - \zeta_2(x)) = \frac{A_1(x)}{1 + \frac{d\xi_1}{dx}} - A_1(x + \xi_1) \quad .$$

Finally, using the expansions $(1 + d\xi_1/dx)^{-1} \approx 1 - d\xi_1/dx$ and $A_1(x + \xi_1) \approx A_1 - \xi_1 dA_1/dx$ we find

$$\zeta_1 - \zeta_2 = -\frac{1}{B}\frac{\partial}{\partial x}(\xi_1 A_1) \tag{1.9}$$

after cancellations. This is equivalent to a depth-averaged continuity equation (see (1.5)) expressed in terms of displacement fields instead of velocities, and with the width of the lake taken into account.

A momentum conservation equation can be derived from the simple force balance

$$\rho_1 dV_1 a_1 = dP_1 A_1(x) \quad ,$$

in which $dP_1 = dP/dx \cdot dx$ is the pressure difference over dx in Layer 1, and a_1 is the fluid acceleration. Expanding each term in this expression,

$$\rho_1 \left[dx \left(1 + \frac{\partial \xi_1}{\partial x} \right) A_1 \right] \frac{\partial^2 \xi_1}{\partial t^2} = \left(-g\rho_1 \frac{\partial \zeta_1}{\partial x} dx \right) A_1 \quad ,$$

which simply reduces to

$$\frac{\partial^2 \xi_1}{\partial t^2} \approx -g\frac{\partial \zeta_1}{\partial x} \tag{1.10}$$

to leading order. Once again this is a depth-averaged, linearized equation, identical to the momentum equation in (1.5).

The analysis in the lower layer is the same as the upper, and yields

$$\zeta_2 = -\frac{1}{B}\frac{\partial}{\partial x}(\xi_2 A_2) \quad , \qquad \frac{\partial^2 \xi_2}{\partial t^2} = -g\frac{\rho_1}{\rho_2}\frac{\partial \zeta_1}{\partial x} - g\frac{\triangle \rho}{\rho_2}\frac{\partial \zeta_2}{\partial x} \quad . \tag{1.11}$$

The boundary conditions for both layers are $\xi(0) = \xi(L) = 0$, $\partial\zeta/\partial x(0) = \partial\zeta/\partial x(L) = 0$. The system (1.9), (1.10), and (1.11) is equivalent to the two-layer system (1.5)/(1.6); the derivation of governing equations for the ξ and ζ therefore proceeds as in Section 1.2.1. Making the rigid lid approximation $\zeta_2 \gg \zeta_1$, we first obtain the volume (~flux) conservation relation $Q_1 + Q_2 = 0$, where $Q_i = \xi_i A_i$, with $i = 1,2$. Then, assuming sinusoidal time variation $\partial/\partial t \rightarrow i\omega$, the governing equations for the transverse and longitudinal displacements are

$$\frac{1}{B\Lambda}\frac{\partial}{\partial x}\left(\Lambda\frac{\partial\zeta_2}{\partial x}\right) + K^2\zeta_2 = 0 \ , \qquad \frac{\partial}{\partial x}\left(\frac{1}{B}\frac{\partial Q_i}{\partial x}\right) + K^2 Q_i = 0 \ ,$$

in which $\Lambda(x) = A_1 A_2/(\rho_2 A_1 + \rho_1 A_2)$ and $K(x) = \omega/\sqrt{g\triangle\rho\Lambda(x)}$. The cross-sectional areas are generally taken as $A_i(x) = B(x)h_i(x)$, with layer depths h_i.

Two-layer Defant Procedure (TDP)

Defant (1918, 1960) developed a technique for evaluating surface seiches using a formulation similar to the equations of Chrystal (1905). The system is solved numerically by partitioning the lake volume with a series of cross-sections, and then varying the seiche frequency until the volume fluxes across the sections balance. Mortimer (1979) adapted the method to internal seiches using a two-layer formulation, based on the lower layer equations

$$\frac{\partial}{\partial x}\left(\xi_2(x)\, S_2(x)\right) = -B_i(x)\,\zeta_i(x) \ , \qquad \frac{\partial^2\xi_2}{\partial t^2} = -g\frac{\rho_2 - \rho_1}{\rho_2}\frac{S_1}{S_1 + S_2}\frac{\partial\zeta_i}{\partial x} \ ,$$

with B_i and ζ_i the width and vertical displacement of the interface, respectively (compare to equations (1.9), (1.10), and (1.11) above, from Wedderburn (1912)). The numerical procedure is described in more detail by Lemmin and Mortimer (1986), who studied eight lakes in Switzerland. Roget *et al.* (1997) have since developed a three-layer Defant procedure, in order to study the second vertical mode in Lake Banyoles, Spain.

Separable eigenvalue methods (and wind forcing)

For simple domains such as rectangular or cylindrical basins, the seiche governing equations are spatially separable, and the problem reduces to a set of one-dimensional spatial eigenvalue problems (see (1.1) for the rectangular basin, for example). In general the basin shape is chosen

such that the horizontal solutions are simple analytic functions (eg., $\sin kx$ or Bessel functions); the only portion of the problem which poses any analytical difficulty is the vertical function, due to the stratification (see, eg., (1.1)). Although the method is somewhat simplistic, it is useful for studying the response of seiches to wind forcing, because the overall lake response can be decomposed analytically into a sum of orthogonal modes (see, eg., Csanady 1968, 1972, Birchfield 1969, Monismith 1987). We discuss this approach in more detail in Section 1.3.

Two-layer Equivalent Depth (TED) and Variable Depth (TVD) Models

This method, developed by Schwab (1977) (following the work of Charney (1955)), is based on depth-averaged equations in two horizontal dimensions in which the bathymetry is approximated by a constant, effective epth $h_e = h_1 h_2 / (h_1 + h_2)$. Momentum (including Coriolis) and continuity in the lower layer are thus given by

$$\frac{\partial M}{\partial t} - fN = -g\varepsilon h_e \frac{\partial \zeta}{\partial x} \ , \qquad \frac{\partial N}{\partial t} + fM = -g\varepsilon h_e \frac{\partial \zeta}{\partial y} \ , \qquad \frac{\partial \zeta}{\partial t} + \frac{\partial M}{\partial x} + \frac{\partial N}{\partial y} = 0 \ .$$

Here ζ is the interface displacement, M and N are the depth-integrated horizontal flows in the lower layer, and $\varepsilon = \Delta\rho/\rho_0$. This system was solved numerically by Schwab (1977) for an irregular horizontal domain to evaluate internal Kelvin and Poincaré waves in Lake Ontario. Bäuerle (1985) performed the same analysis in Lake Geneva. Horn *et al.* (1986) subsequently generalized the method to include variable depth, to study the seiches in Lake Zürich.

Matrix multilayer

As described in Section 1.2.1, the two-layer depth-averaged (rectangular basin) model is convenient for describing the response of lakes to wind forcing. Csanady (1982) generalized the method to a multilayer formulation to describe coastal upwelling. Monismith (1985) and Münnich *et al.* (1992) later applied the technique to lakes. For a multilayer system, the momentum and continuity relations within each layer can be summarized as

$$\frac{\partial U_i}{\partial t} = -A_{ij} \frac{\partial \zeta_j}{\partial x} + T_i \ , \qquad \frac{\partial \zeta_i}{\partial t} = -B_{ij} \frac{dU_j}{dx} \ , \tag{1.12}$$

where U_i and ζ_i are the layer velocities and interface displacements, respectively, T_i are the surface, interfacial, and bed stresses, and

$$A_{ij} = \begin{cases} g & j = 1 \\ g\dfrac{\rho_j - \rho_{j-1}}{\rho_0} & i \geq j,\ j \neq 1 \\ 0 & i < j \end{cases} , \qquad B_{ij} = \begin{cases} h_j & j = 1 \\ -h_j & j = i+1 \\ 0 & j < i \text{ or } j > i+1 \end{cases} .$$

Solutions for the eigenvalues β ($= c = \omega/k$, the modal phase speed) for this system are found from the determinantal equation

$$\left| A_{ij} - \beta B_{ij}^{-1} \right| = 0 \ .$$

There is no particular advantage to this technique for computing seiche frequencies, since ω can be determined much more precisely using a continuous, one-dimensional vertical eigenvalue method. However, to describe the response of seiches to forcing, (1.12) can be summarized succinctly as (using the notation in Monismith (1985))

$$\frac{\partial}{\partial \xi_{m+}} (Q_m + \beta_m \pi_m) = F_m \ , \qquad \frac{\partial}{\partial \xi_{m-}} (Q_m - \beta_m \pi_m) = F_m \ ,$$

where we have defined the characteristics $\xi_{m\pm} = x \pm \beta_m t$, and

$$Q_m = a_{mi} U_i \ , \qquad \pi_m = a_{mi} \zeta_i \ , \qquad F_m = a_{mi} T_i$$

are the modal velocities, displacements, and forcings, respectively. The mode vector $\mathbf{a}_m$ is determined from the condition

$$a_{mi} \left(A_{ij} - \beta B_{ij}^{-1} \right) = 0 \ .$$

Monismith (1985) used this formulation to simulate the initiation of seiching (i.e., the unsteady problem) in Wellington Reservoir, Western Australia.

Two-layer matrix eigenvalue formulation

From the seiche stream function formulation (1.7), which is valid for continuous, non-constant stratification, we see that within a homogenous layer the equation reduces to Laplace's equation

$$\frac{\partial^2 \psi}{\partial z^2} + \frac{\partial^2 \psi}{\partial x^2} = 0 \ .$$

Yang and Yih (1976) used this simplification to evaluate solutions for a two-layer fluid in non-uniform basins. With $\psi = \psi_1$ and ψ_2 in the upper layer and lower layers, respectively, the formulation is completed by adding boundary conditions at the interface

$$\omega^2 \frac{\partial}{\partial z} \left(\rho_2 \psi_2 - \rho_1 \psi_1 \right) - g \left(\rho_2 - \rho_1 \right) \frac{\partial^2 \psi_1}{\partial z^2} = 0 \ , \qquad \psi_1 = \psi_2 \ ,$$

as well as the dynamic free surface

$$\omega^2 \frac{\partial \psi_1}{\partial z} - g \frac{\partial^2 \psi_1}{\partial z^2} = 0$$

and solid boundary conditions,

$$\psi_i = 0 \ .$$

Yang and Yih (1976) solved this system numerically as a matrix eigenvalue problem. The same technique can also be used to solve the continuous problem (i.e., equation (1.7); Münnich (1996)); this method is described in greater detail in Chapter 2 and Appendix C, and is used throughout the thesis to compute seiche solutions in systems with non-uniform stratification and bathymetry.

Wave ray tracing

Recall from Section 1.2.1 that internal wave motion can be described using characteristic curves. Maas and Lam (1995) used a wave ray tracing technique based on the characteristics $\xi_\pm = z \pm N/\omega x$ to compute seiches in basins with uniform stratification (constant N, and using both the hydrostatic $\left(N^2/\omega^2 - 1 \right) \rightarrow N^2/\omega^2$ and Boussinesq $\overline{\rho}^{-1} \partial/\partial z \left(\overline{\rho} \partial \psi / \partial z \right) \approx \partial^2 \psi / \partial z^2$

approximations; see (1.7)). They showed first that, as a condition for the existence of coherent seiches, all wave ray paths in the system must be closed over a finite number of reflections. When this condition is satisfied internal seiches can be evaluated as the sum of all possible paths throughout the basin. However, for most bathymetries Maas and Lam found that the ray paths do not form closed loops, but instead become progressively focused along specific limiting lines. In Chapter 2, even though we use non-uniform density profiles, the Maas and Lam (1995) results help explain the focusing behavior observed in certain limiting cases. Stated another way, our results demonstrate the role of stratification (and not just bathymetry) in determining whether or not wave ray focusing occurs, i.e., whether coherent seiches exist.

1.3 Excitation of seiches: continuous stratification

In Sections 1.2.1 and 1.2.2 we briefly outlined some of the homogeneous-layer or depth-averaged methods which can be used to describe the response of seiches to wind stress. We now discuss the excitation of seiches in systems with continuous stratification. In principal, since the (linear) internal seiches in lakes correspond to orthogonal eigenmodes of a boundary value problem (see Appendices B.3.1 and B.4.1), the seiche solutions can be used to describe the baroclinic response to wind forcing as a Fourier sum, provided we have a description of the displacement field or a realistic force balance equation. As described in Section 1.2.2, this technique has been used in analytical studies by Csanady (1968, 1972) and Birchfield (1969), and in the experimental work of Monismith (1983, 1987). We shall also review a number of problems associated with the technique.

1.3.1 Amplitude evolution

To explore the response of seiches to wind forcing we use a generalization of the method described by Monismith (1982, 1987). (Csanady (1968, 1972) and Birchfield (1969) also used this technique, but for rotational waves instead of longitudinal seiches.) An equation describing the evolution of internal seiche modal amplitudes can be derived from continuity relations

$$\frac{\partial u}{\partial x} + \frac{\partial^2 \zeta}{\partial z \partial t} = 0 \qquad \rho = -\frac{\partial \overline{\rho}}{\partial z}\zeta \ , \tag{1.13}$$

and the linear, hydrostatic ($\partial w/\partial t \approx 0$) two-dimensional momentum equations

$$\overline{\rho}\frac{\partial u}{\partial t} = -\frac{\partial P}{\partial x} + \frac{\partial \tau}{\partial z} \qquad\qquad 0 = -\frac{\partial P}{\partial z} + g\frac{\partial \overline{\rho}}{\partial z}\zeta \ . \tag{1.14}$$

Following Monismith (1987) we use the vertical displacement field ζ instead of the velocity w to simplify the density-continuity relation, so that ρ can be easily eliminated from the z-momentum equation. To expand the fields ζ, u, and τ in a Fourier sum

$$\zeta = -\sum_n A_n(t)\frac{\partial \psi_n}{\partial x}(x,z) \qquad u = \sum_n A_n'(t)\frac{\partial \psi_n}{\partial z}(x,z) \qquad \frac{\partial \tau}{\partial z} = \sum_n F_n(t)\overline{\rho}\frac{\partial \psi_n}{\partial z}(x,z) \tag{1.15}$$

we use the stream function eigensolutions $\psi_n(x,z)$ to the hydrostatic form of equation (1.7) (i.e., with $N^2 \gg \omega^2$):

$$\frac{1}{\overline{\rho}}\frac{\partial}{\partial z}\left(\overline{\rho}\frac{\partial \psi_n}{\partial z}\right) - \frac{N^2}{\omega_n^2}\frac{\partial^2 \psi_n}{\partial x^2} = 0 \ . \tag{1.16}$$

With the hydrostatic approximation, the streamfunction solutions satisfy the modified orthogonality relations

$$\int_\Omega \overline{\rho}\frac{\partial \psi_a}{\partial z}\frac{\partial \psi_b}{\partial z}dxdz = 2E_a\delta_{ab} \qquad \frac{1}{\omega_{ab}^2}\int_\Omega \overline{\rho}N^2\frac{\partial \psi_a}{\partial x}\frac{\partial \psi_b}{\partial x}dxdz = 2E_a\delta_{ab} \ ,$$

where E_a is the total energy of the linear inviscid seiche (see Appendix B.4.1). Since the forcing $\partial\tau/\partial z$ is known, we immediately compute the coefficients F_n as

$$F_n(t) = \frac{1}{2E_n}\int_\Omega \frac{\partial \tau}{\partial z}(x,z,t)\frac{\partial \psi_n}{\partial z}(x,z)\,dxdz \ . \tag{1.17}$$

Eliminating the pressure from (1.14) and rearranging yields

$$\frac{A_n''(t)}{A_n(t)} - \frac{F_n(t)}{A_n(t)} = \left[\frac{\partial}{\partial z}\left(\overline{\rho}\frac{\partial \psi_n}{\partial z}\right)\right]^{-1} g\frac{\partial \overline{\rho}}{\partial z}\frac{\partial^2 \psi_n}{\partial x^2} \ ,$$

confirming that the time and space portions are separable as the expansions 1.15 require. Substituting (1.16) into this equation then yields

$$A_n''(t) + \omega_n^2 A_n(t) = F_n(t) \quad . \tag{1.18}$$

This result is appealing because it introduces the forcing through a linear amplitude evolution equation. According to (1.18) seiches can be described as forced harmonic oscillators, analogous to the two-layer results (without damping) in Section 1.2.1. Viscous damping is somewhat difficult to incorporate into this formulation, however, because the constitutive equations (1.15)/(1.16) are continuous (as opposed to depth-averaged, say). Specifically, at leading order, viscous effects are localized in small regions near the boundaries, as opposed to being distributed throughout the water column, and the impact of these boundary layers must be incorporated through some form of asymptotic expansion. This is discussed in much more detail in Chapters 3 and 4. For the moment, we anticipate the results in Chapter 3 and claim that the addition of a viscous benthic boundary layer leads to a modification of the seiche frequency $\Omega_n = \omega_{n0} + \varepsilon\omega_{n1} + ...$, where ω_{n0} is the original inviscid frequency in (1.18), $\varepsilon = \delta/H$ is the boundary-layer thickness normalized by the lake depth, $\varepsilon\omega_{n1} = (1+i)\,\alpha_n$ is the first-order frequency shift due to viscosity, and the decay rate for each seiche mode is $\alpha_n = \mathrm{Im}(\varepsilon\omega_{n1})$. A modified amplitude evolution equation is thus obtained simply by replacing $\omega_n \rightarrow \Omega_n$ in (1.18). The resulting equation

$$A_n'' + 2i\alpha_n\omega_{n0}A_n + \left(\omega_{n0}^2 + 2\alpha_n\omega_{n0}\right)A_n = F_n$$

matches the exact damped harmonic oscillator equation

$$A_n'' + 2\alpha_n A_n' + \omega_{n0}^2 A_n = F_n$$

to first order in α.

Application to a rectangular basin

Following Monismith (1987), we apply the above analysis to a rectangular basin. The model stratification we consider is arbitrary (and unspecified), except for an epilimnion of constant density and thickness h_1. Using the scalings

$$x \sim L \ , \qquad z \sim H \ , \qquad \overline{\rho} \sim \rho_0 \ , \qquad \frac{\omega_{nm}}{N} \sim \mu \ ,$$

the rectangular basin solution reduces to

$$\psi_{mn}(x,z) = \phi_n(z) \sin k_m x \qquad k_m = m\pi \qquad m = 1, 2, \ldots \ ,$$

where the $\phi_n(z)$ satisfy the Sturm-Liouville problem (see (1.7) or (1.16))

$$\frac{d}{dz}\left(\overline{\rho}\frac{d\phi_n}{dz}\right) + \frac{1}{c_n^2}\overline{\rho}N^2\phi_n = 0 \ , \qquad \phi_n(0) = \phi_n(1) = 0 \ , \tag{1.19}$$

with $c_n = \omega_{mn}k_m^{-1}$. The ϕ_n can be normalized by the factor $\sqrt{4H/(L\rho_0)E_n}$ so as to satisfy the conditions

$$\int_0^1 \overline{\rho}\left(\frac{\partial\phi_n}{\partial z}\right)^2 dz = 1 \qquad \frac{1}{c_n^2}\int_0^1 \overline{\rho}N^2\phi_n^2 dz = 1$$

(see Appendix B.4.1). (Note that the total seiche energy $E_{nm} \Rightarrow E_n$ is independent of horizontal mode number for the rectangular basin.) With these definitions, the force coefficients in (1.17) become

$$F_{mn}(t) = \int_\Omega \frac{\partial\tau}{\partial z}(x,z,t)\frac{\partial\phi_n}{\partial z}(z)\sin k_m x dx dz \ .$$

Monismith (1987) and Csanady (1968) considered the specific case of constant, horizontally-uniform wind forcing, with $\partial\tau/\partial z = \tau_s/h_1$ over $0 < z < h_1/H$, which can be written as $\partial\tau/\partial z = \tau_s/h_1\left[\mathcal{H}(z) - \mathcal{H}(z-h_1)\right]$, with $\mathcal{H}(z)$ the Heaviside function. This choice for $\partial\tau/\partial z$ is discussed in Section 1.3.1. For this stress distribution the F_{mn} are simply

$$F_{mn} = \frac{1}{k_m}\frac{\tau_s}{h_1}\phi_n(h_1) \ , \qquad m \text{ odd} \ .$$

According to Monismith (1987), the solutions to (1.18) which satisfiy the inital value problem $A'_{mn}(0) = A_{mn}(0) = 0$ are

$$A_{mn}(t) = \frac{1}{\omega_{mn}^2 k_m} \frac{\tau_s}{h_1} \phi_n(h_1) (\cos \omega_{mn} t - 1) \quad ,$$

and the displacement and shear stress fields are

$$\zeta(x,z,t) = \frac{\tau_s}{\rho_0} \sum_n \frac{1}{c_n^2} \phi_n(h_1) \phi_n(z) \sum_{m \ odd} \frac{1}{k_m^2} \cos k_m x [\cos \omega_{mn} t - 1] \tag{1.20}$$

$$\frac{\partial \tau}{\partial z}(z) = \frac{\tau_s}{h_1} \sum_n \overline{\rho}(z) \phi_n(h_1) \frac{\partial \phi_n}{\partial z}(z) \quad . \tag{1.21}$$

These expressions have been simplified using the sum

$$\sum_{m \ odd} \frac{4}{k_m} \sin k_m x = 1 \quad .$$

Csanady's (1968) results are analogous to (1.20) and (1.21), but for a circular basin.

The 'steady' displacement

Even though we have readily obtained solutions for this system, the results are unsatisfying for several reasons. The limitations of this approach are most easily outlined by considering the time-invariant or 'steady' portions of ζ, u, and τ. Eliminating the dynamic pressure from the steady momentum equations (1.14), Monismith (1987) derived the steady force balance

$$g \frac{\partial \overline{\rho}}{\partial z} \frac{\partial \overline{\zeta}}{\partial x} = -\frac{\partial^2 \tau}{\partial z^2} \quad . \tag{1.22}$$

Since $\partial \overline{\rho} / \partial z = 0$ in the epilimnion, we know that $\partial^2 \tau / \partial z^2$ must also vanish over $0 < z < h_1$. Very little is known about current-induced shear stresses at the base of the epilimnion in real lakes, but it seems likely that the shear diminishes rapidly below $z = h_1$, since the stratification is extremely strong there. Therefore, the choice $\partial \tau / \partial z = \tau_s / h_1 [\mathcal{H}(z) - \mathcal{H}(z - h_1)]$ for the stress gradient seems a reasonable approximation to the real physical system.

Monismith defines the time-invariant portion of ζ in (1.20), i.e.,

$$\overline{\zeta}(x,z) = -\frac{\tau_s}{\rho_0 h_1}\left(x-\frac{1}{2}\right)\sum_n \frac{1}{c_n^2}\phi_n(h_1)\,\phi(z) \quad , \tag{1.23}$$

as the steady solution to the governing equations (1.13) and (1.14). This expression follows from (1.20) using

$$\sum_{m\ odd}\frac{4}{k_m^2}\cos k_m x = -\left(x-\frac{1}{2}\right) \quad .$$

(Formally, steady state can be defined either as the solution to the 'steady' form of the governing equations, i.e., setting $\partial/\partial t = 0$, or as the solution to the full equations as $t \to \infty$. The former definition is somewhat weaker because it does not require that the governing equations include any physical mechanism, such as viscous dissipation, which moves the system toward a steady state. The steady solution in (1.23) conforms to the weaker definition.) Monismith also argues that since $\partial^2\tau/\partial z^2 = -\tau_s/h_1\delta(z-h_1)$, equation (1.22) implies that $\overline{\zeta}$ must also be a representation of the delta function, i.e., the displacement field diverges at the base of the epilimnion. In fact, this is not quite correct; there are two representations of the delta function associated with equation (1.19):

$$\delta(z-a) = \overline{\rho}N^2\sum_n c_n^2\phi_n(a)\,\phi_n(z) \quad , \qquad \delta(z-a) = \overline{\rho}\sum_n \frac{\partial\phi_n}{\partial z}(a)\,\frac{\partial\phi_n}{\partial z}(z) \quad .$$

This clearly shows that $\overline{\zeta}$ itself is not divergent, but instead, from the z-momentum equation and 1.23,

$$\frac{\partial P}{\partial z} = g\frac{\partial\overline{\rho}}{\partial z}\overline{\zeta} = -\frac{\tau_s}{h_1}\left(x-\frac{1}{2}\right)\delta(z-h_1) \quad .$$

Integrating this equation simply gives

$$P(x,z) = \frac{\tau_s}{h_1}\left(x-\frac{1}{2}\right)\left[\mathcal{H}(z)-\mathcal{H}(z-h_1)\right] \quad , \tag{1.24}$$

which is consistent with the steady x-momentum equation (1.14) and the modal expansion solutions (1.20) and (1.21).

The problems with this method are clearly illustrated by (1.24). This relation implies that the baroclinic pressure field is extinguished at $z = h_1$. This is explicitly incorrect: apart from violating continuity, the baroclinic response which compensates the barotropic displacement must necessarily involve fluid below $z = h_1$, since this is the region of the water column which is stratified (i.e. fluid displacements generate buoyancy forces). At first glance it might seem that this erroneous result is a consequence of the assumed form for $\partial\tau/\partial z$, which also vanishes at $z = h_1$. However, the problem is more fundamental; it is a consequence of the linearization process, and the fact that the steady state baroclinic displacement field cannot be described using dynamic fields (i.e. ζ, u, and ρ).

Summary

Recall the full density continuity relation for $\rho(x,z,t) = \overline{\rho}(z) + \rho'(x,z,t)$,

$$\frac{D\rho}{Dt} = \frac{\partial\rho}{\partial t} + \mathbf{u}\cdot\nabla\rho = 0 \ .$$

In the steady state limit $\partial/\partial t \rightarrow 0$ this becomes

$$\mathbf{u}\cdot\nabla\rho = 0 \ ,$$

since the velocity field $\mathbf{u}$ does not vanish if the wind forcing continues indefinitely. Given this relation, the linearized result for the dynamic field

$$\frac{\partial\rho'}{\partial t} = -\frac{\partial\overline{\rho}}{\partial z}w \quad \rightarrow \quad \rho' = -\frac{\partial\overline{\rho}}{\partial z}\zeta$$

is clearly not valid in the steady state limit, and the steady baroclinic response to the wind-induced surface displacement is thus not equivalent to the seiche modal response of the system as assumed by Monismith (1987). The dynamic response to wind forcing can potentially still be described in terms of seiche modes by using the amplitude evolution equation (1.18), especially if attention is restricted to short timescales, or if viscous effects are included (i.e., using $\omega_n \rightarrow \Omega_n$). Unfortunately, at early times (i.e. shortly after the onset of winds) there is likely a lag between the forcing and the baroclinic response, because of the time required to generate surface currents

and the barotropic setup.

1.3.2 Reformulation

The steady state baroclinic displacement field $\overline{\zeta}(x,z)$ can be described in terms of seiche modes if we forego the force balance method, and instead decompose $\overline{\zeta}$ itself as a Fourier sum. The drawback to this approach is that we must employ on a somewhat ad hoc description of $\overline{\zeta}$.

Surface setup and currents

We begin by exploring the relationship between the steady surface setup and currents in the epilimnion. For a homogeneous surface layer (depth h_1, with constant density ρ_s and viscosity ν), using the far-field approximation (i.e., neglecting vertical velocities) the steady surface current $u(z)$ can be found from the x-momentum equation

$$0 = -\frac{\partial P}{\partial x} + \rho_s \nu \frac{\partial^2 u}{\partial z^2} \ .$$

The solution to this equation which conserves mass and satisfies a free-slip condition at the (undisplaced) base of the mixed layer,

$$\int_0^{h_1} u dz = 0 \ , \qquad \frac{\partial u}{\partial z}(h_1) = 0 \ ,$$

is simply

$$u(z) = \frac{\tau_s h_1}{6\rho_s \nu}\left(3\frac{z^2}{h_1^2} - 6\frac{z}{h_1} + 2\right) \ .$$

Note that the free surface condition $\tau_s = \rho_s \nu \partial u/\partial z\,(0)$ leads to the requirement

$$\frac{\partial P}{\partial x} = \frac{\partial \tau}{\partial z} = \frac{\tau_s}{h_1} \ . \tag{1.25}$$

This is conventionally regarded as a depth-averaged momentum balance, but in fact we see that it also corresponds to a steady state condition. Therefore, neglecting the impact of the fluid displacement at $z = h_1$, the assumption of constant stress in the surface layer which was

used by Csanady (1968) and Monismith (1985) in fact corresponds to a fully-developed (steady state) current profile. Clearly, using $\partial\tau/\partial z = \tau_s/h_1 \left[\mathcal{H}(z) - \mathcal{H}(z-h_1)\right]$ beginning immediately at $t = 0$ neglects the time required for the epilimnetic currents to fully develop, as noted at the end of Section 1.3.1. The time scale for the baroclinic response is often taken as one-quarter wave period of the fundamental (V1H1) mode. However, as discussed in Section 1.3.1, wind-driven fluid displacements in the epilimnion are not related to the seiche response at leading order. The time scale for the development of surface currents is governed by numerous other factors, such as the strength of wind forcing and the thickness of the surface mixed layer, and is only indirectly affected by the seiche response, i.e., due to the tilting of the base of the epilimnion.

Integrating (1.25) (which corresponds to the steady x-momentum equation; see (1.14)) within the surface layer, we find

$$P = \frac{\tau_s L}{h_1}\left(\frac{x}{L} - \frac{1}{2}\right) = \rho_s g \zeta_s(x) \quad ,$$

where we have defined the surface setup

$$\zeta_s(x) = -\frac{u_*^2 L}{g h_1}\left(\frac{x}{L} - \frac{1}{2}\right) \equiv -\left|\zeta_s\right| \gamma(x) \quad , \tag{1.26}$$

with $|\zeta_s| \equiv u_*^2 L/(2gh_1)$ and $\gamma(x) \equiv 2x/L - 1$. Note that the displacement field within the surface layer is indeterminate (or may not in fact be a meaningful concept), since the vertical (dynamic) pressure gradient vanishes over $0 < z < h_1$.

Baroclinic response revisited

Below the epilimnion, integrating the z-momentum equation (see (1.14)) gives

$$P(x,z) = g\int_0^z \frac{d\overline{\rho}}{dz'}\overline{\zeta}(x,z')\,dz' + \rho_s g \zeta_s(x) \quad . \tag{1.27}$$

This solution satisfies $P(x, z < h_1) = \rho_s g \zeta_s(x) = -\left(\rho_s u_*^2 L/h_1\right)\gamma(x)$. In order for the steady baroclinic displacement field to uniformly compensate the barotropic setup throughout the

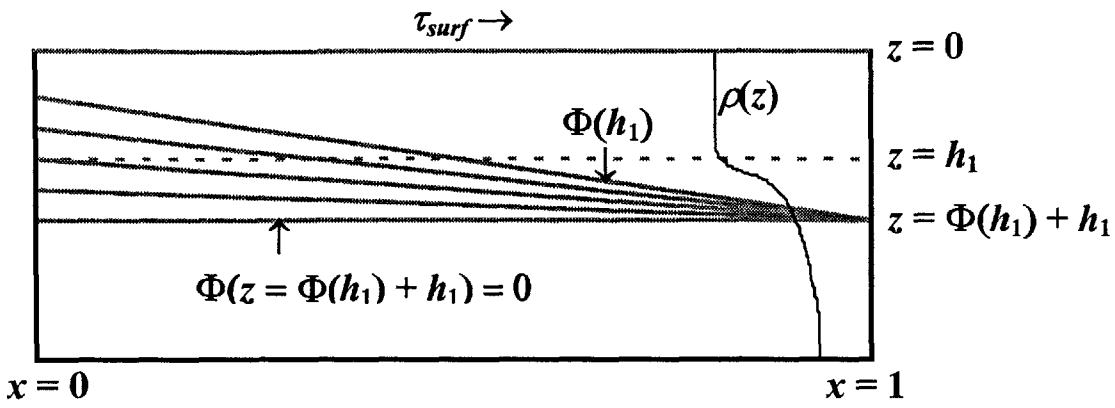

Figure 1-1: Descriptive diagram of the vertical displacements $\Phi(z) = \Phi(h_1) + h_1 - z$ associated with the steady state baroclinic displacement field $\overline{\zeta}(x, z) = \Phi(z)\gamma(x)$.

water column, $\overline{\zeta}$ must have the same horizontal structure as P, i.e.,

$$\overline{\zeta}(x, z) = \Phi(z)\gamma(x) \quad . \tag{1.28}$$

The maximum isopycnal displacement occurs at the base of the epilimnion, i.e., $\Phi(z = h_1)$. Below $z = h_1$, the isopycnal tilts become progressively smaller, until the dynamic pressure gradient vanishes at some depth in the pycnocline. Since adjacent isopycnals cannot cross one another, the displacement $\Phi(z)$ at the edge of the lake (i.e., at $x = 1$) at depth z below h_1 must be the same as the displacement $\Phi(z = h_1)$; see Figure 1-1. The equilibrium state can thus be described by $\Phi(z) + z = \Phi(h_1) + h_1$ for $\forall z \in (h_1, h_1 + \Phi(h_1))$. Rearranging this expression, the displacement field Φ is simply

$$\Phi(z) = \Phi(h_1) + h_1 - z \quad . \tag{1.29}$$

The depth at which the baroclinic response cancels the pressure gradient established by the barotropic setup is then $z = h_1 + \overline{\zeta}(0, h_1)$, i.e.

$$\frac{\partial P}{\partial x}\left(x, h_1 + \overline{\zeta}(0, h_1)\right) = 0 \qquad \forall x \quad .$$

Since P and $\overline{\zeta}$ are separable, using (1.26) and (1.27), and (1.28) this condition simply reduces to

$$\int_0^{h_1+\Phi(h_1)} \frac{d\overline{\rho}}{dz'}\Phi\left(z'\right)dz' = \rho_s\left|\zeta_s\right| \quad . \tag{1.30}$$

In other words, at steady state the baroclinic response integrated over the pycnocline compensates and cancels the wind-induced surface setup pressure gradient. Equation (1.30) can be further rearranged through partial integration to give

$$\int_0^{h_1+\Phi(h_1)} \left(\overline{\rho}-\rho_s\right)\frac{d\Phi}{dz'}dz' = -\rho_s\left|\zeta_s\right| \quad ,$$

using the fact that

$$\left[\left(\overline{\rho}-\rho_s\right)\Phi\right]_0^{h_1+\Phi(h_1)} = 0 \quad ,$$

since $\Phi\left(h_1+\Phi\left(h_1\right)\right)=0$, and $\overline{\rho}\left(0\right)=\rho_s$. With $d\Phi/dz=-1$ (see (1.29)), this further reduces to

$$\int_{h_1}^{h_1+\Phi(h_1)} \left(\overline{\rho}\left(z'\right)-\rho_s\right)dz' = \rho_s\left|\zeta_s\right| \quad . \tag{1.31}$$

As an example, consider the simple linear stratification

$$\overline{\rho} = \rho_s + \triangle\rho\frac{z-h_1}{\triangle h} \qquad h_1 < z < h_1+\triangle h \quad ,$$

where we explicitly require that the baroclinic displacement does not extend beyond the bottom of the pycnocline, i.e., $\triangle h > \Phi\left(h_1\right)$. From (1.31) we find

$$\frac{\triangle\rho}{\triangle h}\int_{h_1}^{h_1+\Phi(h_1)}\left(z'-h_1\right)dz' = \rho_s\left|\zeta_s\right| \qquad \rightarrow \qquad \left(\Phi\left(h_1\right)\right)^2 = 2\frac{\rho_s}{\triangle\rho}\left|\zeta_s\right|\triangle h \quad ,$$

which completely specifies the baroclinic response to the wind stress $\tau_s=\rho_s u_*^2$,

$$\overline{\zeta}\left(x,z\right) = \left(\sqrt{\frac{\rho_s}{\triangle\rho}\frac{u_*^2 L}{g h_1}\triangle h} + h_1 - z\right)\left(2\frac{x}{L}-1\right) \quad . \tag{1.32}$$

This displacement field can be described in terms of seiche modes using the solutions $\chi(x)$ to the seiche vertical equation (1.1), i.e.,

$$\zeta(x,z) = \sum_m \sum_n a_{nm} \overline{\rho}(z) \frac{N^2(z)}{\omega_{nm}^2} k_n^2 \chi_m(z) \cos\frac{n\pi x}{L} \ .$$

Using the fact that

$$\int_0^L \left(2\frac{x}{L} - 1\right) \cos\frac{p\pi x}{L} dx = -2L\frac{1-(-1)^p}{p^2\pi^2} \ ,$$

the coefficients a_{nm} are given by

$$a_{pq} = -\frac{1-(-1)^p}{p^2\pi^2} \frac{1}{E_{pq}L} \int \left(\sqrt{\frac{\rho_s}{\triangle\rho}\frac{u_*^2 L}{g h_1}\triangle h} + h_1 - z\right) \overline{\rho}(z) \chi_q(z) \, dz$$

(see Appendix B.4.1). This expression can be solved numerically after specifying the values of the parameters $(\rho_s, \triangle\rho, u_*^2, h_1, \triangle h, L)$, and solving the vertical structure function eigenproblem (1.1) to evaluate the $\chi_m(z)$.

1.4 Summary

In this chapter we have briefly outlined some of the fundamental concepts associated with internal seiching, as well as the analytical and numerical techniques most commonly used to evaluate seiches. Even though seiches are adequately described qualitatively as forced, damped harmonic oscillators, it is difficult to obtain realistic quantitative results because of the mathematical difficulties which arise due to the irregular bathymetry and continuous, non-uniform stratification in real lakes. The summary of models in Section 1.2.2 is designed to highlight these difficulties, and to preface the discussion of the analysis methods used in the remaining chapters.

In the remainder of this chapter we discussed the generation of internal seiches by wind forcing. In Section 1.3 we showed that, for a continuous stratification, seiche amplitude is described by a linear evolution equation (1.18), and that viscous damping is easily included through a modification of the inviscid frequency (as described in Chapter 3). However, solving the evolu-

tion equation for a rectangular basin revealed that the steady state baroclinic response cannot be easily described through a direct force balance as a sum of seiche modes. We concluded in Section 1.3.2 by presenting an alternative approach, base on an ad hoc formulation for the baroclinic displacement field generated by a steady wind-induced surface setup.

Bibliography

[1] Bäuerle, E., 1985. Internal free oscillations in the Lake of Geneva. *Ann. Geophys.* **3**: 199-206.

[2] Birchfield, G. E., 1969. Response of a Circular Model Great Lake to a Suddenly Imposed Wind Stress. *J. Geophys. Res.* **74**: 5547-5554.

[3] Charney, J. G., 1955. The generation of oceanic currents by wind. *J. Mar. Res.*, **14**: 477-498.

[4] Chrystal, G., 1905. On the Hydrodynamical Theory of Seiches. *Trans. Roy. Soc. Edin.*, vol. **XLI**, part III (no. 25): 599-649.

[5] Csanady, G. T., 1968. Motions in a Model Great Lake Due to a Suddenly Imposed Wind. *J. Geophys. Res.* **73**: 6435–6447.

[6] Csanady, G. T., 1972. Response of Large Stratified Lakes to Wind. *J. Phys. Oceanogr.* **2**: 3–13.

[7] Csanady, G. T., 1982. On the Structure of Transient Upwelling Events. *J. Phys. Oceanogr.*, **12**: 84-96.

[8] Defant, A., 1918. Neue Methode zur Ermittlung der Eigenschwingungen von abgeschlossenen Wassermassen. *Ann. Hydrogr. Berlin* **46**: 78-85.

[9] Defant, A., 1960. Physical oceanography. Pergamon, London, vol. II, 598 pp.

[10] Evans, R.D. 1994. Empirical evidence of the importance of sediment resuspension in lakes. Hydrobiologia 285, 5-12

[11] Forel, F. A., 1876. La Formule des Seiches. *Archives des Sciences Physiques et Naturelles, Genève.*

[12] Gaedke, U, M. Schimmele, 1991. Internal seiches in Lake Constance - influence on plankton abundance at a fixed sampling site. *J. Plankton Res.*, **13**(4): 743-754.

[13] Gloor, M., A. Wüest, and M. Münnich, 1994. Benthic boundary mixing and resuspension induced by internal seiches. *Hydrobiologia* **284**: 59-68.

[14] Gloor, M., A. Wüest, and D. M. Imboden, 2000. Dynamics of mixed bottom boundary layers and its implications for diapycnal transport in a stratified, natural water basin. *J. Geophys. Res.*, **105**(C4): 8629-8646.

[15] Goudsmit, G.-H., F. Peeters, M. Gloor, and A. Wüest, 1997. Boundary versus internal diapycnal mixing in stratified natural waters. *J. Geophys. Res.*, **102** C13, 27903-27914.

[16] Hagatun, K, and Eidsvik, K. J., 1986. Oscillating turbulent boundary layer with suspended sediments. *J. Geophys. Res.*, **91** C11: 13045-13055.

[17] Heaps, N. S., and A. E. Ramsbottom, 1966. Wind effects on water in a narrow two-layered lake. *Phil. Trans. Roy. Soc. Lond.* **A 259**: 391-430.

[18] Horn, W., C. H. Mortimer, and D. J. Schwab, 1986. Wind-induced internal seiches in Lake Zürich observed and modeled. *Limnol. Oceanogr.* **31**(6): 1232-1254.

[19] Ivey, G. N., and G. M. Corcos, 1982. Boundary mixing in a stratified fluid. *J. Fluid Mech.*, **121**: 1-26.

[20] LaZerte, B. D., 1980. The dominating higher order vertical modes of the internal seiche in a small lake. *Limnol. Oceanogr.* **25**(5): 846-854.

[21] Lemmin, U. and C. H. Mortimer, 1986. Tests of an extension to internal seiches of Defant's procedure for determination of surface seiche characteristics in real lakes. *Limnol. Oceanogr.*, **31**(6): 1207-1231.

[22] Lemmin, U., 1987. The structure and dynamics of internal waves in Baldeggersee. *Limnol. Oceanogr.*, **32**(1): 43-61.

[23] Levy, D. A., R. L. Johnson, J. M. Hume, 1991. Shifts in fish vertical distribution in response to an internal seiche in a stratified lake. *Limnol. Oceanogr.*, **36**(1): 187-192.

[24] Maas, L. R. M., and F.-P. A. Lam, 1995. Geometric focusing of internal waves. *J. Fluid Mech.*, **300**: 1-41.

[25] MacManus, J. nd R. W. Duck, 1988. Internal seiches and subaqueous landforms in lacustrine cohesive sediments. *Nature*, **334**: 511-513.

[26] Monismith, S. G., 1983. Dynamic response of stratified reservoirs to surface shear stress. PhD Thesis, University of California, Berkeley.

[27] Monismith, S. G., 1985. Wind-forced motions in stratified lakes and their effect on mixed-layer shear. *Limnol. Oceanogr.*, **30**(4): 771-783.

[28] Monismith, S., 1987. Modal response of reservoirs to wind stress. *J. Hydr. Eng.*, **113**(12): 1290.

[29] Mortimer, C. H., 1979. Strategies for coupling data collection and analysis with dynamic modelling of lake motions. Hydrodynamics of Lakes: Symposium Proceedings, pp. 183-222. W. H Graf and C. H. Mortimer, editors. Elsevier Scientific Publishing.

[30] Münnich, M., A. Wüest, and D. M. Imboden, 1992. Observations of the second vertical mode of the internal seiche in an alpine lake. *Limnol. Oceanogr.*, **37**(8): 1705-1719.

[31] Münnich, M., 1996. Influence of bottom topography on internal seiches in stratified media. *Dyn. Atmos. and Oceans*, **23**: 257-266.

[32] Phillips, O. M., J.-H. Shyu, H. Salmun, 1986. An experiment on boundary mixing: mean circulation and transport. *J. Fluid Mech.* **173**: 473-499.

[33] Pierson, D. C. and G. A. Weyhenmeyer, 1994. High resolution measurements of sediment resuspension above an accumulation bottom in a stratified lake. *Hydrobiologia* **284**: 43-57.

[34] Roget, E., G. Salvadé, and F. Zamboni, 1997. Internal seiche climatology in a small lake where transversal and second vertical modes are usually observed. *Limnol. Oceanogr.* **42**(4): 663-673.

[35] Saggio, A., and J. Imberger, 1998. Internal wave weather in a stratified lake. *Limnol. Oceanogr.*, **43**(8): 1780-1795.

[36] Schwab, D. J., 1977. Internal free oscillations in Lake Ontario. *Limnol. Oceanogr.* **22**: 700-708.

[37] Sheng, Y. P. and W. Lick, 1979. The transport and resuspension of sediments in a shallow lake. *Jour. Geophys. Res.* 84 C4, 1809.

[38] Shteinman, B., W. Eckert, S. Kaganowsky, and T. Zohary, 1997. Seiche-induced resuspension in Lake Kinneret: A fluorescent tracer experiment. *Water, Air, and Soil Pollution*, **99**(1-4): 123-131.

[39] Slinn, D. N. and J. J. Riley, 1996. Turbulent mixing in the oceanic boundary layer caused by internal wave reflection from sloping terrain. *Dynam. Atmos. Oceans*, **24**(1-4): 51-62.

[40] Turner, J. S., 1973. Buoyancy Effects in Fluids. Cambridge University Press.

[41] Wedderburn, E. M., and A. M. Williams, 1911. The temperature seiche, Part II, Hydrodynamical theory of temperature oscillations. *Trans. Roy. Soc. Edinburgh*, **47**: 628-634.

[42] Wedderburn, E. M., 1912. Temperature observations in Loch Earn; with a further contribution to the hydrodynamical theory of temperature oscillations. *Trans. Roy. Soc. Edinburgh*, **48**: 629-695.

[43] Wedderburn, E. M., and A. W. Young, 1915. Temperature observations in Loch Earn, Part II. *Trans. Roy. Soc. Edinburgh*, **50**: 741-767.

[44] Wiegand, R. C. and V. Chamberlain, 1987. Internal waves of the second vertical mode in a stratified lake. *Limnol. Oceanogr.*, **32**(1): 29-42.

[45] Wüest, A. and M. Gloor, 1998. Bottom boundary mixing: The role of near-sediment stratification. In: Physical Processes in Lakes and Oceans, Ed. J. Imberger. AGU

[46] Yang, W. H, and C.-S. Yih, 1976. Internal waves in a circular channel. *J. Fluid Mech.*, **74**: 183-192.

Chapter 2

Bathymetry, stratification, and internal seiche structure

Abstract[1]

Internal seiches play a significant role in a broad range of physical, chemical, and biological processes in lakes. A detailed assessment of the impact of seiching requires an understanding of seiche structure, which is determined by bathymetry and stratification. In this study, internal seiche solutions are evaluated for arbitrary bathymetry and continuous stratification using a 2D numerical model. Formulated in terms of a streamfunction, the model produces a finite set of linear internal wave eigenmodes, and allows the computation of the complete velocity field (over a grid) associated with each seiche mode. Several idealized configurations of continuous stratification and variable bathymetry are used to explore the effect of non-uniform systems on internal wave structure. In particular, we focus on bed velocity distribution and the resulting potential impact on scalar fluxes, sediment transport, and internal wave damping. Model results are also compared to thermistor chain data collected in the Upper Mystic Lake (UML, Winchester, MA). Using an idealized description of the UML bathymetry, and density profiles which emulate the seasonal variation of stratification in the lake, the evolution of bed velocities during the autumnal breakdown in stratification is assessed, providing insight into the fate of the contaminants entering the lake.

[1]This chapter has been published as:
P. D. Fricker and H. M. Nepf, 2000. Bathymetry, stratification, and internal seiche structure, *J. Geophys. Res. - Oceans* **105**(C6): 14,237-14,251.

2.1 Introduction

Internal seiches play a significant role in a broad range of physical, chemical, and biological processes in lakes. By mediating exposure to light and nutrients, the vertical excursions of fluid associated with the wave motions have been shown to affect the spatial distribution of macro- and microscopic organisms (Levy *et al.* 1991, Haury *et al.*, 1983). The sustained oscillations of water over the bed contribute to the generation of a benthic boundary layer, which enhances the dissolution, resuspension, and transport of nutrients, contaminants, and sediment (Gloor *et al.* 1994, Pierson and Weyhenmeyer, 1994), and contribute to effective vertical mixing through horizontal buoyancy-driven flows (Ivey and Corcos 1982, Heinz *et al.* 1990). For example, MacManus and Duck (1988) showed that seiche-induced resuspension was responsible for the sediment scouring patterns observed along the sides of Loch Earn. Because of the lake's relatively simple shape, they were able to model the spatial (i.e. nodal) properties of the seiches using a simple rectangular basin model. Assessing the impact of seiching in lakes with more complex bathymetry is more difficult, because the internal seiches themselves are modified by the basin. In the present study we use a numerical method to evaluate the internal seiches in lakes with non-uniform bathymetry and stratification, focusing attention specifically on the V1H1-type mode. The principal objectives of this work are to examine the effect of bathymetry and stratification on seiche structure, and ultimately to determine the potential impact of seiche motions on resuspension and dissolution of bed material.

Since the earliest studies of internal seiching, the spatial characteristics and oscillation periods of individual internal wave modes have been evaluated using simplified analytical formulations. Lakes were originally modelled as rectangular basins with a two-layer density profile (e.g. Wedderburn 1907, 1912, Heaps and Ramsbottom 1966). A principal drawback to this formulation is that it can only describe the first vertical mode (*i.e.* V1Hn, n=1,2,...). This can be a serious limitation, because higher vertical modes, particularly V2H1, are now known to be present in many systems (LaZerte 1980, Wiegand and Chamberlain 1987, Münnich *et al.* 1992).

Increased computing power has allowed the development of progressively more sophisticated models of internal seiching. The advances in modelling have generally fallen into two categories: improved descriptions of stratification, and the generalization to arbitrary bathymetry. With

regard to the former, wave modes for a continuous stratification were computed numerically by Csanady (1968a,b), Birchfield (1969), and Monismith (1987), and pseudo-analytically by Csanady (1972) as one-dimensional eigenvalue problems in an idealized rectangular or cylindrical basin. Csanady (1982) and Monismith (1985) also used a multiple-layer matrix formulation to approximate continuous density profiles. Although these models yield improved estimates of internal seiche period, they do not provide a realistic picture of spatial structure, due to the use of over-simplified bathymetries. Conversely, most models which incorporate a more accurate basin shape use an overly simplistic two-layer density profile. For example, methods such as the two-layer Defant procedure (TDP), which is an adaptation by Mortimer (1979) and Lemmin and Mortimer (1986) of a surface seiche model (Defant 1918, 1961), as well as the two-layer variable depth (TVD) model (Schwab 1977, Horn *et al.* 1986), only describe vertical internal seiche motion in the horizontal plane at the interface.

In the present study, internal seiches are evaluated for systems with both irregular bathymetry and realistic continuous stratification, using a two-dimensional numerical eigenvalue technique. The method can be considered a generalization to two dimensions of the procedure used by Csanady (1968a,b), Birchfield (1969), and Monismith (1987) described above. A similar eigenvalue method was first used by Yang and Yih (1976) to investigate waves in a basin with semicircular bathymetry. However, their analysis was performed for a two-layer fluid, and discussion was therefore restricted to horizontal modes. More recently, Münnich (1996) studied the effect of varying topography on internal seiches using a formulation similar to that presented here, but only considered uniform stratification.

As a test case, internal seiche solutions are computed for the Upper Mystic Lake (UML, Winchester, MA). Thermistor chain data has been collected in the UML for several field seasons as part of an ongoing investigation of the mobilization of contaminants in the system. These data allow direct comparison between the model results and real internal seiche behavior. The Mystic Lake bathymetry is comprised of a deep main basin and a shallow shelf which extends over one third of the lake. This feature is typical of many systems; lakes with similar bathymetries, although larger in scale, include Lakes Geneva and Zürich. Many of the results presented here are therefore directly applicable to these systems.

The model results demonstrate that large-scale bathymetric features lead to the magnifica-

tion of flow at specific locations along the bed. The resulting spatially non-uniform bed stress will give rise to enhanced localized mixing in the benthic boundary layer, which in turn can cause localized increases in nutrient and contaminant fluxes due to both resuspension and enhanced dissolution. For the UML bathymetry, the model shows that the velocities on the shelf are substantially magnified, even when the mixed layer is very shallow and the thermocline region is relatively high above the bed. Furthermore, as the position of the thermocline varies seasonally, the modification of the internal waves due to the bathymetry also changes, with the greatest magnification of flow occuring as the bottom of the surface mixed layer approaches the depth of the shelf.

2.2 Numerical Method

Internal seiche solutions are evaluated for arbitrary bathymetry and continuous stratification using a 2D numerical model. Formulated in terms of a streamfunction, the model produces a finite set of linear internal wave eigenmodes, which allows the computation of the complete displacement and velocity field (over a grid) associated with each seiche mode.

A linearized governing equation for internal waves in two dimensions can be derived from the full (2D) inviscid momentum (Euler) equations and continuity. The velocities (u, w), pressure (P), and density (ρ) are decomposed into mean and perturbation fields,

$$\begin{aligned} u(x,z,t) &\rightarrow u'(x,z,t) & P(x,z,t) &\rightarrow \overline{P}(z) + P'(x,z,t) \\ w(x,z,t) &\rightarrow w'(x,z,t) & \rho(x,z,t) &\rightarrow \overline{\rho}(z) + \rho'(x,z,t) \ , \end{aligned} \tag{2.1}$$

with the perturbation terms corresponding to the seiche motion. In the momentum equations, the mean pressure and density are found to satisfy the hydrostatic relation

$$\overline{P}_z = g\overline{\rho} \ ,$$

and therefore cancel one another. In this expression, and throughout the paper, we use the notation $f_x \equiv \frac{\partial f}{\partial x}$.

In the usual way, the velocity field may be expressed in terms of a streamfunction,

$$u = \psi_z \qquad w = -\psi_x \ , \tag{2.2}$$

which can be summarized as $\mathbf{q} = (u, w) = \nabla \times \Gamma$, with $\Gamma \equiv (0, \psi, 0)$. Since we seek wave solutions, we assume oscillatory behavior in the perturbation fields, *i.e.*

$$\phi(x, z, t) \Rightarrow \Re\left[\phi(x, z) e^{i\omega t}\right] \ ,$$

where $\phi = (\psi, \rho', P')$. Neglecting nonlinear terms, which is valid for small wave amplitudes, this formulation yields the governing equation (see e.g. Yih 1980, page 70)

$$\psi_{zz} - \frac{N^2}{g}\psi_z - \frac{N^2 - \omega^2}{\omega^2}\psi_{xx} = 0 \qquad N^2(z) = -\frac{g}{\overline{\rho}}\overline{\rho}_z \ , \tag{2.3}$$

where N^2 is the buoyancy frequency. The boundary conditions that complete this system are found from the no-flux requirement on the velocities:

$$\mathbf{n} \cdot \mathbf{q} = 0 \quad \rightarrow \quad \mathbf{n} \cdot (\nabla \times \Gamma) = \mathbf{p} \cdot \nabla\psi = 0 \ , \tag{2.4}$$

where $\mathbf{n}$ and $\mathbf{p}$ are unit vectors normal to and parallel with the boundary, respectively (i.e. $\mathbf{n} \cdot \mathbf{p} = 0$). Since $\mathbf{p} \cdot \nabla\psi = \frac{\partial\psi}{\partial s}$ is zero everywhere along the boundary, denoted by co-ordinate s, we are free to take $\psi(s) = 0$ without loss of generality. Finally, for simplicity we also make the rigid lid approximation, and set $\psi(x, 0) = 0$.

Other than linearization and the rigid lid, no additional approximations were made in this derivation. Additional simplifications are possible, however, the most common being the hydrostatic and Boussinesq approximations. For example, Thorpe (1968) presented an analysis of first-order nonlinear expansion terms for progressive internal waves, using the zeroth–order solution in a Boussinesq fluid. Münnich (1996) numerically evaluated linear eigenmodes using both approximations. The resulting governing equation,

$$\psi_{zz} - \frac{N^2}{\omega^2}\psi_{xx} = 0 \ , \tag{2.5}$$

has the advantage that the eigenvalues vary linearly with the dimensions of the system, and are, in that sense, scale-independent. The principle benefit of this is that round-off errors in the computations can be avoided, which might otherwise result from the small vertical-to-horizontal aspect ratio in the discretization of a real lake system. The possibility of round-off error does arise when working with (2.3), and may lead to a steppiness in the computed solutions. For the systems we consider, the hydrostatic and Boussinesq terms are exceptionally small, and could justifiably be neglected. However, since the inclusion or omission of these terms has no impact on the difficulty or tractability of the problem in our calculations, we have no need to exclude them. We therefore employ equation (2.3) for all the analyses.

For a non-regular basin, (2.3) is not separable, and the eigensolutions for the full 2D system must be evaluated numerically. The equation may be rewritten as

$$N^2\psi_{xx} = \omega^2\left(\psi_{zz} - \frac{N^2}{g}\psi_z + \psi_{xx}\right) \quad , \tag{2.6}$$

which, along with the boundary conditions, are discretized such that the matrix formulation of the problem has generalized eigenvalue form,

$$\mathbf{N}\Psi = \omega^2\mathbf{M}\Psi \quad .$$

$\mathbf{N}$ denotes a matrix whose elements are determined in part by the buoyancy frequency (the left-hand-side of (3.55)), while $\mathbf{M}$ corresponds to the discretization of the right-hand-side. If either of the matrices $\mathbf{M}$, $\mathbf{N}$ has an inverse, which is generally the case, then (3.55) can be put in standard eigenvalue form. In the present study, the problem is solved in standard form using a finite difference formulation.

The velocities are evaluated by taking derivatives of the numerical streamfunction solution (see equation 3.52). In general, grid points in the computational mesh do not lie on the boundary, but instead are located a fractional distance from the bed, in both the x and z directions. To improve the estimate of velocity at the bed, the numerical solution is interpolated over a finer grid, exploiting the known condition $\psi(s) = 0$, to generate data closer to the boundary (s). A slight steppiness is still observed in the final result, but this effect can be arbitrarily minimized by using an even finer grid. To compare the model results to thermistor chain observations, we

calculate the vertical fluid displacements,

$$\zeta = -\frac{1}{i\omega}\psi_x \ , \tag{2.7}$$

which only differ from the vertical velocities by the factor $(i\omega)^{-1}$. This factor will be ignored, since we are interested in the envelope of the seiche motion and not the absolute magnitude.

The eigensolutions which correspond to the fundamental modes, for example the V1H1 or V2H1 analogues, appear mid-way within the manifold of computed solutions to (3.55). In other words, their eigenvalues are neither the largest nor the smallest in the solution set. The reason for this is illustrated by the analytical solution to (2.3) for a rectangular basin and constant N^2 (e.g. Turner, 1973, page 23):

$$\psi(x,z) = \psi_0 \sin\frac{n\pi x}{L} e^{-\frac{N^2}{2g}z} \sin\frac{m\pi z}{H} \ , \tag{2.8}$$

in which the horizontal (n) and vertical (m) mode numbers are related to the frequency by

$$\frac{\omega_{nm}^2}{N^2} = \frac{n^2}{n^2 + \mu^{-2}m^2 + \frac{N^4L^2}{4\pi^2g^2}} \qquad \begin{matrix} n,m = 1,2,3,.... \\ \mu^2 = \frac{H^2}{L^2} \end{matrix} \ . \tag{2.9}$$

The maximum and minimum values of ω_{nm} correspond respectively to $n \to \infty$ and $m \to \infty$, with the other mode number bounded. The seiche modes of greatest interest, for which $n \approx m \approx 1$, do not correspond to an extremum eigenvalue. As a result, it is necessary to compute all of the eigensolutions for the discretized system, and then identify the desired oscillations from among the entire set by inspection, using their nodal properties. This makes the analysis computationally expensive, thereby limiting the possible size of the discretization. However, the structural features of the numerical seiche solutions presented in this paper were generally found to be unaffected by the size of the discretization employed. In most of the computations, the square domain overlying the basin was discretized in a 40×40 grid, resulting in 1045 wet points (and 1045×1045 matrices) for the parabolic basin and 869 wet points for the model UML basin. A 30×30 grid was used for the series which included the largest (nearly-rectangular) basin, due to the prohibitive size of the resulting matrices.

Lastly, the use of a 2D model in this study raises the issue of attempting a 3D formu-

lation. While a 3D formulation is possible (in terms of the seiche-related pressure deviation field $P'(x, y, z, t)$), it was found to be prohibitively difficult for three reasons: 1) Adding an extra dimension generates larger matrices, and hence a larger eigenvalue computation; 2) The eigenvalue problem is quadratic (and is also complex), requiring that the size of the matrix system be doubled in order to reduce it to a linear form; 3) The boundary conditions for the system are Neumann conditions, so that the resulting matrices tend to be singular. This means that the eigenvalue problem cannot be recast in standard form, and must be solved as a more expensive generalized problem. Fortunately, the 2D formulation presented here provides meaningful results for longitudinal seiches in small to mid-sized lakes, for which Coriolis effects are unimportant. The excellent agreement between model results and field observations supports this conclusion, as demonstrated in the next section.

2.3 Test case: the Upper Mystic Lake

2.3.1 Site description

The Upper Mystic Lake (UML, Figure 2-1) is located in greater metropolitan Boston, at the southern end of the Aberjona Watershed. The lake is relatively small, roughly 1000 m long and 600 m wide, with a maximum depth of 25 m. The principal axis of wind forcing is almost aligned with the major axis of the lake (also shown in Figure 2-1), with winds predominantly from the south in summer, and from the north in winter. This is due to a combination of local ambient weather conditions and the presence of low hills which flank the UML on its eastern and western sides. Stratification conditions at midsummer are consistently strong, with typical surface and bottom temperatures of 27-30°C and 5-6°C, respectively, and a surface layer depth of roughly 4 m. The bathymetric cross-section along the major axis (Figure 2-2) shows that the northern third of the lake consists of a shoal with maximum depth 9 m. The stratification profile shown at the right is derived from thermistor chain data collected in late summer. Later results will show that the location of the thermocline relative to the shelf has a major impact on the internal seiches in the lake.

The Aberjona Watershed is highly contaminated with organic and metal industrial wastes, the legacy of an industrial period which spanned approximately 150 years (Durant *et al.* 1990,

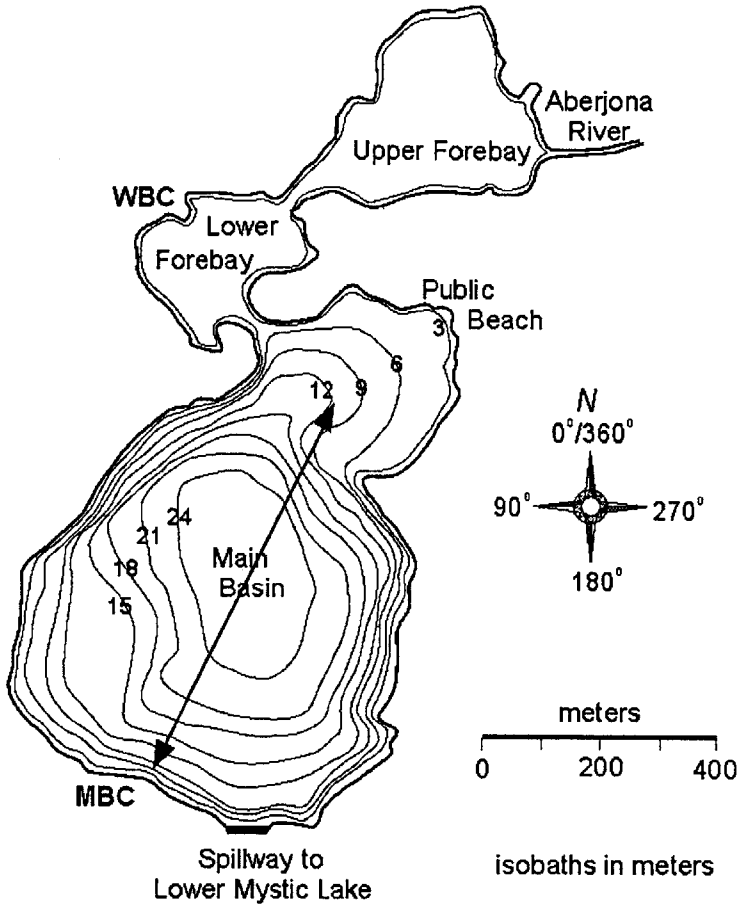

Figure 2-1: The Upper Mystic Lake (Winchester, MA), with depth contours plotted in 3 meter increments. The positions of the thermistor chains are labelled A,B,C, and the predominant wind forcing axis (oriented at approximately 340°/160°) is denoted by the solid arrow.

Spliethoff and Hemond 1996). The Aberjona river continues to bring contaminants such as arsenic, chromium, and lead into the Mystic Lake system at a rate of hundreds of kilograms per year (150 kg/year As, for example; Solo-Gabriele, 1995). Chemical studies of the UML have found concentrations of As and Cr on the order of 5 g/kg in the sediments (Spliethoff and Hemond, 1996), and As concentrations up to 0.1 μM in the water column (Trowbridge, 1995). The objective of the present study is to assess the potential contribution of internal seiching to the fluxes of contaminants in the UML. In particular, we investigate how the seasonal variation of seiche structure, especially at the bed, can lead to a temporal variation in these fluxes.

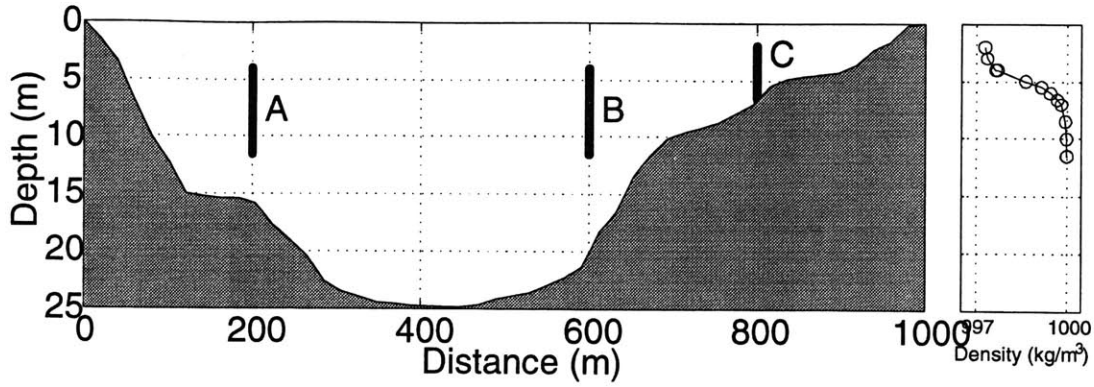

Figure 2-2: The bathymetry of the UML along the wind axis, with projections of the approximate locations of the thermistor chains. Wind data was collected at the Medford Boat Club (MBC) at the southern end of the lake.

2.3.2 Data collection and analysis

Temperature data was collected in the UML using thermistor chains at three locations (labeled A,B,C in Figure 2-1). Each chain consisted of six thermistors, with vertical spacings of 1.5 m for the chains at A and B, and 1.0 m at C. Based on previous studies (Trowbridge 1995, Aurilio *et al.* 1994), and using an understanding of typical mid-summer stratification conditions in the UML, the thermistors at A and B were placed to span an optimal region of the thermocline for observing seiche motions, running from the bottom of the surface mixed layer (approximately 4 m) to a depth of nearly 12 m. Below this depth the density gradient becomes sufficiently small that estimates of seiche amplitude based on thermistor records are unreliable. Chain C was located in the shallower part of the lake, and was therefore placed higher in the water column, from 2 m to approximately 6.5 m in depth. After deployment the bottom thermistor was found to be lying on the sediment. The exact depth of each system was determined using a pressure transducer mounted on the datalogger unit located at the top of each chain. The three systems were placed in a staggered arrangement to allow assessment of three-dimensional seiche motion. However, no transverse or rotational motion was detected in any of the data collected. Although transverse seiching can occur in principle, these modes did not feature in the UML internal wave spectra, most likely because the wind forcing consistently aligns with the major axis of the lake (see Figure 2-1), as discussed above. Temperature measurements were recorded

every five minutes. Concurrent wind (speed and direction) measurements were recorded at ten minute intervals by an anemometer placed roughly 12 m above the water surface atop a flag pole, at the Medford Boat Club at the southern end of the lake (MBC, Figure 2-1).

Previous thermistor chain studies (Trowbridge, 1995) have shown that the V1H1 (~0.6 cph) and V2H1 (~0.09 cph) modes are the dominant seiches in the UML. Since the V1H1 seiche is the focus of the current paper, motion associated with this mode is isolated from the temperature data by filtering around 0.6 cph (bandpass 0.3-0.9 cph). A sample of raw and filtered data from Chain C (i.e. over the shelf), along with the corresponding wind record, is presented in Figure 2-3 for a seven-day period in midsummer. The data show both the presence of sustained V1H1 and V2H1 oscillations, and the response to a transient forcing event. For example, the strong burst of wind at Jday 195.6 generated a sudden increase in the amplitude of the V1H1 mode. Comparison to the data collected at Chain A (Figure 2-4) shows that this response is substantially greater in the shallow part of the lake (Chain C) than in the main basin (Chain A), indicating localized magnification of fluid displacement in this region.

Thermistor chain data can be used to identify the internal wave modes present in a lake by matching observed seiche frequencies to model predictions, and (for the gravest modes) by comparing the phases of motions recorded at different locations in a lake. However, the overall sparsity of data, particularly in the horizontal, makes it difficult to develop a clear picture of the spatial structure of the seiches. The numerical model, however, provides a description of seiche structure over the entire longitudinal and vertical cross-section of the lake. Once the model solutions have been validated through comparison to the field data, they can be used to infer more detailed information about the structure and impact of the seiches.

To determine seiche amplitude from the thermistor data, a mean temperature profile $\overline{T}(z)$ is first constructed by averaging the time series temperature measurements in the selected time period and pooling the data from the three chains (Figure 2-5). An RMS temperature deviation ΔT_{rms} is then computed for the V1H1 mode from a selected length of filtered thermistor record (N points),

$$\Delta T^i_{rms} \equiv \sqrt{\frac{2}{N}\sum_{n=1}^{N}\left[T(\mathbf{x}_i,t_n)-\overline{T}(\mathbf{x}_i)\right]^2}\ , \qquad \overline{T}(\mathbf{x}_i)=\frac{1}{N}\sum_{n=1}^{N}T(\mathbf{x}_i,t_n)\ , \tag{10A}$$

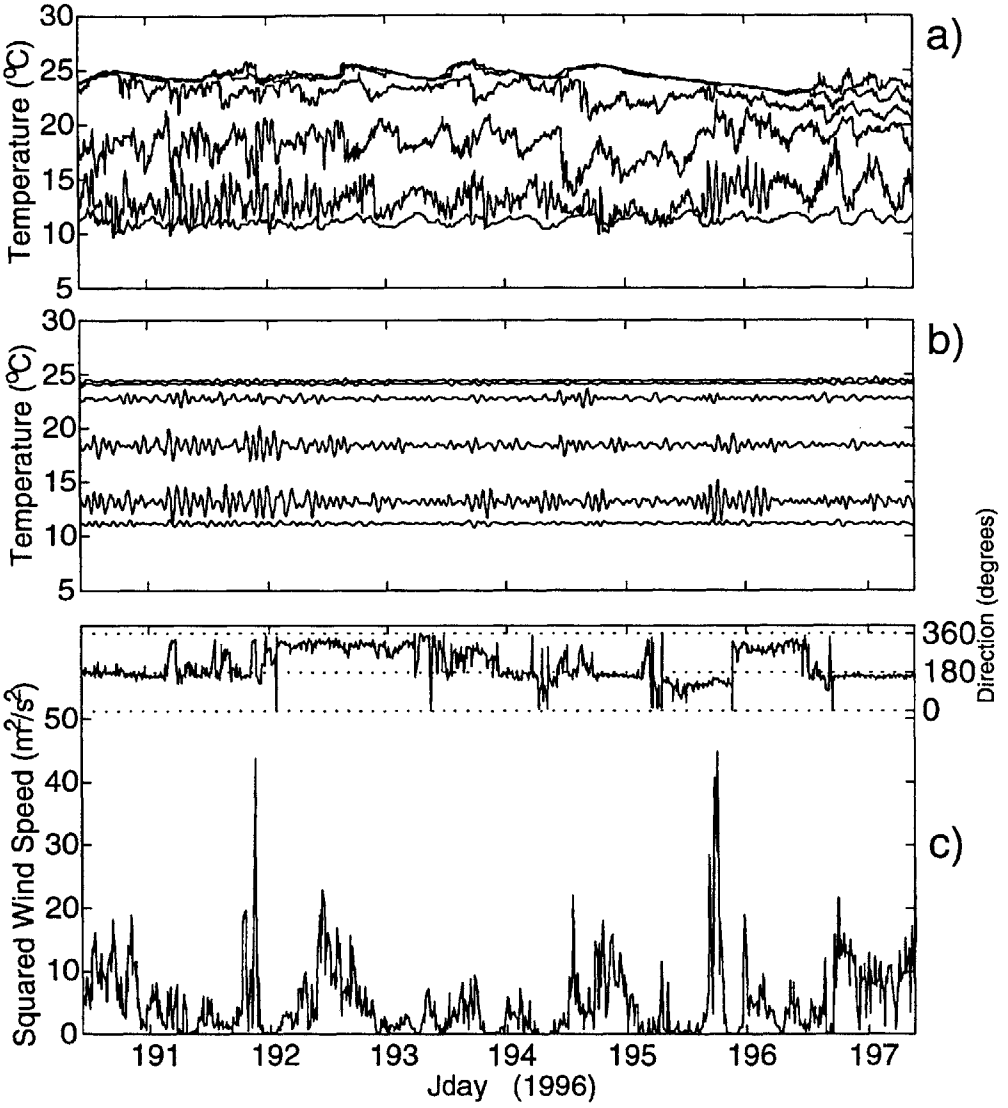

Figure 2-3: A sample of temperature data from thermistor chain C in the UML. a) Raw data for a seven-day period in July, 1996. The bottom thermistor in the chain was resting on the lake bed, giving rise to a damped signal. b) The same temperature record as a), after bandpass filtering (0.3-0.9 cph) around the V1H1 internal seiche period (0.6 cph). c) The simultaneous wind record, measured at the southern end of the UML. The wind direction is plotted in the inset at the top of the figure; 0° is North.

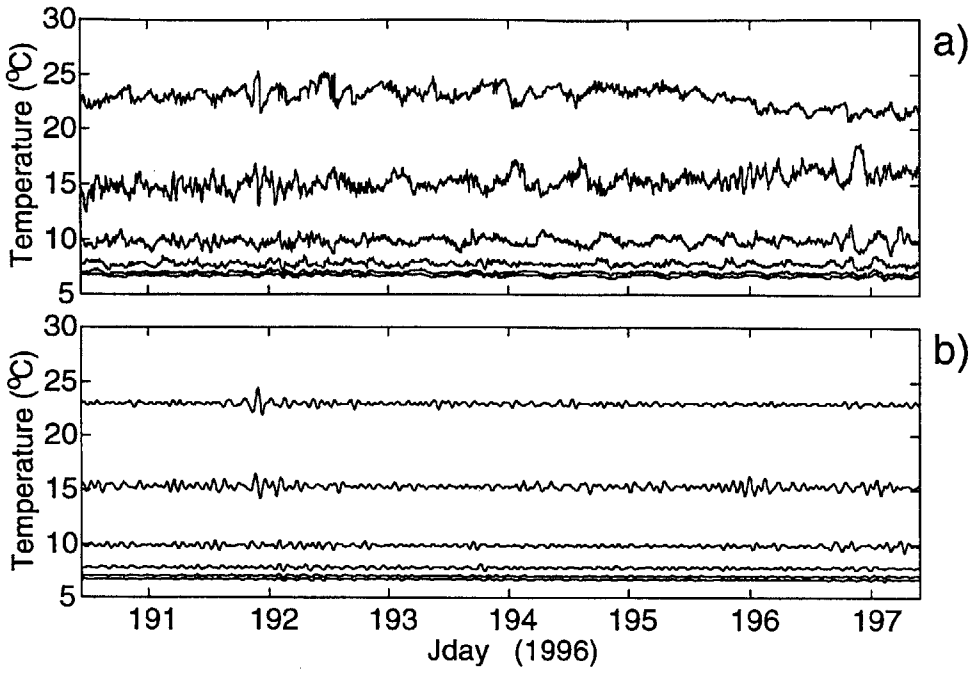

Figure 2-4: Thermistor data at Chain A, for the same time period shown in Figure 2-3. a) Raw data. b) The data in a), after bandpass filtering (0.3-0.9 cph).

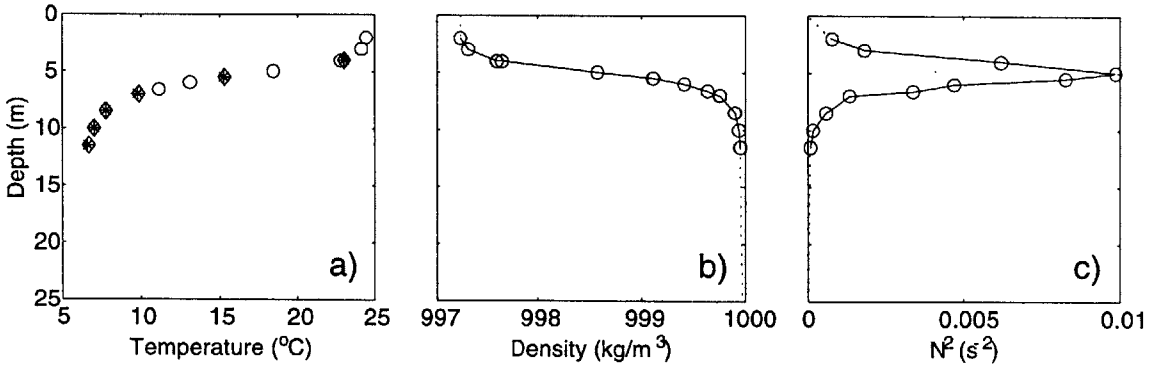

Figure 2-5: Mean temperature data derived from thermistor chains A,B,C for the time period shown in Figures 2-3 and 2-4 (Jday 191-197). a) Mean temperature at each thermistor on Chains A (*), B (◊), C (o). Chains A and B were positioned at the same depth in the water column. b) Mean densities at each thermistor, calculated from the data in figure a). The data from the three chains are assembled in a single profile (solid line); the data points at Chains A and B are averaged. The profile is extrapolated to the surface and to the bed (dashed lines). c) Buoyancy frequency profile derived from the temperature data in a).

where $\mathbf{x}_i$ denotes the position of thermistor i. The factor of 2 in this expression eliminates the factor of $\frac{1}{2}$ introduced by the summation, which is analogous to period averaging. Finally, RMS seiche amplitudes are determined as

$$\zeta^i_{rms} = \frac{\triangle T^i_{rms}}{\partial T/\partial z} \ , \tag{10B}$$

in which the local gradient $\partial\overline{T}/\partial z$ is estimated from the composite temperature profile (Figure 2-5). Note that the computed $\triangle T_{rms}$ profiles represent the envelope of wave motion for the V1 modes only, because for these modes the vertical fluid motions at any horizontal location are in phase throughout the water column, and the sign of $\left[T\left(t_n\right) - \overline{T}\right]$ at any instant in time t_n is the same for all the thermistors on each chain. For higher vertical modes, the $\triangle T_{rms}$ represent the absolute value of the wave envelope. Finally, note in equation 10AB that the RMS temperature deviations are assumed to correspond entirely to vertical fluid motions. In the thermistor chain data, however, horizontal displacements can also contribute to the observed $\triangle T_{rms}$ at locations where a strong vertical temperature gradient impinges on a sloping boundary. We therefore anticipate a divergence between the observed ζ_{rms} and the simulated ζ near the bed at Chain C.

2.4 Results and Discussion

2.4.1 Comparison to the model

The streamfunction contour plot shown in Figure 2-6 is the numerically-evaluated V1H1 seiche in the UML for the time period shown in Figure 2-3 (Jday 191-197). The basin shape used to compute this solution corresponds to the bathymetry along the major axis of the lake (see Figure 2-1), and the density profile, shown on the right, is an idealization based on the composite temperature profile shown in Figure 2-5. Simulated vertical profiles of ζ derived from this solution (Figure 2-6) using (2.7) are shown in Figure 2-7 for three longitudinal positions corresponding to the approximate locations of the three thermistor chains (see Figure 2-1, 2-2). The model profiles match those from the lake data. For the main basin profiles (A,B) the model correctly predicts two local maxima, one at the base of the surface mixed layer, and another

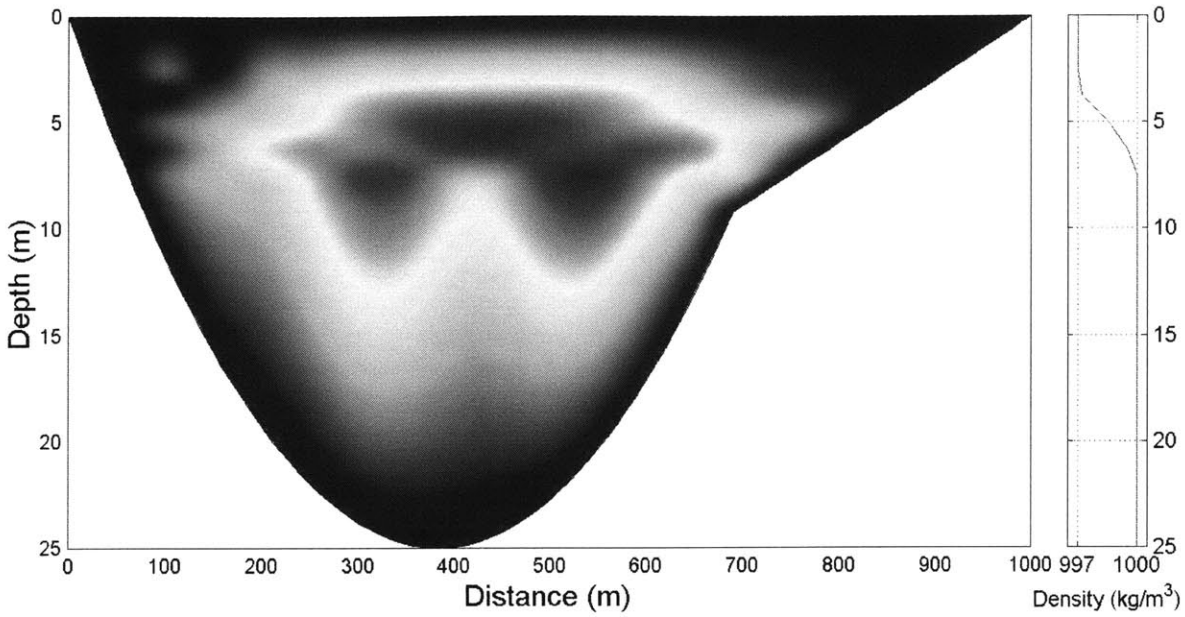

Figure 2-6: Streamfunction contours of the simulated V1H1 mode in the UML. The density profile used to generate this solution, shown on the right, is derived from the profile in Figure 2-5.

at an intermediate depth within the pycnocline. The RMS amplitudes at Chain A are slightly greater than those at B for the higher-lying peak, while the opposite is true for the deeper peak. The simulated profiles mirror this behavior. Over the shelf, the RMS amplitude at Chain C increases down to the bed in both the observed and modelled profiles. The differences in magnitudes directly at the bed probably arises because (10B) overpredicts the ζ_{rms} by neglecting the contribution of horizontal motions to the observed temperature variations, as discussed previously. The differences between the simulations and the data in the vertical positions and magnitudes of the peaks, are most likely due to differences between the real lake bathymetry (Figure 2-1) and the idealization (Figure 2-6), and to the low spatial resolution of the temperature measurements. Overall these results suggest that the numerical model provides a good description of the structure of the V1H1 internal seiche.

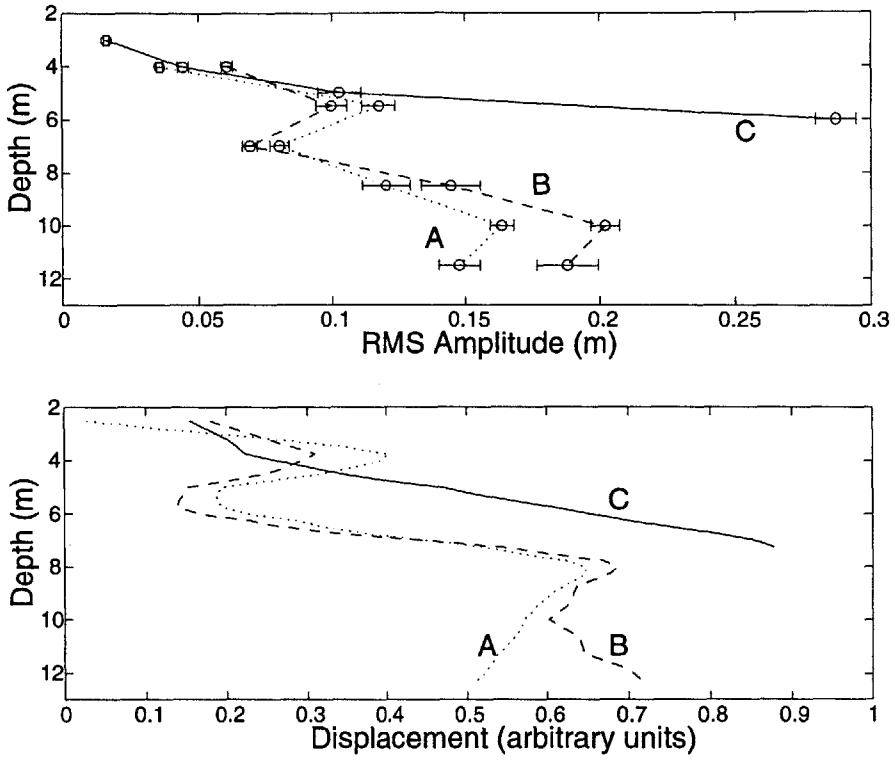

Figure 2-7: RMS vertical displacements at Chains A,B,C in the UML, using the data in Figures 2-3 and 2-4 for Chains C and A respectively, and the corresponding data for the same time period for Chain B. The bars indicate the estimated error, which primarily results from the computation of $\partial T/\partial z$ from the temperature profile. The model simulation, computed from the solution in Figure 2-6, is shown in the lower plot.

2.4.2 Stratification and bed velocities

To assess the potential impact of seiching on contaminant fluxes and resuspension, we focus on the structure of the V1H1-type seiche at the lake bed. In this section we use a parabolic basin to investigate the relationship between stratification and seiche-related bed velocities. The relative importance of other processes which affect sediment transport, such as river inflow and surface wave action, is not assessed here.

As lakes lose heat in the autumn, the breakdown in stratification can be characterized as a decrease in surface layer temperature and a deepening of both the epilimnion and the pycnocline. During this process, internal seiche structure (and climate) in the lake also changes. Although it was assumed that $\overline{\rho}(z)$ is not a function of time in the derivation of the governing equation

(2.3), the model may be used for this analysis if the timescale for significant changes in the density profile $\triangle\tau$ ($\sim$10 days) is much longer than the internal wave periods $2\pi\omega^{-1}$;

$$\frac{\nabla\cdot(\overline{\rho}_t\nabla\psi_t)}{\nabla\cdot(\overline{\rho}\nabla\psi_{tt})}\sim\frac{\triangle\overline{\rho}_0/\triangle\tau}{\overline{\rho}_0\omega}\sim\frac{\varepsilon}{\omega\triangle\tau}\ll 1\ ,$$

where $\varepsilon\equiv\frac{\triangle\overline{\rho}_0}{\overline{\rho}_0}\sim 0.003$. For modeling purposes, we describe the evolving stratification using a sequence of idealized density profiles comprised of a homogeneous epilimnion and hypolimnion connected by a linearly-varying pycnocline (see Figure 2-8, for example). These profiles can be parameterized in terms of the thicknesses of the epilimnion (h_{epi}) and pycnocline (h_{pyc}), and by the surface and hypolimnion densities. In this analysis we focus on the impact of changing layer thicknesses on seiche structure. Changes in surface temperature have a direct impact on seiche frequency, but only weakly affect seiche structure (on the order of the Boussinesq approximation), and are not considered here.

Figure 2-8 shows a series of V1H1 seiche solutions evaluated in a parabolic basin ($h(x)=1-(2x-1)^2$) for three different density profiles. As described earlier, the governing equation (2.3) is not scale-independent. In order to have the magnitudes of the Boussinesq and hydrostatic terms be of correct order it is necessary to use a vertical-to-horizontal aspect ratio which is typical of real lakes. The calculations are performed using the UML dimensions ($H=25m$, $L=1000m$) and densities ($\overline{\rho}(0)=997\,kg/m^3$ and $\overline{\rho}(H)=1000\,kg/m^3$), but the solutions are presented in normalized spatial coordinates. All of the solutions in Figure 2-8 were computed for an epilimnion depth of $h_{epi}=0.15H$. The pycnocline thickness is broadened sequentially by one grid point ($\triangle z=\frac{1}{40}$), with $h_{pyc}=0.18H$, $0.20H$, and $0.22H$ for figures a, b, and c respectively. The profiles are denoted ρ_1, ρ_2, and ρ_3 for convenience.

To demonstrate the connection between these streamfunction solutions and the more familiar velocity field, u and w are computed for the solution in Figure 2-8a, and plotted in Figure 2-9. The plot represents the spatial envelope of a standing wave, with the arrows reversing direction sinusoidally in time with the seiche frequency. This solution corresponds to the V1H1 mode in the rectangular basin. As this example illustrates, the V1H1 analogue can be identified in more complex basins by the absence of nodes (i.e. changes in sign) in the streamfunction contours in either the horizontal or vertical direction.

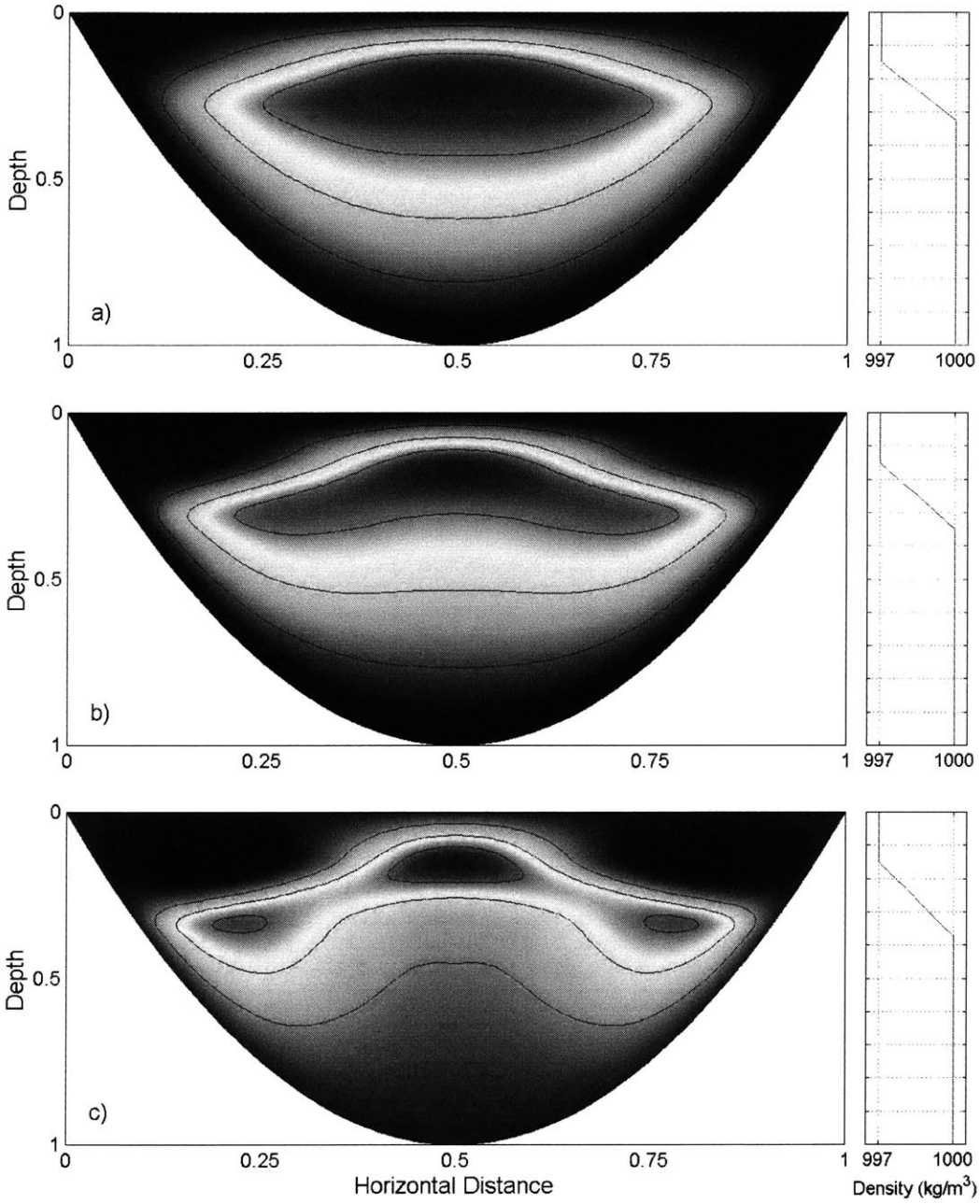

Figure 2-8: V1H1 seiche solutions evaluated in a parabolic basin. The density profiles used to compute each solution (shown on the right) are comprised of a surface mixed layer with thickness $h_{epi} = 0.15H$, and a pycnocline region which is broadened sequentially by one grid point ($\triangle z = \frac{1}{40}H$), from $h_{pyc} = 0.18H$ to $0.22H$. The lines show the $\psi = 0.25$, 0.5, 0.75 contours.

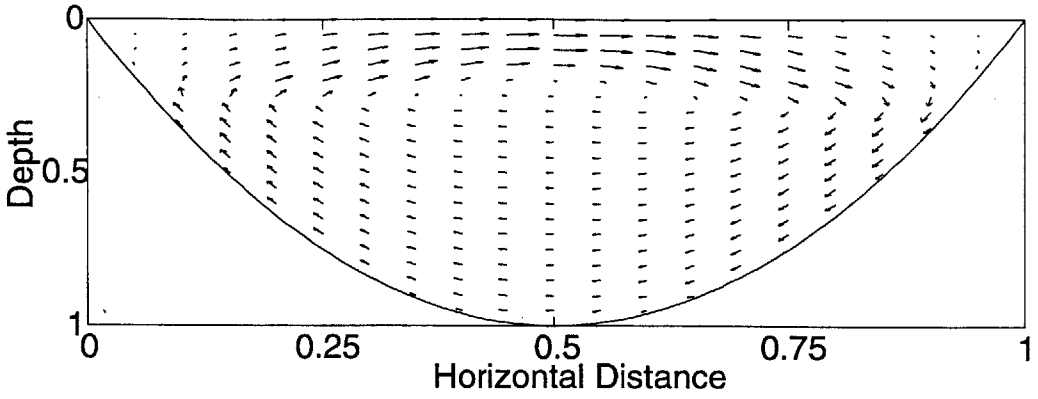

Figure 2-9: Velocity field derived from the V1H1 streamfunction solution in Figure 2-8a (see equation 3.52). The solution is computed for a 40×40 grid, but presented on a 20×20 grid for clarity.

The bed velocity distributions for the three solutions in Figure 2-8 are shown in Figure 2-10 (solid lines, labelled ρ_1, ρ_2, and ρ_3), along with three additional curves. The fourth solid line (ρ_{2L}) is the two-layer solution for $h_{epi} = 0.15H$. The dashed curves represent the two-layer solutions for epilimnion thicknesses of $h_{epi} = 0.25H$ and $0.35H$, and will be discussed below. In all cases the U_{bed} are normalized by the total energy of the seiche,

$$U_{bed} \equiv \frac{q_{bed}}{\sqrt{2E/\rho_0 V}} \ , \qquad q_{bed} = \sqrt{u_{bed}^2 + w_{bed}^2} \ , \tag{11}$$

where (due to equipartition of energies)

$$E = |E_{kin}| = \frac{1}{2}\int_V \overline{\rho}\left(u^2 + w^2\right) dxdz \qquad \text{and} \qquad \rho_0 V \equiv \int_V \overline{\rho} dxdz \ , \tag{12}$$

to allow direct comparison among the six cases. They are then rescaled to set the mid-lake maximum of the ρ_{2L} curve to unity, for convenience in illustrating the magnification of the flow. The velocity structures shown in Figure 2-10 clearly differ from rectangular basin solutions, for which U_{bed} ($\sim \sin\frac{\pi x}{L}$) has a maximum at the center of the lake regardless of stratification. For the parabolic basin considered here, the maximum U_{bed} only occurs at mid-lake when the pycnocline is exceptionally thin, as the two-layer solution shows (ρ_{2L}). As the pycnocline thickness increases, U_{bed} makes the transition to the two-peaked profiles seen for ρ_1 to ρ_3.

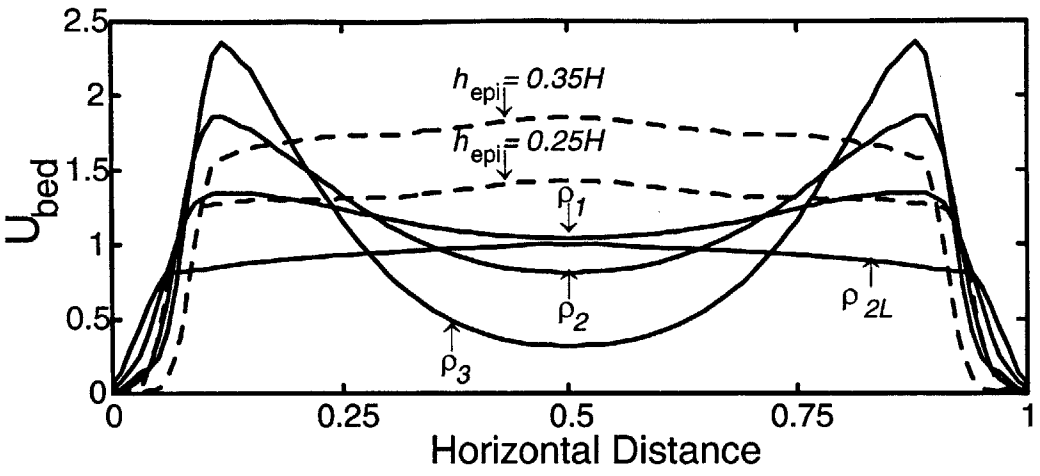

Figure 2-10: Bed velocities derived from the solutions in Figure 2-8, plus three additional solutions. To generate the curves, the streamfunction contours were first interpolated onto a finer grid and then used to compute $q_{bed} = \sqrt{u_{bed}^2 + w_{bed}^2}$ using equation 3.52. Residual steppiness was smoothed with five-point averaging. The curves were normalized as in equation 11, and then rescaled by the maximum value of the ρ_{2L} solution. The solid lines were all computed with $h_{epi} = 0.15H$, and show the evolution of bed velocity with increasing pycnocline thickness ($h_{pyc} = 0$ (ρ_{2L}), $0.18H$ (ρ_1), $0.2H$ (ρ_2), $0.22H$ (ρ_3)). The dashed lines were computed using two-layer density profiles ($h_{pyc} = 0$), with $h_{epi} = 0.25H$ and $0.25H$. Along with the ρ_{2L} solution, these curves show the changes in U_{bed} with increasing epilimnion depth.

Making the simple assumption that sediment is scoured from regions of high bed velocity and deposited in locations of lower bed velocity, the off-center maxima imply that sediment will be carried not just toward the 'edges' of the lake, but also toward the center. Furthermore, moving from ρ_1 to ρ_3 (i.e. increasing h_{pyc}), we see a substantial increase in the maximum value of U_{bed} around $x = 0.1$ and 0.9, and a dramatic decrease in velocity at mid-lake, as the bottom of the lake is progressively cut off from the seiche motion. In fact, the results in Figure 2-10 suggest that there is a density profile for which U_{bed} at the center of the lake drops to zero. In this respect, the bed velocity structures in the (more realistic) parabolic basin differ substantially from the corresponding rectangular basin solutions for these stratification profiles.

To estimate the damping rate for the internal seiches, we assume that the seiche energy is dissipated predominantly through bed shear. The E defined in 12 is the energy (per unit width) for an inviscid system, and is therefore constant over time. If we assume that the viscous

Profile	k/k_{2L}
ρ_{2L}	1.0
ρ_1	2.4
ρ_2	3.4
ρ_3	4.2
$0.25H$	2.0
$0.35H$	5.0

Table 2.1: Damping coefficients for the six density profiles in Figure 2-10. The k are evaluated as in equation 13 and normalized by the two-layer solution. The rate of seiche damping increases both as the pycnocline is broadened and as the epilimnion depth is increased.

damping of the seiches has small magnitude, we can permit a small transient component to E and estimate the dissipation of energy using a first-order model,

$$\frac{dE}{dt} = -kE \ .$$

This is then balanced by the work done at the bed (coordinate s):

$$-kE = \int_{\partial} \tau_{bed} U_{bed} ds \ .$$

The bed stress can be taken as $\tau_{bed} = \overline{\rho} C_b U_{1m}^2$ (i.e. U at 1m) with $C_b = 0.005$ (Dimai *et al.*, 1994). Using the bed velocities in Figure 2-10 as representative of U_{1m}, we then find

$$k = \frac{C_b \int_{\partial} \overline{\rho} U_{bed}^3 ds}{\int_V \overline{\rho} \left(u^2 + w^2\right) dx dz} \ . \tag{13}$$

The relative damping coefficients for each of the six cases is shown in Table 1. Each k is normalized by the two-layer ($h_{epi} = 0.15$) solution. We see that the damping rate for the seiches increases four-fold as the metalimnion is broadened and the bed velocities at the base of the pycnocline increase. Likewise, for the two-layer profiles, as the interface moves closer to the bed we see a substantial increase in k. These results illustrate the effect of internal seiche structure on energy dissipation, and show that the attenuation of the seiching is controlled in part by stratification and bathymetry. This clearly has an impact on the seasonal variation in seiche activity.

Returning to Figure 2-8, note that the seiche develops a ray-like structure as the thickness

of the pycnocline increases (ρ_1 to ρ_3). Figure 2-8c in particular suggests that the model system is approaching a critical behavior, as the seiche energy is confined to a narrow conduit within the water column, i.e. along the streamfunction contours. These observations are suggestive of the results obtained by Maas and Lam (1995), in which internal waves were evaluated using a geometric wave ray technique. For uniform stratification (constant N), they concluded that for most bathymetries the internal wave rays (i.e. energy) generated within the lake become focused along specific lines, called attractors. The trend in Figure 2-8 suggests that the system may be converging toward such focusing behavior. Maas and Lam demonstrated that wave ray focusing is typical in constant-N systems, so that coherent internal seiches are the exception rather than the norm in a uniform stratification. For the systems we consider ($N \approx$ constant in the pycnocline and $N = 0$ in the surface and lower layers), when the pycnocline is thin the shape of the 'waveguide' region in which the wave rays can propagate approximates an elongated bucket with slightly rounded sides. From Maas and Lam, the bucket-shaped basin (flat bed with linear sloping side walls) is one of the few constant-N systems which permits seiche solutions. Although these two configurations are not exactly equivalent (because they have different boundary conditions; the BC $\psi = 0$ applies at the free surface and the bed, not at the boundary of the pycnocline), the geometric similarity strongly suggests a correspondence between their seiche solutions. In addition, in our numerical calculations, as h_{pyc} is increased beyond that in ρ_3 by one or more additional grid points and the system makes the transition to wave ray focusing, we no longer obtain smooth V1H1 solutions like those in Figure 2-8. This is consistent with the conclusions of Maas and Lam (1995), who contend that systems which are subject to focusing are poorly described by discretization methods. It is not possible to make a direct comparison between the cases considered here (i.e. profiles for which focusing does not occur, and coherent seiche solutions are found) and the results of Maas and Lam, however, since these authors only considered uniform stratification.

Regarding the above observation of an apparent approach toward a critical behavior, viscous and nonlinear processes, which were omitted from the present formulation, will likely prevent this behavior from occuring in real systems (as Maas and Lam (1995) also note in their analysis). Specifically, as the seiche energy becomes more focused and velocities are increasingly magnified, nonlinearity and viscosity become important and lead to greater damping. This can be seen

from the results above (Table 1), in which the increases in h_{pyc} led to a four-fold increase in the decay rate k. The impact of nonlinear terms can be inferred from the curves in Figure 2-10; as U_{bed} increases at the base of the pycnocline, the advective terms $\sim U_{bed} \cdot \partial U_{bed}/\partial s$ grow substantially.

Along with the ρ_{2L} curve, the dashed lines in Figure 2-10 show the evolution of bed velocities with changing surface layer depth, h_{epi}. Two-layer density profiles were used in these calculations to isolate the changes in bed velocity structure due to increasing h_{epi}. The trends were found to be qualitatively similar for all values of h_{pyc}. As the epilimnion deepens, the bed velocities show a steady increase in the deepest part of the lake. This result is easily explained using a simple depth-averaged perspective. As the thickness of the lower layer decreases, conservation of mass requires that the flow at the bottom of the lake increases relative to the upper layer, $u_2 = -\frac{h_1}{h2}\, u_1$. Normalizing by the system energy then gives $\frac{|u_2|}{\sqrt{E/\rho_0 V}} = \sqrt{\frac{2h_1}{h2}}$, which predicts increases in $|u_2|$ ($\sim |U_{bed}|$) of 40 per cent and 75 per cent as h_{epi} is increased respectively from $0.15H$ to $0.25H$, and from $0.15H$ to $0.35H$. These increases are very close to the results in Figure 2-10.

We conclude by noting that the 2D model used in the present study effectively reduces to the method of Yang and Yih (1976) when a two-layer stratification is used. Therefore, the results in Figure 2-10 (i.e. the qualitative and quantitative differences between the two-layer and ρ_1, ρ_2, ρ_3 curves) also illustrate some of the differences between two-layer models and the numerical technique used here (with continuous stratification). For example, the magnification of U_{bed} associated with the development of a ray-like seiche structure clearly cannot occur in two-layer systems. The figure thus demonstrates the importance of an accurate description of vertical structure, and of the limitations of a two-layer perspective.

2.4.3 Bathymetry and bed velocities

In this section we investigate the dependence of bed velocities on bathymetry, using a series of basins ranging from rectangular to parabolic. The bathymetry in each case is given by

$$h(x) = \frac{\cosh\alpha - \cosh\alpha\,(2x-1)}{\cosh\alpha - 1} \qquad \begin{array}{l} h(0) = h(1) = 0 \\ h\left(\frac{1}{2}\right) = 1 \end{array} ,$$

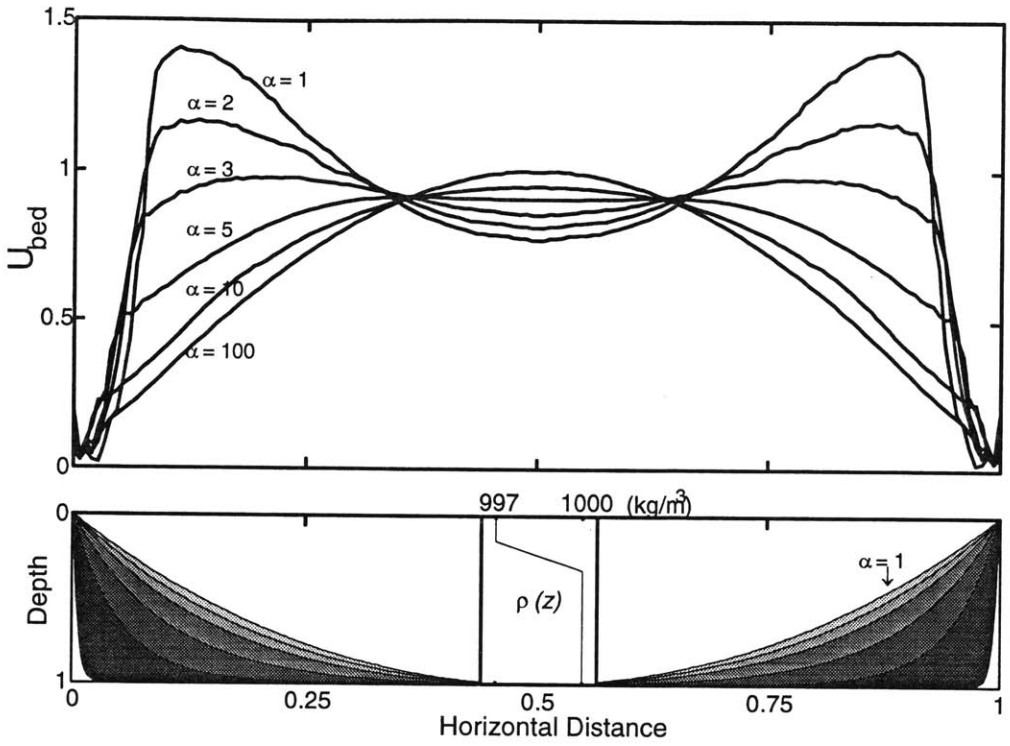

Figure 2-11: Bed velocity versus horizontal distance for six basins of varying concavity ($\alpha = 1, 2, 3, 5, 10, 100$). The corresponding bathymetries are shown in figure b). The curves were generated and processed the same way as those in Figure 2-10, and subsequently were rescaled by the maximum (i.e. mid-lake) value for the rectangular basin soution ($\alpha \rightarrow \infty$).

and is parametrized in terms of the variable α, which corresponds to an index of concavity. The two extreme basin shapes are given by $\alpha \rightarrow 0$ (parabola $h(x) \rightarrow 1 - (2x-1)^2$) and $\alpha \rightarrow \infty$ (rectangle). The density profile is the same as the profile in Figure 2-8a.

Figure 2-11 shows the bed velocity profiles computed for six configurations ($\alpha = 100, 10, 5, 3, 2, 1$). The corresponding basin shapes are also shown. The U_{bed} are once again normalized as described in equation 11, and then rescaled to set the mid-lake maximum U_{bed} of the rectangular basin solution to unity. Moving from $\alpha = 100$ ($\sim$rectangular) to $\alpha = 1$ ($\sim$parabolic), a region of substantially enhanced velocities develops at two locations, where the base of the pycnocline reaches the bed. While U_{bed} at the center of the lake decreases by 20 per cent, the velocities at $x \simeq 0.1$ and 0.9 increase by approximately a factor of 5, ultimately becoming as much as 50 percent greater than U_{bed} at mid-lake. We anticipate substantially different sedimentation

patterns for each of the six cases. In particular, for the nearly-rectangular bathymetry the observed distribution of U_{bed} will tend to carry sediment away from the center of the lake, causing a build-up at the 'corners' of the basin. For the parabola, on the other hand, the off-center maxima cause sediment to be carried both toward the edges of the lake, and to the center. Furthermore, for the same total seiche energy, the scouring is greatest in the metalimnion region of the parabolic basin because the highest bed velocities are generated in that system.

2.4.4 Seasonal variation of bed velocities in the UML

Because of the high level of contaminants in the sediments of the UML, the enhanced benthic mixing, dissolution, and transport associated with the internal seiches can be an important factor contributing to the water quality of the lake. And because the seiches vary seasonally (in structure and climate), their contribution to contaminant (and nutrient) fluxes will also vary with time. In this section we assess the temporal changes in bed velocity for the V1H1 seiche arising from the autumnal changes in stratification in the UML.

Bed velocities for three different stratification profiles are shown in Figure 2-12 (solid lines). The representation of the UML bathymetry (dashed line) which was used to compute these solutions is laid over the velocity curves. The velocities are again normalized by the total seiche energy (equation 11), and subsequently rescaled by the overall maximum value of the three solutions. The density profiles are comprised of a surface mixed layer, a linearly-varying pycnocline, and a homogeneous hypolimnion (inset, Figure 2-12), and represent an idealization of the autumnal breakdown in stratification, based on profiles measured on 8/21, 10/13, and 11/4, in 1992 (Aurilio *et al.*, 1994). When the pycnocline is relatively high in the water column (08/21), the region of magnified flow extends over a broad region of the shoal in the northern end of the lake (right side of the plot). As the lake cools and the mixed layer deepens (10/13), the maximum amplitude of U_{bed} remains essentially unchanged, but the region of amplified flows becomes localized to a much narrower region of the shelf. This suggests that the fluid further up on the shelf becomes disconnected from the seiching motion. Finally, when the lake cools still further and the pycnocline drops below the level of the shelf (11/4), the amplified flows over the shelf disappear, and an increase in main basin flows is observed. At this point the entire shelf is disconnected from seiche-induced flows.

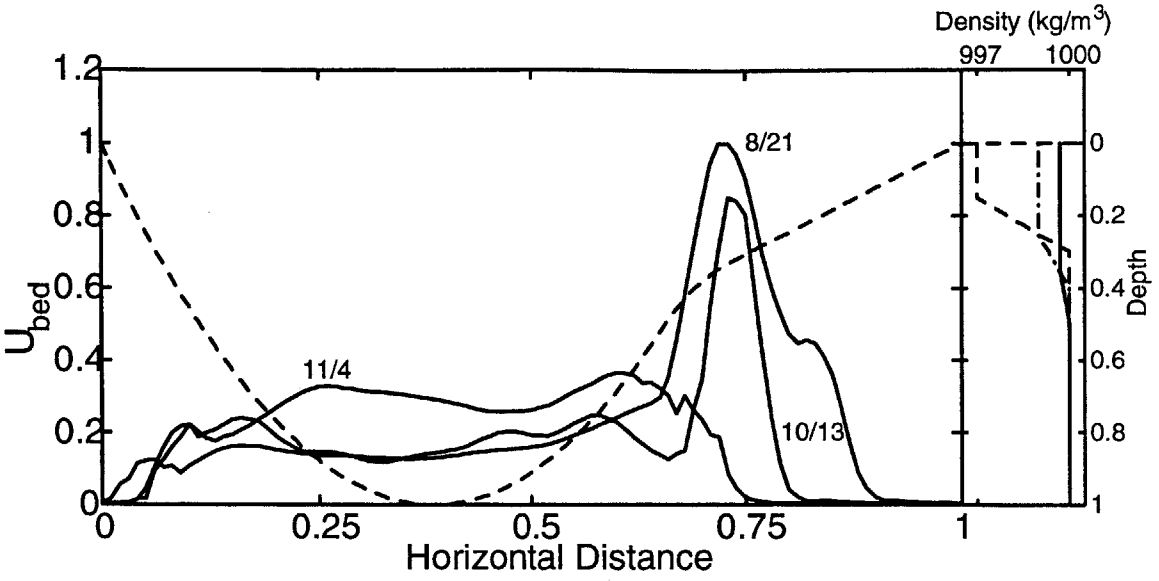

Figure 2-12: Bed velocities for three different density profiles which simulate the seasonal evolution of stratification in the UML (from Aurilio *et al.*, 1994); the curves are labeled with the dates on which the density profiles were measured. The idealized density profiles used to generate these solutions are shown in the inset figure, and the model UML bathymetry used in the computations is also shown (dashed line). The data were generated the same way as in Figures 2-10 and 2-11, but rescaled in this case by the maximum overall value on the data set (8/21 curve, at $x \simeq 0.75$).

The observed temporal evolution of the maximum U_{bed} and the migration of the magnified flow region can play significant roles in the annual influx of contaminants to the UML. Metal-laden sediments enter the system from a river inlet near the northern end of the lake (right side, Figure 2-2), arriving first at the shelf. The seasonal strong winds that begin in the autumn coincide with the changes in U_{bed} described above. Although an exact prediction of the magnitude of the V1H1 seiche (or indeed any seiche) requires specific information about wind forcing, we nonetheless know qualitatively that the V1H1 seiche is strongly excited in the UML during the fall. We therefore conclude that the bed motions outlined in Figure 2-12 may have a substantial impact on the initial deposition and subsequent mobilization of contaminants in the lake. Future field studies of sediments in the UML will explore the link between seiching and sediment distribution.

2.5 Conclusions

The results presented here show that internal seiche structure is highly dependent on both bathymetry and stratification. Simpler lake models which use a rectangular basin and/or two-layer stratification formulation, which are frequently used for convenient characterizations of seiche motion, provide poor descriptions of even the basic qualitative features of seiches. For example, the V1H1 vertical motions observed and modeled in the UML differ substantially from rectangular basin structure functions. The accurate modeling of seiches therefore requires the use of realistic density profiles and basin shapes.

In this paper we have assessed the effects of bathymetry and stratification on seiche structure. A 2D numerical model was used to compute a finite set of seiche eigensolutions in systems with variable bathymetry and continuous stratification. Each solution yields a description of the entire velocity or displacement field of the seiche, and can thus be used to augment the extremely limited spatial information provided by thermistor chain data. The model can therefore be a valuable tool for interpreting field observations. In addition, the entire set of computed eigenmodes can also be used as a basis for describing the composition of internal seiche data, both in the field and from hydrodynamic model simulations.

The dependence of seiche structure on stratification was investigated using a series of density profiles in a parabolic basin. The results show that the depth of the epilimnion (h_{epi}) and the thickness of the pycnocline (h_{pyc}) affect both the magnitude and the distribution of bed velocities. The observed variation in U_{bed} as a function of h_{epi} is easily explained by conservation of (horizontal) volume flux throughout the water column. The dependence of U_{bed} on h_{pyc} is somewhat more complicated, however. Except for cases where the pycnocline is exceptionally sharp (tending to a discrete interface), the maximum bed velocities occur where the base of the pycnocline intersects the bed, and the center of the lake corresponds to a local minimum in U_{bed}. Furthermore, as the pycnocline thickness increases, the U_{bed} maxima are magnified while the velocity at mid-lake drops toward zero, and the deepest part of the lake becomes cut off from the seiching motion. The net effect of this evolution in bed velocities is an increase in the damping rate of the seiches (k) with increasing h_{pyc}. This is in complete contrast to the rectangular basin model results, which predict a single velocity maximum at mid-lake for the V1H1 mode (i.e. $U \propto \sin\frac{\pi x}{L}$) for all stratification conditions. This implies that basin shape

also plays an important role in determining seiche structure. The dependence on bathymetry was confirmed by computing the V1H1 seiche solutions for a single density profile in a series of basins of varying concavity. As the basin shape was changed from rectangular to parabolic, the computed U_{bed} evolved smoothly from the single mid-lake maximum curve into the two-peaked distribution described above. By altering the magnitude and spatial distribution of the boundary shear, the basin shape influences the long-term fate of sediments and the damping of internal seiche motion.

Application of the model to the UML demonstrated the potential impact on bed velocities of the autumnal stratification breakdown. The most important consequence of the changing conditions in the lake is the migration of the magnified bed-flow region. During the summer the maximum bed velocity peak is located on the shelf, and is relatively broad. Moving into the fall, as the surface layer deepens and the pycnocline begins to broaden, the region of elevated velocity narrows. Ultimately, as the base of the pycnocline deepens and drops below the shoal, the flows over the shelf disappear altogether . This variation in U_{bed} has potentially important consequences for the transport of contaminants in the UML. Contaminant-laden sediment entering the lake is initially deposited over the shelf. The timing and magnitude of the remobilization of these contaminants depend strongly on the bed velocities over the shelf, and therefore on the spatial structure and temporal evolution of the seiche.

2.6 Acknowledgments

The authors gratefully acknowledge the help of the Winchester Boat Club, which made its facilities, and some of its members, available for the deployment of equipment and the routine collection of data. We also thank the Medford Boat Club for providing a site for wind data collection. We thank Hrund Andradóttir, Gordon Ruggaber, and Enrique Vivoni for their help deploying the thermistor chains and anemometer. Helpful comments from Prof. Ole Madsen regarding interpretation of the data were greatly appreciated. This research was funded by NIEHS, grant number P42-ES04675.

Bibliography

[1] Aurilio, A. C., R. P. Mason, and H. F. Hemond, 1994. Speciation and fate of arsenic in three lakes of the Aberjona Watershed. *Env. Sci. and Tech.* **28**(4): 577-585.

[2] Birchfield, G. E., 1969. Response of a Circular Model Great Lake to a Suddenly Imposed Wind Stress. *J. Geophys. Res.* **74**: 5547-5554.

[3] Csanady, G. T., 1968. Wind-Driven Summer Circulation in the Great Lakes. *J. Geophys. Res.* **73**: 2579-2589.

[4] Csanady, G. T., 1968. Motions in a Model Great Lake Due to a Suddenly Imposed Wind. *J. Geophys. Res.* **73**: 6435–6447.

[5] Csanady, G. T., 1972. Response of Large Stratified Lakes to Wind. *J. Phys. Oceanogr.* **2**: 3–13.

[6] Csanady, G. T., 1982. On the Structure of Transient Upwelling Events. *J. Phys. Oceanogr.*, **12**: 84-96.

[7] Defant, A., 1918. Neue Methode zur Ermittlung der Eigenschwingungen von abgeschlossenen Wassermassen. *Ann. Hydrogr. Berlin* **46**: 78-85.

[8] Defant, A., 1960. Physical oceanography. Pergamon, London, vol. II, 598 pp.

[9] Dimai, A., M. Gloor, and A. Wüest, 1994. Bestimmung der Intensität von Turbulenz in der Bodengrenzschicht von Seen. *Limnologica* **24**(4): 339-350.

[10] Durant, J. L., J. J. Zemach, and H. F. Hemond, 1990. The History of Leather Industry Waste Contamination in the Aberjona Watershed: A Mass Balance Approach. *Civil Engineering Practice*, Fall 1990: 41-65.

[11] Gloor, M., A. Wüest, and M. Münnich, 1994. Benthic boundary mixing and resuspension induced by internal seiches. *Hydrobiologia* **284**: 59-68.

[12] Haury, L.R., P.H. Wiebe, M.H. Orr, and M.B. Briscoe, 1983. Tidally generated high-frequency internal wave packets and their effects on plankton in Massachusetts Bay. *J. Mar. Res.*, **41**: 65-112.

[13] Heaps, N. S., and A. E. Ramsbottom, 1966. Wind effects on water in a narrow two-layered lake. *Phil. Trans. Roy. Soc. London* ser **A 259**: 391-430.

[14] Heinz, G., Johann Ilmberger, and Michael Schimmele, 1990. Vertical Mixing in Überlinger See, western part of Lake Constance. *Aquat. Sci.* 52/3: 256-268.

[15] Horn, W., C. H. Mortimer, and D. J. Schwab, 1986. Wind-induced internal seiches in Lake Zürich observed and modeled. *Limnol. Oceanogr.* **31**(6): 1232-1254.

[16] Ivey, G. N., and G. M. Corcos, 1982. Boundary mixing in a stratified fluid. *J. Fluid Mech.*, **121**: 1-26.

[17] LaZerte, B. D., 1980. The dominating higher order vertical modes of the internal seiche in a small lake. *Limnol. Oceanogr.* **25**(5): 846-854.

[18] Lemmin, U. and C. H. Mortimer, 1986. Tests of an extension to internal seiches of Defant's procedure for determination of surface seiche characteristics in real lakes. *Limnol. Oceanogr.*, **31**(6): 1207-1231.

[19] Levy, D. A., R. L. Johnson, J. M. Hume, 1991. Shifts in fish vertical distribution in response to an internal seiche in a stratified lake. *Limnol. Oceanogr.*, **36**(1): 187-192.

[20] Maas, L. R. M., and F.-P. A. Lam, 1995. Geometric focusing of internal waves. *J. Fluid Mech.*, **300**: 1-41.

[21] MacManus, J. and R. W. Duck, 1988. Internal seiches and subaqueous landforms in lacustrine cohesive sediments. *Nature*, **334**: 511-513.

[22] Monismith, S. G., 1985. Wind-forced motions in stratified lakes and their effect on mixed-layer shear. *Limnol. Oceanogr.*, **30**(4): 771-783.

[23] Monismith, S., 1987. Modal response of reservoirs to wind stress. *J. Hydr. Eng.*, **113**(12): 1290.

[24] Mortimer, C. H., 1979. Strategies for Coupling Data Collection and Analysis with Dynamic Modelling of Lake Motions. Hydrodynamics of Lakes, W. H. Graf and C. H. Mortimer eds. pp. 183-222.

[25] Münnich, M., A. Wüest, and D. M. Imboden, 1992. Observations of the second vertical mode of the internal seiche in an alpine lake. *Limnol. Oceanogr.*, **37**(8): 1705-1719.

[26] Münnich, M., 1996. Influence of bottom topography on internal seiches in stratified media. *Dyn. Atmos. Oceans*, **23**: 257-266.

[27] Pierson, D. C. and G. A. Weyhenmeyer, 1994. High resolution measurements of sediment resuspension above an accumulation bottom in a stratified lake. *Hydrobiologia* **284**: 43-57.

[28] Schwab, D. J., 1977. Internal free oscillations in Lake Ontario. *Limnol. Oceanogr.* **22**(4): 700-708.

[29] Solo-Gabriele, H, 1995. Metal Transport in the Aberjona River System: Monitoring, Modeling, and Mechanisms. Ph.D. thesis, MIT.

[30] Spliethoff, H. M., and H. F. Hemond, 1996. History of toxic metal discharge to surface waters of the Aberjona Watershed. *Env. Sci. Technol.*, **30**(1): 121-128.

[31] Trowbridge, P. R., 1995. Rapid Redox Transformations of Arsenic and the Characterization of the Internal Seiches in the Upper Mystic Lake, Medford, Massachusetts. S.M. thesis, MIT.

[32] Turner, J. S., 1973. Buoyancy Effects in Fluids. Cambridge University Press.

[33] Wedderburn, E. M., 1907. The temperature of the fresh water lochs of Scotland, with special reference to Loch Ness. *Trans. Roy. Soc. Edinburgh*, **45**: 407-489.

[34] Wedderburn, E. M., 1912. Temperature observations in Loch Earn; with a further contribution to the hydrodynamical theory of temperature oscillations. *Trans. Roy. Soc. Edinburgh*, **48**: 629-695.

[35] Wiegand, R. C. and V. Chamberlain, 1987. Internal waves of the second vertical mode in a stratified lake. *Limnol. Oceanogr.*, **32**(1): 29-42.

[36] Yang, W. H, and C.-S. Yih, 1976. Internal waves in a circular channel. *J. Fluid Mech.*, **74**: 183-192.

[37] Yih, C.-S., 1980. Stratified Flows. Academic Press.

Chapter 3

Viscous damping of internal seiches

Abstract

We present an analysis of the viscous damping of internal seiches in lakes, using a perturbation technique based on the addition of a benthic boundary-layer flow to the inviscid velocity field. The resulting expression for the decay rate (α) can be interpreted physically as the rate of bed stress working by the seiche on the bed, and corresponds to the integral of seiche kinetic energy at the bed (or more accurately, within the benthic boundary layer) modified by a coefficient which describes the effects of buoyancy and bathymetry. Numerical (inviscid, two-dimensional) V1H1 seiche solutions are used to compute α for a series of idealised basins. We find that the buoyancy factor gives rise to a $\sim$20% increase in α, except for the rectangular basin model, in which buoyancy effects are confined to vanishingly small contributions at the vertical end walls. Further exploration of the boundary layer structure shows that the magnification of the α is caused by a decrease in the shear length (δ'), the distance over which the outer flow velocity drops to zero at the bed. The relationship between δ' predicted by our model and stratification is also explored.

3.1 Introduction

The decay of standing waves in containers and basins has been studied extensively over the past few decades. Johns (1968) evaluated the damping of interfacial waves for a two-layer fluid system, using a perturbation technique based on the addition of a viscous boundary-layer flow to the inviscid velocity field. The decay rate (α) is computed as the complex portion of the leading-order perturbation of the wave frequency (ω). Dore applied the same method to the decay of both surface waves (1968a) and internal waves in an arbitrarily stratified fluid (1968b, 1969). However, he restricted attention to constant-depth systems, and thus gained no insight into the effects of bathymetry. Mei and Liu (1973) computed damping rates for surface waves in an arbitrarily-shaped basin, and included the effects of a meniscus region to resolve problems with singularities which arise in the asymptotic expansion at the basin walls on the free surface (Ursell, 1952). Kerswell and Barenghi (1995) used the method to evaluate decay rates for inertial modes in a rotating cylinder. The perturbation method employed in these studies is summarised concisely by Mei (1989; page 395) for surface waves, with results computed for several examples, including seiches in simple basins.

A number of researchers have computed wave and seiche decay rates using a simplified linearised bed stress relation ($\tau \propto u$) with friction coefficient, with a resulting perturbation analyses similar to the boundary-layer method described above. For example, Orlič (1984) computed decay times for rotational waves in a two-layer fluid in a rectangular channel, using depth-averaged equations and a linear bed stress relation in the momentum. Hukuda (1986) used the same method to study surface seiches in 3D parabolic and elliptical basins, for which the zeroth order systems can be solved analytically. And Craig (1991) studied the damping of internal waves in open systems using both conventional stress terms in the momentum equations as well as a linearised stress relation for the bed boundary conditions. In addition to these perturbation techniques, α can also be computed using physical arguments based on the assumption of linear energy decay. Henderson and Miles (1994) evaluated the damping of surface waves in cylinders as the rate of stress working by the wave system on the boundary. Mei and Liu (1973) showed that the results of their perturbation analysis could be interpreted equivalently as the rate of pressure working by the surface waves on the top of the bed/wall boundary layers.

Here, we begin by presenting a generalised analysis of the damping of longitudinal (two-dimensional) internal seiches in lakes with arbitrary bathymetry and non-uniform stratification. An expression for seiche decay rates is first derived using the boundary-layer perturbation analysis described above. This is followed by a comparison to several physically-based derivation methods, which reveals the equivalence of the different techniques. We find that the decay rate for internal seiches is similar to the homogeneous fluid result, but includes an additional factor which accounts for effects due to buoyancy and bathymetry. Since α is proportional to the kinetic energy at the bed (i.e. within the benthic boundary layer) at leading order, determination of the damping rate requires an accurate estimate of bed velocity structure. As we shall see, simplified models such as the rectangular basin provide inadequate description of u_{bed}. We therefore compute a series of numerical two-dimensional seiche solutions (for the V1H1 mode) using an eigenvalue method (Fricker and Nepf, 2000).

The increase in the damping rate for internal seiches (versus α when buoyancy effects are neglected) is most easily interpreted using the bed stress perspective (Henderson and Miles 1994). Within the pycnocline, the magnitude of the pressure gradient at the boundary increases due to enhanced buoyancy forces in this region of the water column. This in turn requires a magnification of the boundary shear stress (τ) in order to satisfy the momentum balance. Further analysis reveals that the increase in τ corresponds to a decrease in shear length (δ'), the distance over which the free-stream velocity drops to zero at the bed.

3.2 Analytical formulation

The complete velocity field in the lake $\mathbf{q}(\mathbf{x}, t)$ (where $\mathbf{x} = \{x_i\}$, $i = 1, 2, 3$) can be decomposed into a flow $\mathbf{U}(\mathbf{x}, t)$ in the viscous benthic boundary layer and a flow $\mathbf{u}(\mathbf{x}, t)$ throughout the rest of the water column:

$$\mathbf{q} = \mathbf{u} + \mathbf{U} \ . \tag{3.1}$$

Neglecting nonlinear terms, which is valid for small wave amplitudes, the momentum equations are thus

$$\rho \frac{\partial q_j}{\partial t} = -\frac{\partial P}{\partial x_j} - g_j \rho + \frac{\partial \tau_{jk}}{\partial x_k} \ , \tag{3.2}$$

written in tensor notation. The (incompressible) continuity relations are

$$\boldsymbol{\nabla} \cdot \mathbf{q} = 0 \qquad \frac{\partial \rho}{\partial t} + \mathbf{q} \cdot \boldsymbol{\nabla} \rho = 0 \ .$$

For small amplitude waves, the velocities $\mathbf{u} = (u, v, w)$, pressure P, and density ρ can be decomposed into mean and dynamic fields,

$$\begin{aligned} \mathbf{u}(\mathbf{x}, t) &\rightarrow \mathbf{u}'(\mathbf{x}, t) & P(\mathbf{x}, t) &\rightarrow \overline{P}(z) + P'(\mathbf{x}, t) \\ \mathbf{U}(\mathbf{x}, t) &\rightarrow \mathbf{U}'(\mathbf{x}, t) & \rho(\mathbf{x}, t) &\rightarrow \overline{\rho}(z) + \rho'(\mathbf{x}, t) \ , \end{aligned} \tag{3.3}$$

where the perturbations correspond to the seiche motion. Since we are interested in periodic solutions, we assume the temporal variation of the fields $f = (\mathbf{u}', \mathbf{U}', \rho', P')$ is sinusoidal,

$$f(\mathbf{x}, t) \rightarrow \mathrm{Re}\left[f(\mathbf{x}) \, \mathrm{e}^{\mathrm{i}\omega t} \right] \ , \tag{3.4}$$

with ω the internal seiche frequency.

From (3.3) and (3.4), the linearised density-continuity relation can be written as

$$\mathrm{i}\omega \rho' + \frac{\mathrm{d}\overline{\rho}}{\mathrm{d}z} \left(w' + W' \right) = 0 \ . \tag{3.5}$$

In the momentum equations, the mean pressure and density are found to satisfy the hydrostatic relation $\mathrm{d}\overline{P}/\mathrm{d}z = -g\overline{\rho}$, and therefore cancel each other. (Hereinafter we drop the primes on the perturbation fields for convenience.) Dimensional analyses reveal that shear stresses throughout the water column scale on ν, while stresses near solid boundaries are $\sim \nu^{\frac{1}{2}}$ (see, for example, Ursell 1952). In addition, recent field observations by Gloor *et al.* (2000) support the assumption that the dissipation of seiche energy occurs at leading order within the benthic boundary-layer. We therefore neglect viscosity in the water column, and consider the τ_{jk} near

the bed alone. Because of the partitioning of the flows we are free to separate (3.2) into two sets of equations (after using (3.5) to eliminate the density),

$$\mathrm{i}\omega\overline{\rho}\mathbf{u} = -\boldsymbol{\nabla}P + \mathbf{g}\frac{1}{\mathrm{i}\omega}\frac{\mathrm{d}\overline{\rho}}{\mathrm{d}z}w \ , \qquad i\omega\overline{\rho}U_j = -g\frac{1}{\mathrm{i}\omega}\frac{\mathrm{d}\overline{\rho}}{\mathrm{d}z}W\delta_{j3} + \frac{\partial\tau_{jk}}{\partial x_k} \ , \tag{3.6}$$

representing the outer inviscid and boundary-layer flows, respectively. Continuity is simply

$$\boldsymbol{\nabla}\cdot\mathbf{u} = 0 \qquad \boldsymbol{\nabla}\cdot\mathbf{U} = 0 \ . \tag{3.7}$$

These two systems are coupled by the boundary/matching condition for the boundary-layer and outer flows,

$$\mathbf{u} + \mathbf{U} = \mathbf{0} \qquad \text{on } \partial \ , \tag{3.8}$$

where ∂ denotes boundary of the lake, i.e., the bed plus free surface $z = 0$; the surface makes zero contribution to seiche damping at lowest order, i.e. $\mathbf{U}_{surf} = \mathbf{0}$, but it is still convenient to describe the entire boundary as ∂ in the rest of this analysis. The partitioning in (3.6) is effectively analogous to the conventional treatment of oscillating (thin) boundary-layer flows, in which the pressure gradients inside and outside the boundary-layer are equal, and can be cancelled to yield a boundary-layer equation such as the **U**-equation in (3.6). In the present formulation the same result is achieved by associating the dynamic variations in P exclusively with the outer flow **u** (first equation in (3.6)).

We next derive the governing equation for the outer flow, followed by a boundary-layer analysis which provides the boundary conditions on **u** necessary to compute the viscous damping coefficient for the seiches.

3.2.1 Outer flow

Outside the boundary layer, a linearised governing equation for internal waves in 3D can be derived from the momentum equations (3.6) and continuity (3.7). The pressure and velocities

are related by the modified momentum equations (3.6), which we rewrite as

$$i\omega\frac{1}{\overline{\rho}}\nabla P = \omega^2\mathbf{u} - N^2 w\mathbf{k} \ , \tag{3.9}$$

where $\mathbf{k}$ is a unit vector in the z-direction, and $N^2(z) = -g/\overline{\rho}\cdot \mathrm{d}\overline{\rho}/\mathrm{d}z$ is the buoyancy frequency. For linear internal waves in 3D the problem is usually formulated in terms of the dynamic pressure, because P is the only field which can be isolated in a complete governing equation plus boundary condition system. Using (3.9) to replace the velocities in the $\mathbf{u}$-continuity relation (3.7) gives the governing equation

$$\nabla_h^2 P - \omega^2\overline{\rho}\frac{\partial}{\partial z}\left(\frac{1}{\overline{\rho}}\frac{1}{N^2-\omega^2}\frac{\partial P}{\partial z}\right) = 0 \ , \tag{3.10}$$

where $\nabla_h^2 \equiv \partial^2/\partial x^2 + \partial^2/\partial y^2$. The boundary conditions are derived from the no-flux requirement on the velocities, again using (3.9);

$$\mathbf{n}\cdot\mathbf{u} = 0 \quad \rightarrow \quad n_x\frac{\partial P}{\partial x} + n_y\frac{\partial P}{\partial y} - n_z\frac{\omega^2}{N^2-\omega^2}\frac{\partial P}{\partial z} \equiv \Gamma P = 0 \tag{3.11}$$

with $\mathbf{n} = (n_x, n_y, n_z)$ the boundary unit normal vector. Finally, for the boundary-layer analysis in the following section we note the following dimensional scalings for the outer flow. The horizontal and vertical coordinates are on the order of the length (or width) and depth of the lake, respectively, while the velocities follow conventional continuity scaling;

$$x, y \sim L \qquad z \sim H \qquad \frac{w}{u}, \frac{w}{v} \sim \mu \ , \qquad \mu \equiv \frac{H}{L} \ . \tag{3.12}$$

The mean density $\overline{\rho}$ is order $\rho_0 \sim 1000\mathrm{kg/m}^3$.

3.2.2 The boundaries

For convenience in describing both the boundary layer (i.e. $\mathbf{U}$) and the boundary conditions on $\mathbf{u}$, we define unit vectors $\mathbf{t}_1$, $\mathbf{t}_2$ which form a basis in the tangent plane at each point on ∂ (and are thus normal to $\mathbf{n}$, $\mathbf{n}\cdot\mathbf{t}_1 = \mathbf{n}\cdot\mathbf{t}_2 = 0$; $\mathbf{t}_1\cdot\mathbf{t}_2 = 0$; see figure 3-1). The vectors $(\mathbf{t}_1, \mathbf{t}_2, \mathbf{n})$

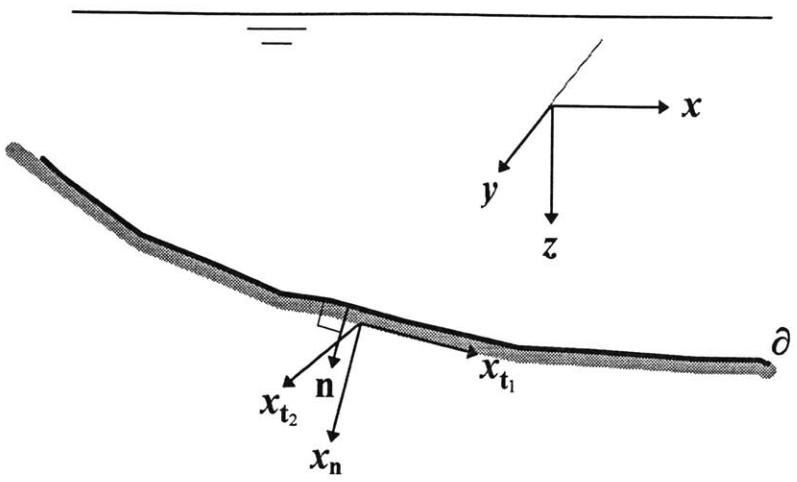

Figure 3-1: Definition sketch showing the absolute coordinates (x, y, z) and the boundary-fixed coordinates (x_{t_1}, x_{t_2}, x_n). Both systems are defined with the same relative orientation.

have the same relative orientation as $(\mathbf{i}, \mathbf{j}, \mathbf{k})$:

$$\mathbf{t}_1 \times \mathbf{t}_2 = \mathbf{n} \qquad \mathbf{t}_2 \times \mathbf{n} = \mathbf{t}_1 \qquad \mathbf{n} \times \mathbf{t}_1 = \mathbf{t}_2 \ ,$$

in analogy to the cyclic relations $\mathbf{i} \times \mathbf{j} = \mathbf{k}$, $\mathbf{j} \times \mathbf{k} = \mathbf{i}$, $\mathbf{k} \times \mathbf{i} = \mathbf{j}$. If we specify $\mathbf{x} = (x, y, z)$ as an absolute coordinate system (horizontal, vertical, with z positive down), we can then define

$$x_n \equiv \mathbf{n} \cdot \mathbf{x} \qquad x_{t_1} \equiv \mathbf{t}_1 \cdot \mathbf{x} \qquad x_{t_2} \equiv \mathbf{t}_2 \cdot \mathbf{x} \ ; \qquad \mathbf{x}_T = (x_{t_1}, x_{t_2}) \ .$$

Even though the orientation of these new coordinates is defined by the boundary (so that $(\mathbf{x}_T, x_n)$ are formally local coordinates which apply for the boundary-layer flow), we still treat $(\mathbf{x}_T, x_n)$ as an alternate, equivalent system to (x, y, z) in the outer flow analysis (i.e. for $\mathbf{u}$). Because the vertical-to-horizontal aspect ratio $\mu \ll 1$ for lakes, the two systems have essentially the same scales, $(\mathbf{x}_T, x_n) \sim (L, H)$. Boundary layer coordinates related to $(\mathbf{x}_T, x_n)$ will also be formally introduced below. Note that the boundary itself corresponds to $x_n = 0$, and we use

the equivalent notations

$$f|_{\partial} = f(\mathbf{x}_T, 0) \equiv f(\mathbf{s})$$

throughout this paper to describe functions on ∂.

3.2.3 Benthic boundary layer

The boundary conditions which complete the formulation for $\mathbf{u}$ are derived from the analysis of the boundary-layer flow. Viscous stresses dominate the momentum balance near the bed, so that this region can be regarded as distinct from the rest of the water column. The motion in the boundary-layer can be evaluated separately and then related to the outer flow as a modification to the conventional inviscid boundary conditions. We describe the stresses $\tau = \widehat{\tau}$ in the boundary-layer by

$$\widehat{\tau}_{jk} = \overline{\rho}\nu\left(\frac{\partial U_j}{\partial x_k} + \frac{\partial U_k}{\partial x_j}\right) \quad . \tag{3.13}$$

The viscosity ν is likely to have a spatial dependence, especially along the bed, due to variations in fluid velocity and to internal wave breaking at the bed within the pycnocline region (as discussed by Imberger 1998). We therefore consider both constant ν and $\nu(\mathbf{s})$ in the analytical formulation of the seiche decay rate. Across the boundary layer (i.e. in the normal direction) we assume that variation in $\overline{\rho}\nu$ (and in the outer inviscid flow $\mathbf{u_0}$) is very small. In practice, very little is currently known about turbulence or mixing parameters in lake benthic boundary layers, and so ultimately we take ν constant for the model systems investigated in this paper. However, it is still useful to carry the spatial dependence through the analysis in order to observe the potential impact of variations in viscosity and boundary-layer thickness on the decay.

Replacing $\partial/\partial t$ with $\mathrm{i}\omega$ in the boundary-layer equation in (3.6) and substituting the $\widehat{\tau}_{jk}$ (3.13) gives

$$\mathrm{i}\omega U_j = -\mathrm{i}\omega\frac{1}{\overline{\rho}}\frac{g}{\omega^2}\frac{\mathrm{d}\overline{\rho}}{\mathrm{d}z}W\delta_{j3} + \frac{1}{\overline{\rho}}\frac{\partial}{\partial x_k}\left[\overline{\rho}\nu\left(\frac{\partial U_j}{\partial x_k} + \frac{\partial U_k}{\partial x_j}\right)\right] \quad , \tag{3.14}$$

where $j = 1, 2, 3$, corresponding to x, y, z. The spatial variation of ν in the boundary-layer can

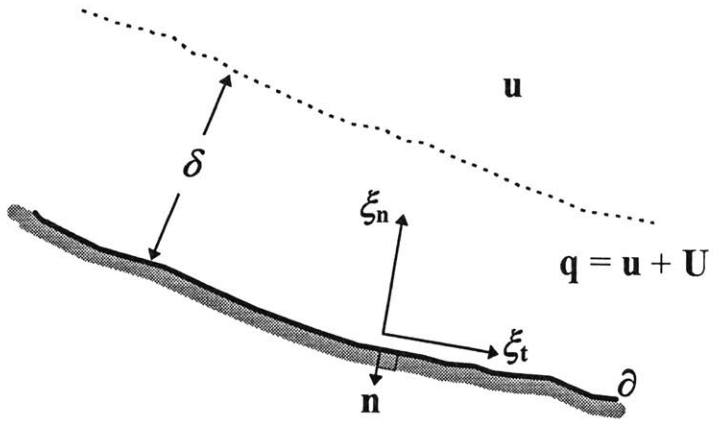

Figure 3-2: Definition sketch showing the boundary layer δ and the BL coordinates $(\boldsymbol{\xi}_\mathbf{t}, \xi_n) = (L^{-1}\mathbf{x_t}, -\delta^{-1}x_n)$ (the coordinate ξ_t denotes the pair (ξ_{t_1}, ξ_{t_2}) in the tangent plane to ∂).

be described by

$$\nu \rightarrow \nu\sigma^2(\mathbf{s}) \ , \qquad \max(\sigma^2) = 1 \ .$$

Specific details concerning the form of σ^2 will be discussed later. Within the boundary-layer we define the scaled coordinates $(\boldsymbol{\xi}_T, \xi_n)$ (figure 3-2)

$$\mathbf{x}_T \equiv L\boldsymbol{\xi}_T \qquad x_n \equiv -\delta\xi_n \ ; \qquad \delta \equiv \left(\frac{2\nu}{\omega_0}\right)^{\frac{1}{2}} \ , \tag{3.15}$$

where δ is the boundary-layer thickness and ω_0 is a reference frequency; in the following analysis ω_0 corresponds to the inviscid seiche frequency. The spatial variation of ν can equivalently be incorporated into the definition of the boundary-layer thickness, $\delta \rightarrow \delta(\mathbf{s}) = (2\nu/\omega_0)^{\frac{1}{2}}\sigma(\mathbf{s})$. The horizontal scale L is once again the length of the lake (see 3.12). The minus sign in the definition of ξ_n accounts for the fact that the boundary-layer normal coordinate is positive into the fluid, while the unit vector $\mathbf{n}$ is positive outward by convention (see figure 3-2). Given the

relationship between the inner and outer flows (3.8), the boundary-layer velocities scale as

$$\mathbf{U}_T \sim (u, v) \ , \qquad U_n \sim w \ ; \qquad \frac{U_n}{|\mathbf{U}_T|} \sim \mu \ , \tag{3.16}$$

where $\mathbf{U}_T \equiv (\mathbf{t}_1 \cdot \mathbf{U}, \mathbf{t}_2 \cdot \mathbf{U})$. With these scalings and assumptions, (3.14) becomes

$$2\mathrm{i}\frac{\omega}{\omega_0}U_j = 2\mathrm{i}\frac{\omega}{\omega_0}\frac{N^2}{\omega^2}W\delta_{j3} + \sigma^2\widehat{\nabla}^2 U_j + \mathcal{O}\left(\frac{\delta^2}{H^2}\right) \ . \tag{3.17}$$

Although the coordinates and velocities in this equation are written in the absolute basis $(\mathbf{i}, \mathbf{j}, \mathbf{k})$, in the next section we use the fact that the Laplacian can be written in terms of the boundary basis;

$$\widehat{\nabla}^2 \equiv \frac{\partial^2}{\partial \xi_n^2} + \frac{\delta^2}{L^2}\widehat{\nabla}_T^2 \ , \qquad \widehat{\nabla}_T^2 \equiv \frac{\partial^2}{\partial \xi_{t_1}^2} + \frac{\partial^2}{\partial \xi_{t_2}^2} \ . \tag{3.18}$$

The Boussinesq-type terms from $\partial\widehat{\tau}_{jk}/\partial x_k$ in (3.14) are somewhat difficult to scale because the density gradients are not expressed in terms of the (x, y, z) co-ordinate system. Nonetheless, it is safe to say they are within an order of magnitude of $\triangle\rho/\rho_0 \cdot \delta^2/H^2$, where $\triangle\rho = \rho_{surface} - \rho_{bed} \lesssim 3\mathrm{kg/m}^3$ in thermally-stratified lakes, and are therefore exceedingly small relative to the leading-order terms.

Continuity in the boundary-layer can be written in terms of $(\mathbf{x}_T, x_n)$ as

$$\frac{\partial}{\partial x_n}(\mathbf{n} \cdot \mathbf{U}) + \frac{\partial}{\partial x_{t_1}}(\mathbf{t}_1 \cdot \mathbf{U}) + \frac{\partial}{\partial x_{t_2}}(\mathbf{t}_2 \cdot \mathbf{U}) = 0 \, . \tag{3.19}$$

Defining the small dimensionless parameter

$$\varepsilon = \frac{\delta}{H} = \left(\frac{2\nu}{\omega_0 H^2}\right)^{\frac{1}{2}} < 1 \, , \tag{3.20}$$

continuity (3.19) can be non-dimensionalised as

$$-\frac{\partial}{\partial \xi_n}(\mathbf{n} \cdot \mathbf{U}) + \varepsilon\widehat{\nabla}_T \cdot \mathbf{U}_T = 0 \ , \tag{3.21}$$

where $\widehat{\nabla}_T$ is defined as in (3.18). The boundary-layer system (3.17)/(3.21) forms the basis for

the following perturbation analysis.

3.3 Perturbation

We now perform a perturbation analysis to evaluate the rate of viscous decay of internal seiche amplitude. Using the small parameter ε defined in (3.20), begin by making the expansions for $f \equiv (\mathbf{u}, \mathbf{U}, P, \omega)$:

$$f \rightarrow f_0 + \varepsilon f_1 + ... \tag{3.22}$$

We first evaluate the modification of the boundary conditions on $\mathbf{u}$ due to the presence of the benthic boundary-layer. The perturbation of the governing equation (3.10) is considered in the next section during computation of the frequency modification ω_1.

3.3.1 Boundary conditions

The continuity equation for the boundary-layer (3.21) reveals that the normal gradient of the n-component of $\mathbf{U_0}$ is zero;

$$\frac{\partial}{\partial \xi_n}(\mathbf{n} \cdot \mathbf{U_0}) = 0 \qquad \rightarrow \qquad \mathbf{n} \cdot \mathbf{U_0} = 0 \ . \tag{3.23}$$

The integration constant is taken as zero because we require $\mathbf{U}(\xi_n \rightarrow \infty, \boldsymbol{\xi}_T) = \mathbf{0}$. The flow within the boundary-layer is therefore exactly parallel to the boundary at lowest order, $\mathbf{U_0} = \mathbf{T} \cdot \mathbf{U_0} = \mathbf{U}_{0T}$. The matching condition on $\mathbf{u}$,$\mathbf{U}$ shows that the same is true for $\mathbf{u_0}$;

$$\mathbf{n} \cdot \mathbf{u_0}(0, \mathbf{x}_T) = 0 \ , \qquad \text{or} \qquad \mathbf{u_0}(0, \mathbf{x}_T) = (\mathbf{t_1}, \mathbf{t_2}) \cdot \mathbf{u_0}|_\partial = \mathbf{u}_{0T}(0, \mathbf{x}_T) \ . \tag{3.24}$$

Note that this is simply the standard no-flux condition for an inviscid flow (eg., 3.11).

In order to write the zeroth-order boundary-layer momentum equations (3.17) solely in terms of the 2-component tangential velocity field $\mathbf{U}_{0T}$ we must rewrite W_0 (see Appendix to

this chapter),

$$\frac{\partial^2 \mathbf{U}_{0T}}{\partial \xi_n^2} = 2\mathrm{i}\sigma^{-2}\left(\mathbf{U}_{0T} - \frac{N^2}{\omega_0^2} W_0 \mathbf{T}\cdot\mathbf{k}\right) = 2\mathrm{i}\sigma^{-2}\left(\mathbf{U}_{0T} - \frac{N^2}{\omega_0^2}\left(\mathbf{U}_{0T}\cdot(\mathbf{T}\cdot\mathbf{k})\right)\mathbf{T}\cdot\mathbf{k}\right) \quad . \tag{3.25}$$

This equation is simply the conventional Stokes system for an oscillating flow over a flat plate, modofied with the addition of buoyancy terms on the right. Outside the pycnocline, where $N \approx 0$, (3.25) reduces to the Stokes system. Within the pycnocline, however, the leading-order momentum balance is between the stresses on the left and buoyancy. As we see in §3.3.2 and §3.7.1, this has implications for the structure of the decay rate and the structure of the boundary-layer.

The solution to (3.25) with $\mathbf{U}_0(\xi_n \to \infty) \to 0$ is (see Appendix)

$$\mathbf{U}_{0T}(\boldsymbol{\xi}_t, \xi_n) = -\left(\mathbf{R}\mathrm{e}^{-(1+\mathrm{i})\sigma^{-1}\xi_n} + \mathbf{R}'\mathrm{e}^{-(1+\phi\mathrm{i})\sigma^{-1}|\eta|\xi_n}\right)\mathbf{u}_{0T}(0, \mathbf{x}_T) \quad , \tag{3.26}$$

where

$$\eta^2 \equiv 1 - \frac{N^2}{\omega_0^2}\left(p_1^2 + p_2^2\right) \quad ,$$

$p_i(s) = \mathbf{t}_i(s)\cdot\mathbf{k}$ is the projection of $\mathbf{t}_i$ in the vertical, $\phi \equiv \mathrm{sign}\left(\eta^2\right)$, and the matrices $\mathbf{R}$ and $\mathbf{R}'$ are given by

$$\mathbf{R}(s) = \frac{1}{p_1^2 + p_2^2}\begin{pmatrix} p_2^2 & -p_1 p_2 \\ -p_1 p_2 & p_1^2 \end{pmatrix} \qquad \mathbf{R}'(s) = \frac{1}{p_1^2 + p_2^2}\begin{pmatrix} p_1^2 & p_1 p_2 \\ p_1 p_2 & p_2^2 \end{pmatrix} \quad .$$

We define the 2-component $\mathbf{U}_{0T}$ and $\mathbf{u}_{0T}(0, \mathbf{x}_T)$ as column vectors. (In principal we can always choose a $\mathbf{T}$-basis such that, for example, $\mathbf{t}_1 \cdot \mathbf{k} = 0$ over the entire lake bed surface. However for some simple basins, for example with spherical or elliptical geometries, it is often more convenient to select a conventional basis, for which $\mathbf{t}_{1,2}\cdot\mathbf{k} \neq 0$ in general.) The zeroth-order flow for the entire system can thus be written as

$$\mathbf{q}_0 = \mathbf{u}_0 - \left(\mathbf{R}\mathrm{e}^{-(1+\mathrm{i})\sigma^{-1}\xi_n} + \mathbf{R}'\mathrm{e}^{-(1+\phi\mathrm{i})\sigma^{-1}|\eta|\xi_n}\right)\mathbf{u}_0|_\partial \quad . \tag{3.27}$$

Some interesting and important properties of this solution are discussed in §3.8.

As stated earlier, it is not necessary to determine the governing equation and solution for $\mathbf{U}_1$ in order to evaluate the modification to the seiche frequency ω_1. However we do need to consider the $\mathcal{O}(\varepsilon)$ continuity relation, since it allows us to manipulate the boundary condition for $\mathbf{u}$ later in the analysis. From (3.21), first-order continuity in the boundary-layer gives

$$-\frac{\partial}{\partial \xi_n}(\mathbf{n}\cdot\mathbf{U}_1)+\boldsymbol{\nabla}_T\cdot\mathbf{U}_{0T}=0 \quad \rightarrow \quad \mathbf{n}\cdot\mathbf{U}_1|_\partial=\left[\int \boldsymbol{\nabla}_T\cdot\mathbf{U}_{0T}\mathrm{d}\xi_n'\right]_\partial .$$

Substituting the solution for $\mathbf{U_0}$ (3.26) into this integral, and using the matching conditions $\mathbf{n}\cdot\mathbf{u}_1|_\partial=-\mathbf{n}\cdot\mathbf{U}_1|_\partial$ and $\mathbf{u}_{1T}|_\partial=-\mathbf{U}_{1T}|_\partial$, (3.8) then gives

$$\begin{aligned}\mathbf{n}\cdot\mathbf{u}_1|_\partial &= \boldsymbol{\nabla}_T\cdot\left(\left(\mathbf{R}\left[\int \mathrm{e}^{-(1+\mathrm{i})\sigma^{-1}\xi_n'}\mathrm{d}\xi_n'\right]_\partial+\mathbf{R}'\left[\int \mathrm{e}^{-(1+\phi\mathrm{i})\sigma^{-1}|\eta|\xi_n'}\mathrm{d}\xi_n'\right]_\partial\right)\mathbf{u}_{0T}|_\partial\right)\\ &= -\frac{1}{2}\boldsymbol{\nabla}_T\cdot\left(\sigma\left((1-\mathrm{i})\,\mathbf{R}+(1-\mathrm{i}\phi)\,\frac{1}{|\eta|}\mathbf{R}'\right)\mathbf{u}_{0T}(0,\mathbf{x}_T)\right) , \end{aligned} \tag{3.28}$$

using the fact that $\phi^2=1$. Here we write the inviscid flow on ∂ as $\mathbf{u}_{0T}(0,\mathbf{x}_T)$ to make it clear that $\boldsymbol{\nabla}_T$ is operating on $\mathbf{u}_{0T}|_\partial$. This somewhat complicated procedure has ultimately allowed us to write the boundary condition for $\mathbf{u}_1$ solely in terms of $\mathbf{u_0}$.

Finally, for the free surface condition we use the rigid lid approximation,

$$w(x,y,0)=0 ,$$

which yields a simple homogeneous condition for the $\mathbf{n}\cdot\mathbf{u}_i|_\partial$ at every order i in ε.

3.3.2 Governing equation and frequency change

Placing the expansions (3.22) for P and ω into the P-equation (3.10), we obtain the zeroth- and first-order governing equations (see Dore, 1969)

$$\mathcal{L}P_0=0 , \qquad \mathcal{L}P_1=2\omega_0\omega_1\frac{\partial}{\partial z}\left(\frac{1}{\overline{\rho}}\frac{N^2}{\left(N^2-\omega_0^2\right)^2}\frac{\partial P_0}{\partial z}\right) , \tag{3.29}$$

where $\mathcal{L}$ is the linear operator

$$\mathcal{L}(*) = \overline{\rho}^{-1}\nabla_h^2(*) - \frac{\partial}{\partial z}\left(\frac{1}{\overline{\rho}}\frac{\omega_0^2}{N^2-\omega_0^2}\frac{\partial}{\partial z}(*)\right) \ .$$

Therefore, once the boundary conditions at each order are known, the frequency change ω_1 can be evaluated from the solvability condition on the P_0/P_1 system.

To determine the boundary conditions for P_0 and P_1, note that the boundary-layer perturbation to the system appears as a modification of the velocity field at $\mathcal{O}(\varepsilon)$ (see 3.28). The required conditions on P can thus be obtained by replacing $\mathbf{u}$ with P in (3.24) and (3.28). To do this, first expand P, ω, and $\mathbf{u}$ (3.22) in the momentum equations (3.9) to find expressions relating P and $\mathbf{u}$ at both orders:

$$\begin{aligned} \mathrm{i}\omega_0\boldsymbol{\nabla}P_0 &= \overline{\rho}\left(\omega_0^2\mathbf{u}_0 - N^2 w_0\mathbf{k}\right) \\ \mathrm{i}\omega_0\boldsymbol{\nabla}P_1 &= \overline{\rho}\left(\omega_0^2\mathbf{u}_1 - N^2 w_1\mathbf{k}\right) + \frac{\omega_1}{\omega_0}\overline{\rho}\left(\omega_0^2\mathbf{u}_0 + N^2 w_0\mathbf{k}\right) \ . \end{aligned} \tag{3.30}$$

Using these, the boundary conditions on P are

$$\begin{aligned} \Gamma_0 P_0 &= 0 \qquad \text{on } \partial \\ \Gamma_0 P_1 &= 2\omega_0\omega_1\overline{\rho}\gamma_0\mathbf{n}\cdot\boldsymbol{\nabla}P_0 \\ &\quad -\frac{1}{2}\mathrm{i}\omega_0\overline{\rho}\boldsymbol{\nabla}_T\cdot\left(\sigma\left((1-\mathrm{i})\,\mathbf{R} + (1-\mathrm{i}\phi)\,\frac{1}{|\eta|}\mathbf{R}'\right)\mathbf{u}_{0T}(0,\mathbf{x}_T)\right) \ , \end{aligned} \tag{3.31}$$

with Γ_0 as defined in (3.11) (with $\omega \to \omega_0$). The last term in the $\mathcal{O}(\varepsilon)$ expression, which is the inhomogeneous term introduced by the boundary-layer perturbation, has been left in its original form (i.e. in terms of $\mathbf{u}_0$). The conditions (3.31) complete the information required to determine ω_1.

Although we can proceed with the solvability analysis using equations (3.29) and (3.31) as written, it is possible to use a shorthand technique which exploits the connection between the P- and $\mathbf{u}$-representations of the various equations. Specifically, it can easily be verified that the P_0- and P_1-equations (3.29) can also be derived by substituting (3.30) into the respective

continuity equations

$$\nabla \cdot \mathbf{u}_0 = 0 \qquad \nabla \cdot \mathbf{u}_1 = 0 \ .$$

Thus, both the governing equations and boundary conditions for the P-system can be derived from their $\mathbf{u}$ counterparts by replacing $\mathbf{u}$ with P at each order. The P_0/P_1 solvability condition

$$\int_\Omega (P_0^* \mathcal{L} P_1 - P_1 \mathcal{L} P_0^*)\, \mathrm{d}V = 2\omega_0\omega_1 \int_\Omega P_0^* \frac{\partial}{\partial z}\left(\frac{1}{\overline{\rho}} \frac{N^2}{\left(N^2-\omega_0^2\right)^2} \frac{\partial P_0}{\partial z}\right) \mathrm{d}V$$

(where $\mathrm{d}V \equiv \mathrm{d}x\mathrm{d}y\mathrm{d}z$ and Ω is the lake volume, and $(\,)^*$ denotes complex conjugate) can therefore be written much more succinctly as

$$\int_\Omega (P_0^* \nabla \cdot \mathbf{u}_1 + P_1 \nabla \cdot \mathbf{u}_0^*)\, \mathrm{d}V = 0 \ .$$

From this relation it immediately follows (after rearranging and using Gauss' theorem) that

$$\int_\Omega (\mathbf{u}_1 \cdot \nabla P_0^* + \mathbf{u}_0^* \cdot \nabla P_1)\, dV = \int_\partial \mathbf{n} \cdot (P_0^* \mathbf{u}_1 + P_1 \mathbf{u}_0^*)\, ds \ , \tag{3.32}$$

where $\mathrm{d}s \equiv \mathrm{d}x_{\mathbf{t}_1}\mathrm{d}x_{\mathbf{t}_2}$ is the surface element on the boundary. The free surface makes no contribution to the surface integral because $P = w = 0$. At this point we can choose to eliminate either $\mathbf{u}$ or P in favor of the other, using (3.30). Given that the $\mathcal{O}(\varepsilon)$ boundary conditions are expressed in terms of the velocities, it is simpler to eliminate P. Using (3.30) in the left-hand side of (3.32) and (3.24) and (3.28) on the right-hand side, after cancellations we find

$$\begin{aligned} &\frac{\omega_1}{\omega_0} \frac{1}{\mathrm{i}\omega_0} \int_\Omega \overline{\rho} \left(\omega_0^2 |\mathbf{u}_0|^2 + N^2 |w_0|^2\right) \mathrm{d}V \\ &\qquad = -\frac{1}{2} \int_\partial P_0^* \left(\nabla_T \cdot \left(\sigma \left[(1-\mathrm{i})\,\mathbf{R} + \frac{1-\mathrm{i}\phi}{|\eta|}\mathbf{R}'\right] \mathbf{u}_{0T}\,(0, \mathbf{x}_T)\right)\right) \mathrm{d}s \ . \end{aligned} \tag{3.33}$$

Now, integrating the right-hand-side of this equation by parts gives

$$\begin{aligned}
&\int_{\partial} P_0^* \boldsymbol{\nabla}_T \cdot \left(\sigma \left[(1-\mathrm{i})\,\mathbf{R} + \frac{1-\mathrm{i}\phi}{|\eta|}\mathbf{R}' \right] \mathbf{u}_{0T}\,(0,\mathbf{x}_T) \right) \mathrm{d}s \\
&\quad = \int_{\partial} \boldsymbol{\nabla}_T \cdot \left(\sigma \left[(1-\mathrm{i})\,\mathbf{R} + \frac{1-\mathrm{i}\phi}{|\eta|}\mathbf{R}' \right] P_0^* \mathbf{u}_{0T}\,(0,\mathbf{x}_T) \right) \mathrm{d}s \\
&\qquad - \int_{\partial} \left(\sigma \left[(1-\mathrm{i})\,\mathbf{R} + \frac{1-\mathrm{i}\phi}{|\eta|}\mathbf{R}' \right] \mathbf{u}_{0T}\,(0,\mathbf{x}_T) \right) \cdot \boldsymbol{\nabla}_T P_0^* \mathrm{d}s \ .
\end{aligned}$$

The first integral on the right can be partially integrated up to the free surface, where it vanishes because $P_{0surface} = 0$. This leaves

$$\begin{aligned}
&\frac{\omega_1}{\omega_0} \int_{\Omega} \overline{\rho} \left(\omega_0^2 |\mathbf{u}_0|^2 + N^2 |w_0|^2 \right) \mathrm{d}V \\
&\quad = \frac{1}{2} \int_{\partial} \left(\sigma \left[(1-\mathrm{i})\,\mathbf{R} + \frac{1-\mathrm{i}\phi}{|\eta|}\mathbf{R}' \right] \mathbf{u}_{0T}\,(0,\mathbf{x}_T) \right) \cdot \boldsymbol{\nabla}_T \left(i\omega_0 P_0^* \right) \mathrm{d}s \ .
\end{aligned}$$

Finally, replacing P_0 with $\mathbf{u}_0$ in this relation (using 3.30) gives

$$\begin{aligned}
&\frac{\omega_1}{\omega_0} \int_{\Omega} \overline{\rho} \left(\omega_0^2 |\mathbf{u}_0|^2 + N^2 |w_0|^2 \right) \mathrm{d}V \\
&\quad = -\frac{1}{2} \int_{\partial} \left(\overline{\rho}\sigma \left[(1-\mathrm{i})\,\mathbf{R} + \frac{1-\mathrm{i}\phi}{|\eta|}\mathbf{R}' \right] \mathbf{u}_{0T}\,(0,\mathbf{x}_T) \right) \cdot \left(\omega_0^2 \mathbf{u}_{0T} - N^2 w_0 \mathbf{T}\cdot\mathbf{k} \right) \mathrm{d}s \ .
\end{aligned}$$

Dividing by ω_0^2 and redimensionalising gives

$$\frac{\varepsilon\omega_1}{\omega_0} \cdot 4E = -\frac{1}{2}\delta \int_{\partial} \left(\overline{\rho}\sigma \left((1-\mathrm{i})\,\mathbf{R} + \frac{1-\mathrm{i}\phi}{|\eta|}\mathbf{R}' \right) \mathbf{u}_{0T}\,(0,\mathbf{x}_T) \right) \cdot \left(\mathbf{u}_{0T} - \frac{N^2}{\omega_0^2} w_0 \mathbf{T}\cdot\mathbf{k} \right) \mathrm{d}s \ , \tag{3.34}$$

recalling the definition of ε (3.20). Due to equipartition (linear waves), the zeroth-order system energy

$$E \equiv \int_{\Omega} \frac{1}{2}\overline{\rho} |\mathbf{u}_0|^2 \mathrm{d}V \qquad \left(= \int_{\Omega} \frac{1}{2}\overline{\rho}\frac{N^2}{\omega_0^2} w_0^2 \mathrm{d}V \right) \tag{3.35}$$

represents the magnitude of both the total system kinetic (first integral) and potential (in

brackets) energies, as well as the total (constant) energy of the seiche in the inviscid formulation;

$$\begin{aligned} E_{kin}(t) &= E\cos^2(\omega_0 t+\phi) \\ E_{pot}(t) &= E\sin^2(\omega_0 t+\phi) \end{aligned} \quad ; \qquad E_{total} = E_{kin}+E_{pot} = E \ , \tag{3.36}$$

with ϕ an arbitrary phase. Once again we can replace w_0 with $\mathbf{u}_{0T}$ in (3.34) using

$$\mathbf{u}_{0T}|_\partial - \frac{N^2}{\omega_0^2}\, w_0|_\partial\, \mathbf{T}\cdot\mathbf{k} \;=\; \mathbf{u}_{0T}|_\partial - \frac{N^2}{\omega_0^2}\left(\mathbf{u}_{0T}|_\partial\cdot(\mathbf{T}\cdot\mathbf{k})\right)\mathbf{T}\cdot\mathbf{k} \;=\; \mathbf{M}\,\mathbf{u}_{0T}|_\partial \ ,$$

where

$$\mathbf{M} \equiv \begin{pmatrix} 1-\frac{N^2}{\omega_0^2}p_1^2 & -\frac{N^2}{\omega_0^2}p_1p_2 \\ -\frac{N^2}{\omega_0^2}p_1p_2 & 1-\frac{N^2}{\omega_0^2}p_2^2 \end{pmatrix} = \mathbf{I} - \frac{N^2}{\omega_0^2}\left(p_1^2+p_2^2\right)\mathbf{R}'$$

(see Appendix). The desired decay rate is then computed from (3.34) as $\alpha \equiv \mathrm{Im}(\varepsilon\omega_1)$, defined so that α is positive:

$$\frac{\alpha}{\omega_0}\cdot 4E = \int_\partial \delta(\mathbf{s})\,\frac{1}{2}\overline{\rho}\mathbf{u}_{0bed}^{\mathrm{T}}\left[\mathbf{R}+|\eta|\,\mathbf{R}'\right]\mathbf{u}_{0bed}\mathrm{d}s \ . \tag{3.37}$$

This result is expressed in matrix notation, with $\mathbf{u}_{0T}|_\partial = \mathbf{u}_{0bed}$ a column vector (T denotes transpose), using the fact that $\mathbf{R}^{\mathrm{T}} = \mathbf{R}$, $\mathbf{R}'^{\mathrm{T}} = \mathbf{R}'$, as well as the relations (end of Appendix)

$$\mathbf{R}\mathbf{M} = \mathbf{R} \ , \qquad \mathbf{R}'\mathbf{M} = \eta^2\mathbf{R}' \ ,$$

plus $\eta^2 = |\eta|^2\phi$ and $\phi^2 = 1$. The boundary-layer thickness $\delta(\mathbf{s}) = (2\nu/\omega_0)^{\frac{1}{2}}\sigma(\mathbf{s})$ appears as a weight factor, clearly illustrating the potential importance of spatial variations in ν. The matrices $\mathbf{R}$ and $\mathbf{R}'$, whose elements are given by the relative orientation of the boundary tangent plane and the vertical (i.e. $(\mathbf{t}_1,\mathbf{t}_2)$ versus $\mathbf{k}$), are functions of the bathymetry of the basin.

Note that the boundary-layer contribution to surface seiche damping is found from (3.37) by setting $\overline{\rho}$ = constant. Then, with $N^2 = 0$, $|\eta| = 1$, and $\mathbf{R}+\mathbf{R}' = \mathbf{I}$, we have

$$\frac{\alpha}{\omega_0}\cdot 4E = \int_\partial \delta(\mathbf{s})\,\frac{1}{2}\overline{\rho}|\mathbf{u}_{0bed}|^2\,\mathrm{d}s = \int_\partial \delta(\mathbf{s})\,E_{kin}\mathrm{d}s \ . \tag{3.38}$$

This is identical to the result obtained by Henderson and Miles (1994), and to the boundary-layer portion of the damping rate computed by Mei and Liu (1973; see also Mei 1989). (Although the Mei and Liu decay rate is expressed in terms of both the inviscid and first-order boundary-layer velocities, it is easily verified that their result can be rewritten as in (3.38). Also note that the free surface contribution, which is non-negligible for surface waves and seiches, can also be determined in (3.37) and (3.38) if the rigid lid approximation is avoided from the outset.) The decay rate for internal seiches (3.37) is therefore effectively equal to the kinetic energy at the bed (normalised by the total seiche energy), weighted by a buoyancy factor. In fact, the assumption of linear energy decay $dE/dt \propto E$ or E_{BL} is often used as a starting point for estimating seiche damping rates (see e.g. Fischer *et al.*, 1979, page 186). Equation (3.37) shows that it is necessary to include buoyancy and bathymetry effects in order to compute α for internal seiches. Note that (3.37) is a generic result which is generalizable to any form of basin-scale wave motion (i.e. two-dimensional, three-dimensional, rotational, surface and internal). The only information required to compute α for a given system is a solution for the inviscid flow field $\mathbf{u_0}$.

3.4 Physical interpretation

In the above analysis the decay coefficient α was derived from the mathematical condition of solvability on the $\mathcal{O}(\varepsilon^0)/\mathcal{O}(\varepsilon^1)$ system. There are several other ways to derive the expression for α in (3.37) based on energy arguments; these alternate perspectives prove useful in making the connection between the computed decay rate and the underlying physics.

3.4.1 Bed stresses

Henderson and Miles (1994, §3) showed that the damping rate for surface waves can be computed from the (period-averaged) stress working on the boundary,

$$\frac{\alpha}{\omega_0} = \frac{1}{4\omega_0 E} \mathrm{Re}\left[\int_\partial u_{0j}^* \tau_{0nj} \mathrm{d}s\right] \quad . \tag{3.39}$$

In this expression the normal stresses at the bed $\tau_{0nj} = n_i \tau_{0ij}$ are evaluated using the modified (inviscid plus boundary-layer) flow field q_{0j}. Equation (3.39) can be applied to internal seiches

by simply substituting the solution for $\mathbf{q}_0$ given in (3.27). We thus compute the shear (in dimensional form)

$$\frac{\partial \mathbf{q}_0}{\partial x_i} \simeq \frac{\partial \mathbf{q}_0}{\partial x_n} = \frac{\partial \mathbf{u}_0}{\partial x_n} + \frac{1}{\delta}\left((1+\mathrm{i})\,\mathbf{R}\mathrm{e}^{-(1+\mathrm{i})\frac{x_n}{\delta}} + (1+\phi\mathrm{i})\,|\eta|\,\mathbf{R}'\mathrm{e}^{-(1+\phi\mathrm{i})|\eta|\frac{x_n}{\delta}}\right)\mathbf{u}_0|_\partial \ , \tag{3.40}$$

recognizing that the leading-order terms correspond to the normal derivatives. Using (3.40), the bed stresses are then

$$\boldsymbol{\tau}_{0n}|_\partial = \overline{\rho}\nu\sigma^2\frac{\partial \mathbf{q}_0}{\partial x_n}\bigg|_\partial = \left((1+\mathrm{i})\,\mathbf{R} + (1+\phi\mathrm{i})\,|\eta|\,\mathbf{R}'\right)\frac{\overline{\rho}\nu\sigma^2}{\delta}\mathbf{u}_0\bigg|_\partial \ . \tag{3.41}$$

Placing both (3.40) and (3.41) into (3.39) immediately gives

$$\frac{\alpha}{\omega_0} = \frac{1}{4E}\int_\partial \delta(\mathbf{s})\,\frac{\overline{\rho}}{2}\mathbf{u}_{0bed}^{\mathrm{T}}\left(\mathbf{R} + |\eta|\,\mathbf{R}'\right)\mathbf{u}_{0bed}\mathrm{d}s \ , \tag{3.42}$$

using the definition of the boundary-layer thickness $\delta^2(\mathbf{s}) = 2\nu/\omega_0 \cdot \sigma^2(\mathbf{s})$ and the fact that $\mathbf{u}_0^* = \mathbf{u}_0$. This is the same result as (3.37), revealing that the decay rate for internal seiches can be viewed as the stress working by the seiche on the solid boundary, just as in the surface wave case.

3.4.2 Dissipation within the boundary-layer

Consider the general linearised governing equation (see 3.2)

$$\overline{\rho}\frac{\partial \widehat{q}_j}{\partial t} = -\frac{\partial \widehat{P}}{\partial x_j} - g_j\widehat{\rho} + \frac{\partial \widehat{\tau}_{jk}}{\partial x_k} \ ,$$

where $\widehat{f}(\mathbf{x},t) = \mathrm{Re}\left[f(\mathbf{x})\,\mathrm{e}^{\mathrm{i}\omega t}\right]$ for wave motion. The $\widehat{\tau}_{jk}$ represent viscous stresses, written in terms of the $\widehat{q}_j$ in general ($\widehat{q}_j = \widehat{u}_j + \widehat{U}_j$, for example). Multiplying this equation by $\widehat{q}_j$ and integrating over an unspecified volume V (bounded by surface S) gives (see, for example, Acheson, page 216, and Landau and Lifshitz, page 50)

$$\frac{\mathrm{d}}{\mathrm{d}t}\int_V \frac{1}{2}\overline{\rho}\,|\widehat{\mathbf{q}}|^2\,\mathrm{d}V + \int_V \widehat{\rho}\mathbf{g}\cdot\widehat{\mathbf{q}}\mathrm{d}V = -\int_S \widehat{P}\widehat{\mathbf{q}}\cdot\mathrm{d}\mathbf{s} + \int_S n_i\widehat{q}_j\widehat{\tau}_{ij}\mathrm{d}s - \int_V \widehat{\tau}_{ij}\frac{\partial \widehat{q}_j}{\partial x_i}\mathrm{d}V \ . \tag{3.43}$$

This is a generalised equation for energy fluxes in a fluid flow. The left-hand side of (3.43) is the rate of change of kinetic plus potential energy (i.e. $g\widehat{\rho}_0\widehat{w}_0 = \partial/\partial t\left(\frac{1}{2}\overline{\rho}N^2/\omega_0^2\cdot\widehat{w}_0^2\right) = \widehat{E}_{pot}$, $E = \widehat{E}_{kin} + \widehat{E}_{pot}$), and therefore corresponds to the total energy ($E =$ constant) in the inviscid formulation.

For fluid in a basin, (3.43) reduces to

$$\frac{\mathrm{d}E}{\mathrm{d}t} = -\int_\Omega \widehat{\tau}_{ij}\frac{\partial\widehat{q}_j}{\partial x_i}\mathrm{d}V \ , \qquad E = \int_\Omega\left(\widehat{E}_{kin} + \widehat{E}_{pot}\right)\mathrm{d}V \ , \tag{3.44}$$

since the velocities vanish on the solid boundary, and $P = \tau = 0$ at the free surface. This relation simply states that the energy in the system (which has not yet been specified) decays through viscous dissipation. Applying (3.44) to seiches, dimensional analyses reveal that the dissipation term is of order $\nu_V\omega_0^{-1}H^{-2} \sim \varepsilon^2$ outside the boundary-layer (where ν_V is a vertical viscosity), while the boundary-layer contribution to the integral is $\mathcal{O}(\varepsilon)$. We can therefore partition the total lake volume into an inviscid core plus a boundary-layer, $\Omega = \Omega_c + V_{BL}$, and restrict attention solely to the boundary-layer. Retaining only the $\mathcal{O}(\varepsilon)$ terms, and period averaging, we write (3.44) as

$$-2\alpha E = -\frac{1}{2}\,\mathrm{Re}\left[\int_\Omega \tau_{ij}\frac{\partial q_j^*}{\partial x_i}\mathrm{d}V\right] \simeq -\frac{1}{2}\,\mathrm{Re}\left[\int_{V_{BL}} \boldsymbol{\tau}_{0n}\cdot\frac{\partial\mathbf{q}_0^*}{\partial x_n}\mathrm{d}s\mathrm{d}x_n\right] \ . \tag{3.45}$$

Here we have defined the energy decay rate as 2α (i.e., seiche amplitude decay rate $= \alpha$), and again used the fact that the leading-order stresses and shears are in the normal direction. Now using (3.40) we find

$$\boldsymbol{\tau}_{0n}|_{BL} = \overline{\rho}\nu\sigma^2\left.\frac{\partial\mathbf{q}_0}{\partial x_n}\right|_{BL} \approx \frac{\overline{\rho}\nu\sigma^2}{\delta}\left((1+\mathrm{i})\,\mathbf{R}\mathrm{e}^{-(1+\mathrm{i})\frac{x_n}{\delta}} + (1+\phi\mathrm{i})\,|\eta|\,\mathbf{R}'\mathrm{e}^{-(1+\phi\mathrm{i})|\eta|\frac{x_n}{\delta}}\right)\mathbf{u}_0|_\partial \ ,$$

using the fact that variations in $\overline{\rho}(z)$ and $\mathbf{u}_0$ across the boundary-layer are small (i.e. $\partial\mathbf{u}_0/\partial x_n|_{BL} \approx \mathbf{0}$). Substituting (3.40) and this expression for $\boldsymbol{\tau}_{0n}|_{BL}$ into (3.45) yields

$$\alpha\cdot 4E = \mathrm{Re}\left[\int_{V_{BL}}\frac{\overline{\rho}\nu\sigma^2}{\delta^2}\mathbf{u}_{0bed}^{\mathrm{T}}\left|(1+\mathrm{i})\,\mathbf{R}\mathrm{e}^{-(1+\mathrm{i})\frac{x_n}{\delta}} + (1+\phi\mathrm{i})\,|\eta|\,\mathbf{R}'\mathrm{e}^{-(1+\phi\mathrm{i})|\eta|\frac{x_n}{\delta}}\right|^2\mathbf{u}_{0bed}^*\mathrm{d}s\mathrm{d}x_n\right] \ ,$$

since $\mathbf{R} = \mathbf{R}^{\mathrm{T}}$, $\mathbf{R}' = \mathbf{R}'^{\mathrm{T}}$. Using the fact that $\mathbf{R}^2 = \mathbf{R}$, $\mathbf{R}'^2 = \mathbf{R}'$, $\mathbf{R}\mathbf{R}' = \mathbf{0}$, and $\eta^2 = |\eta|^2\,\phi$ (see Appendix), this again reduces to (3.37) after integrating over the boundary-layer (from $x_n = 0$

to ∞), and using the definition of $\delta(\mathbf{s})$. The seiche decay rate can therefore be interpreted as the rate of generation of turbulence energy in the benthic boundary-layer. This is an important result because it not only shows the impact of seiches on near-bed mixing, it specifically describes the energy transfer from the seiches to the benthic boundary-layer. As mentioned in §3.2, the observations of Gloor *et al.* (2000) confirm that this transfer is the leading-order energy flux for seiches.

3.4.3 Pressure working

Mei and Liu (1973) also related the decay rate for surface waves to the work done by the wave motion on the boundary-layer, through a meticulous accounting of energy fluxes among different regions of the fluid. Interestingly, because the decay rate (3.37) in the present paper was evaluated using a mixed analysis of $\mathbf{u}$ and P, the parallel between the solvability and energy flux approaches is more readily apparent here than for the velocity potential (ϕ) formulation used by Mei and Liu (1973). For surface waves, this equivalence is also clearer if the problem is formulated using the dynamic pressure (i.e. $P = -\mathrm{i}\omega\rho\phi$, with ρ constant).

Beginning with the energy equation (3.43)/(3.44), we once again make the distinction between the inviscid core and the boundary-layer, $\Omega = \Omega_c + V_{BL}$. The boundary between the core and the boundary-layer is denoted ∂_c, with $\partial - \partial_c \sim \delta$. Retaining only the $\mathcal{O}(\varepsilon)$ terms, we write (3.44) as

$$\frac{\mathrm{d}}{\mathrm{d}t}\int_{\Omega_c}\left(\widehat{E}_{kin}+\widehat{E}_{pot}\right)\mathrm{d}V = -\int_{\partial_c}\widehat{P}\widehat{\mathbf{u}}\cdot\mathbf{n}\mathrm{d}s \tag{3.46}$$

$$0 = \int_{\partial_c}\widehat{P}\widehat{\mathbf{u}}\cdot\mathbf{n}ds - \int_{V_{BL}}\widehat{\tau}_{ij}\frac{\partial\widehat{q}_j}{\partial x_i}dV\ . \tag{3.47}$$

From 3.46 we immediately see the equivalence between the energy flux approach and the previous solvability analysis (see e.g. 3.32 and 3.33). Equation 3.46 describes the pressure work done by the seiche on the boundary-layer, while 3.47 is the subsequent viscous dissipation within the boundary-layer of the energy provided by the seiche. Adding these two equations eliminates the pressure terms, which is consistent with the fact that the velocity field $\widehat{\mathbf{q}}$ vanishes on the solid boundary (see 3.43, for $V \to \Omega$, $S \to \partial_{lake}$), as well as the analysis in the previous section.

To proceed, using the fact that $\mathbf{n} \cdot \mathbf{u}_0 = 0$, we find

$$\int_{\partial_c} \widehat{P}\widehat{\mathbf{u}} \cdot \mathbf{n} \mathrm{d}s = \varepsilon \int_{\partial_c} \widehat{P}\widehat{\mathbf{u}}_1 \cdot \mathbf{n} \mathrm{d}s = -\frac{1}{2}\delta \int_{\partial_c} \widehat{P} \boldsymbol{\nabla}_T \cdot (\sigma \Lambda \widehat{\mathbf{u}}_{0T}) \, \mathrm{d}s \ , \tag{3.48}$$

where we have used the boundary condition for $\mathbf{u}_1$ (i.e.3.28, written in dimensional form, and with $\Lambda = (1 - \mathrm{i})\,\mathbf{R} + (1 - \mathrm{i}\phi)\,|\eta|^{-1}\,\mathbf{R}'$). Using 3.48, the decay rate α (computed from $\omega \to \omega' + \mathrm{i}\alpha$) is determined by period averaging 3.46 (see Mei and Liu, 1973, §3.5), and replacing $\Omega_c \to \Omega$ and $\partial_c \to \partial$ in the various integrals (which does not change the degree of accuracy of the result). The analysis then proceeds exactly as before (i.e. from 3.33 to 3.34). This analysis therefore returns the previous result (3.37), and reveals that the damping of the seiches can also be regarded as the pressure working done by the seiche on the boundary-layer. More specifically, according to Mei and Liu (1973), this result provides information about the energy transfer mechanism from the inviscid core to the boundary-layer.

Interestingly, one drawback to this perspective is that, according to 3.46, the pressure working is zero (and thus makes no contribution to α) at any location where $\mathbf{n} \cdot \widehat{\mathbf{u}}|_\partial = 0$. One example of this is the side walls in a longitudinal (two-dimensional) flow; despite the fact that a viscous boundary-layer is present at the wall, and that energy transfer occurs within this boundary-layer at leading order, according to the above pressure working arguments this region makes no contribution to the decay of the waves. Mei and Liu (1973) account for the leading-order transfer in the wall boundary-layer by considering the effect of the small meniscus region which exists at the side walls on the free surface. This is valid for the systems they considered (laboratory wave tanks), but for systems as large as lakes, the meniscus region is essentially insignificant. Therefore, throughout the rest of the paper we rely more on the physical arguments outlined in 3.4.1 and 3.4.2, particularly the energy dissipation perspective.

3.5 Applications 1: Simple systems

As discussed previously, analytical seiche solutions can only be found for a limited number of simple configurations (bathymetry and stratification). Even though these systems provide somewhat poor descriptions of real lakes, they still yield useful information about the dependence of α on $h(x, y)$ and $\overline{\rho}(z)$. We therefore begin by considering a few simple systems, and

continue with a numerical evaluation of some more realistic cases in the next section. The important characteristics of the behaviour of α can be conveniently illustrated for longitudinal seiches. For the sake of brevity we restrict attention to the fundamental longitudinal mode, often designated V1H1 in analogy to the rectangular basin solution. Previous work has shown that longitudinal seiches can be modelled reasonably accurately using a two-dimensional treatment (vertical, horizontal; Fricker and Nepf, 2000). This is particularly convenient for the numerical computations in the next section, since the use of a stream function formulation allows the problem to be cast in matrix eigenvalue form. The decay rates for other types of basin-scale internal wave motions, such as rotational modes, can also be computed from the formula for α in 3.37, since the only information required is a solution for the inviscid flow field $\mathbf{u_0}$. However, the few available analytical 3D solutions (such as a cylindrical lake with a flat bed) do not provide any more insight than the two-dimensional systems we consider. In addition, numerical solutions to the 3D problem (3.29 plus 3.31) is prohibitively difficult to solve (Fricker and Nepf, 2000).

3.5.1 Cylindrical and rectangular basins (3D flows)

The decay rate for basins with vertical side walls is comprised of separate contributions from the bed and wall boundary-layers. The flat bed portion is computed by setting $p_1 = p_2 = 0$ (i.e. $\mathbf{T} = (\mathbf{i}, \mathbf{j})$ or $(\mathbf{e}_r, \mathbf{e}_\theta)$), so that $|\eta|_{bed} = 1$ and $\mathbf{R} + \mathbf{R}' = \mathbf{I}$ (note that we do not put $\mathbf{R} = \mathbf{R}' = \mathbf{0}$). At the walls we can set $p_1 = 1$ (i.e. $\mathbf{t}_1 = \mathbf{k}$) and $p_2 = \mathbf{t}_2 \cdot \mathbf{k} = 0$, with $\mathbf{t}_2 = \pm\mathbf{i}, \mathbf{j}$ for a rectangular basin, or $\mathbf{t}_2 = \mathbf{e}_\theta$ for a cylinder. From the definitions of $\mathbf{R}$, $\mathbf{R}'$ and η (3.72, 3.69, and3.70), we then find

$$\mathbf{u}_{0wall}^{\mathrm{T}} \left(\mathbf{R} + |\eta|_{wall} \, \mathbf{R}' \right) \mathbf{u}_{0wall} = \left(|\eta| \, w_0^2 + u_{0t_2}^2 \right)_{wall} \ ,$$

with $|\eta|_{wall} = \left| 1 - N^2/\omega_0^2 \right|^{\frac{1}{2}}$. The decay rate is then

$$\frac{\alpha}{\omega_0} \cdot 4E = \int_{bed} \delta(\mathbf{s}) \frac{1}{2} \overline{\rho} \, |\mathbf{u}_{0bed}|^2 \, \mathrm{d}A_{bed} + \int_{walls} \delta(\mathbf{s}) \frac{1}{2} \overline{\rho} \left(|\eta| \, w_{0wall}^2 + u_{0t_2}^2 \right) \mathrm{d}A_{wall} \ ,$$

where u_{0t_2} is the wall tangential velocity normal to w_{0wall} (i.e. u_0/v_0 or $u_{\theta 0}$).

For a rectangular basin with constant $N > \omega_0$ and ν, the dynamic pressure is given by

$$P_0(\mathbf{x}) = \cos kx \cos ly \left(\frac{N^2}{2g} \sin mz + m \cos mz \right) e^{-\frac{N^2}{2g} z} ,$$

where $k = m_x \pi / L$, $l = m_y \pi / B$, $m = m_z \pi / H$ (with respective mode numbers $m_x, m_y, m_z = 0, 1, 2, ...$); L, B, H are the basin length, width, and depth, respectively; and the frequency satisfies the dispersion relation

$$\frac{N^2}{\omega^2} = \frac{k^2 + l^2 + m^2 + \frac{N^4}{4g^2}}{k^2 + l^2} .$$

Assuming constant viscosity ν (and δ), the decay rate for this system is

$$\frac{\alpha}{\omega_0} = \delta \frac{\omega_0^2}{N^2} \left[\frac{\epsilon_{m_y}}{B} \left(\frac{k^2}{k^2 + l^2} \left| \eta^2 \right| + |\eta| \right) + \frac{\epsilon_{m_x}}{L} \left(\frac{l^2}{k^2 + l^2} \left| \eta^2 \right| + |\eta| \right) + \frac{1}{2H} \frac{m^2}{k^2 + l^2} \right] , \qquad (3.49)$$

with $\left| \eta^2 \right| = N^2 / \omega_0^2 - 1$ and $\epsilon_0 = \frac{1}{2}$, $\epsilon_m = 1$ for $m > 0$. This result matches the rectangular basin decay rate computed by Dore (1969, § 5) except for a factor of 2 in the bed term resulting from the fact that Dore considered a system with a solid boundary at the surface. To compare the relative sizes of the various contributions to 3.49, note that

$$\eta^2 \sim \frac{N^2}{\omega_0^2} \sim \frac{1}{2\mu^2} \gg 1$$

for systems with lake-sized dimensions $L \gtrsim B \gg H$. The decay rate for such systems reduces approximately to

$$\frac{\alpha}{\omega_0} \sim \frac{\delta}{2} \left[\frac{1}{B} + \frac{1}{L} + \frac{1}{H} \right]$$

for $m_x \sim m_y \sim m_z \sim 1$. The bed contribution is clearly largest, suggesting that buoyancy factors (which appear in the side wall terms) are of little importance in large rectangular basins. (Note that this is not necessarily true for laboratory wave tanks, in which $L \sim B \sim H$.)

3.5.2 Longitudinal seiches (modelled as two-dimensional flows)

Throughout the rest of the paper we focus on longitudinal seiches, using a two-dimensional stream function formulation to compute both analytical and numerical solutions for the inviscid velocity field. As in the previous section the decay rate for a two-dimensional flow in the xz-plane (z vertical) is comprised of a bed component plus a contribution from the vertical side walls. The bed contribution follows from the general expression for α (3.37) by setting $\mathbf{t}_2 = \mathbf{j}$, so that $p_2 = \mathbf{t}_2 \cdot \mathbf{k} = 0$ and $u_{t_2} = v = 0$ (i.e. $\mathbf{u}_{0T} = (u_{0t}, 0)$). The $\mathbf{R}$-matrices in this case reduce to

$$\mathbf{R} = \begin{pmatrix} 0 & 0 \\ 0 & 1 \end{pmatrix} \qquad \mathbf{R}' = \begin{pmatrix} 1 & 0 \\ 0 & 0 \end{pmatrix} ,$$

so that

$$\mathbf{u}_{0bed}^{\mathrm{T}} \left(\mathbf{R} + |\eta| \, \mathbf{R}' \right) \mathbf{u}_{0bed} = |\eta_b| \, |\mathbf{u}_{0bed}|^2 \ .$$

The buoyancy coefficient evaluated at the bed is

$$\eta_b^2 = 1 - (\mathbf{t} \cdot \mathbf{k})^2 \frac{N^2}{\omega_0^2} = 1 - n_x^2 \frac{N^2}{\omega_0^2} ,$$

where n_x is the $\mathbf{i}$-element of the boundary-normal vector $\mathbf{n} = (n_x, n_z)$ (i.e., $\mathbf{t} = (-n_z, n_x)$ in the $\mathbf{i}, \mathbf{k}$-basis), and is equal to the local bed slope

$$n_x = \frac{dh}{dx} \left[1 + \left(\frac{dh}{dx} \right)^2 \right]^{-\frac{1}{2}} = \sin \theta_{bed} \ .$$

At the side walls the boundary normal is explicitly in the y-direction ($(\mathbf{t}_1, \mathbf{t}_2) = (\mathbf{i}, \mathbf{k})$, $(p_1, p_2) = (0, 1)$), so that

$$\mathbf{u}_{0wall}^{\mathrm{T}} \left(\mathbf{R} + |\eta| \, \mathbf{R}' \right) \mathbf{u}_{0wall} \ = \ u_0^2 + |\eta_w| \, w_0^2 \ ,$$

with $\eta_w^2 = 1 - N^2/\omega_0^2$. Putting all of this together, the decay rate is

$$\frac{\alpha}{\omega_0}\cdot 4E = B\int_{bed}\delta(s)\left|1-\frac{N^2}{\omega_0^2}\sin\theta_{bed}^2\right|^{\frac{1}{2}}\frac{1}{2}\overline{\rho}\left|\mathbf{u}_{0bed}\right|^2\mathrm{d}s \qquad (3.50)$$
$$+2\int_{wall}\delta(x,z)\frac{1}{2}\overline{\rho}\left(u_0^2+\left|1-\frac{N^2}{\omega_0^2}\right|^{\frac{1}{2}}w_0^2\right)\mathrm{d}x\mathrm{d}z\ ,$$

where B is the width of the basin. Dividing (3.50) by $4E$ (using 3.35) gives

$$\frac{\alpha}{\omega_0}=\frac{\alpha_{bed}}{\omega_0}+\frac{1}{2B}\frac{\int\delta_{wall}\frac{1}{2}\overline{\rho}\left(u_0^2+|\eta_w|\,w_0^2\right)\mathrm{d}x\mathrm{d}z}{\int\frac{1}{2}\overline{\rho}\left(u_0^2+w_0^2\right)\mathrm{d}x\mathrm{d}z}\ ,$$

where α_{bed}/ω_0 denotes the bed term. Since $w_0/u_0\sim\mu$ and $\eta_w\lesssim\mathcal{O}(\mu)$, the wall contribution to α is $\mathcal{O}(\delta_{wall}/B)$, and is therefore much smaller than $\alpha_{bed}/\omega_0\sim\mathcal{O}(\delta_{bed}/H)$. We therefore neglect the wall boundary-layer in the analyses in section 3.6. For longitudinal seiches in a rectangular basin, (3.50) reduces further to a sum of contributions from the bed (where $\eta^2=1$, since $\sin\theta_{bed}=0$) and the vertical end walls (where $\eta^2=1-N^2/\omega_0^2$),

$$\frac{\alpha}{\omega_0}\cdot 4\frac{E}{B}=\int_{bed}\delta(x)\frac{1}{2}\overline{\rho}u_{0bed}^2\mathrm{d}x+2\int_{end}\delta(z)\left|1-\frac{N^2}{\omega_0^2}\right|^{\frac{1}{2}}\frac{1}{2}\overline{\rho}w_{0end}^2\mathrm{d}z\ . \qquad (3.51)$$

For a basin with lake dimensions $H\ll L$, the end wall contributions vanish and α reduces to the homogeneous fluid result.

3.6 Applications 2: Numerical calculations

To investigate the factors affecting the viscous damping of internal seiches, we compute V1H1 seiche (inviscid) solutions and their corresponding decay coefficients α (3.37) for a series of idealised configurations. Three inputs are needed to fully determine α; to solve the governing equation (i.e. 3.55) we must specify the lake bathymetry and the background stratification $\overline{\rho}(z)$, and to compute α we require a representation or value for viscosity in the benthic boundary-layer. We discuss these inputs below.

3.6.1 Numerical method

For a two-dimensional system the velocities can be expressed in terms of a stream function,

$$\mathbf{u_0} \equiv \left(\frac{\partial \psi_0}{\partial z}, -\frac{\partial \psi_0}{\partial x} \right) \ , \tag{3.52}$$

which satisfies **u**-continuity. Eliminating the pressure and density from the momentum equations (see 3.6) yields the governing equation

$$\overline{\rho}^{-1} \boldsymbol{\nabla} \cdot (\overline{\rho} \boldsymbol{\nabla} \psi_0) - \frac{N^2}{\omega_0^2} \frac{\partial^2 \psi_0}{\partial x^2} = 0 \ , \tag{3.53}$$

with $\boldsymbol{\nabla} = (\partial/\partial x, \partial/\partial z)$. The no-flux boundary condition on $\mathbf{u_0}$ gives

$$\mathbf{n} \cdot \mathbf{u_0}|_\partial = \frac{\partial \psi_0}{\partial x_t}(0, x_t) = 0 \quad \overset{\int \mathrm{d}x_t}{\longrightarrow} \quad \psi_0|_\partial = 0 \ . \tag{3.54}$$

Equations (3.53) and (3.54) complete the inviscid problem. For non-uniform bathymetry and arbitrary stratification, it is not possible to find exact analytical solutions for this system. Internal seiche solutions are therefore evaluated numerically using a finite difference technique.

To begin, (3.53) is rewritten as

$$N^2 \frac{\partial^2 \psi_0}{\partial x^2} = \omega_0^2 \left(\frac{\partial^2 \psi_0}{\partial z^2} - \frac{N^2}{g} \frac{\partial \psi_0}{\partial z} + \frac{\partial^2 \psi_0}{\partial x^2} \right) \ , \tag{3.55}$$

in order to isolate the terms led by the frequency. Discretisation of (3.55) and the boundary conditions (3.54) results in a generalised matrix eigenvalue formulation,

$$\mathbf{N} \Psi_0 = \omega_0^2 \mathbf{M} \Psi_0 \ . \tag{3.56}$$

N denotes a matrix whose elements are determined in part by the buoyancy frequency (the left-hand side of (3.55)), while **M** corresponds to the discretisation of the right-hand side. If either **M** or **N** has an inverse, which is generally the case, then (3.56) can be rewritten as a standard eigenvalue problem. Solution of 3.56 therefore produces a finite set of inviscid internal seiche eigensolutions, which can then be used to compute α (3.37). Solutions are initially computed using a uniform grid, and then interpolated over a finer grid (using the condition $\psi_0|_\partial = 0$) for

an improved estimate of bed velocity. The method is described in more detail by Fricker and Nepf (2000).

Finally, note that the Boussinesq and hydrostatic terms in $\mathcal{L}\psi_0$ (i.e., in $\widetilde{\nabla}\cdot\left(\overline{\rho}\widetilde{\nabla}\psi_0\right)$),

$$\frac{1}{\overline{\rho}}\frac{\mathrm{d}\overline{\rho}}{\mathrm{d}z}\frac{\partial\psi_0}{\partial z} \qquad \text{and} \qquad \mu^2\frac{\partial^2\psi_0}{\partial x^2}\ ,$$

are usually very small for lakes, and as such should perhaps be treated formally as perturbation terms, the same as the τ. However, there is no analytical reason for taking this approach, since, unlike the stresses, these terms are easily incorporated into the numerical formulation for the zeroth-order problem (3.56). In addition, such a perturbation analysis is not tremendously illuminating, since we already have a more exact expression for α (3.37).

3.6.2 Model configurations and parameters

Basins

To explore the impact of bathymetry on the V1H1 seiche we perform two sets of computations, the first in a series of symmetric basins, the second in asymmetric basins. In all cases the length L and depth H of the lake are 10 km and 50 m respectively; these dimensions are chosen as typical, representative values, in order to have the Boussinesq and hydrostatic terms in (3.56) be of correct magnitude.

In normalised coordinates ($x \Leftrightarrow x/L$), the function

$$h(x) = \frac{\cosh\beta - \cosh\beta\,(2x-1)}{\cosh\beta - 1} \qquad \begin{array}{l} h(0) = h(1) = 0 \\ h\left(\frac{1}{2}\right) = 1 \end{array}\ , \tag{3.57}$$

describes symmetric basins ranging in shape from parabolic to rectangular. The parameter β essentially corresponds to an index of concavity, with the two extreme bathymetries given by $\beta \to 0$ (i.e. $h(x) \to 1-(2x-1)^2$) and $\beta \to \infty$ (rectangle). Solutions are computed for a set values of β which adequately span this range.

For asymmetric basins we choose a set of skewed parabolas, given by (see Münnich, 1996)

$$h(x) = \begin{cases} 1 - \dfrac{(x - x_0)^2}{x_0^2} & 0 < x < x_0 \\ 1 - \dfrac{(x - x_0)^2}{(1 - x_0)^2} & x_0 < x < 1 \end{cases} \tag{3.58}$$

The deepest point in each basin is located at $x = x_0$; the parameter x_0, which ranges from 0 to 0.5, represents the degree of skewness (parabola is $x_0 = 0.5$). We compute 11 solutions which span this range in steps of $\triangle x_0 = 0.05$.

Stratification

As the governing equation (i.e. 3.55) suggests, to evaluate seiche solutions it is actually simpler to specify the buoyancy frequency profile instead of $\overline{\rho}$. For typical summer stratification conditions in mid-latitude lakes, the maximum value of N^2 (denoted by N_0^2, at depth z_0) is on the order of 5 to $10 \times 10^{-3}\mathrm{s}^{-2}$. Above and below z_0, N^2 can be adequately simulated using linear functions,

$$N^2 = \begin{cases} N_0^2 \left[\dfrac{z - z_0 + \triangle_-}{\triangle_-} \right] & z_0 - \triangle_- < z < z_0 \\ -N_0^2 \left[\dfrac{z - z_0 - \triangle_+}{\triangle_+} \right] & z_0 < z < z_0 + \triangle_+ \end{cases} , \tag{3.59}$$

as shown in figure 3-3. In this notation the base of the epilimnion is $(z_0 - \triangle_-)$ and the bottom of the pycnocline is $(z_0 + \triangle_+)$. This piecewise linear profile describes the middle of the pycnocline quite well, and is also generally adequate for the top of the pycnocline, where the gradient is usually quite sharp. The density gradient at the bottom of the pycnocline frequently tails off more slowly than described by 3.59, and may not fit the parametrization quite as well. However, due to computational constraints we select a reasonable value for $\triangle_+$ by extending the linear-gradient region near mid-pycnocline down to $N^2 = 0$ (see figure 3-3).

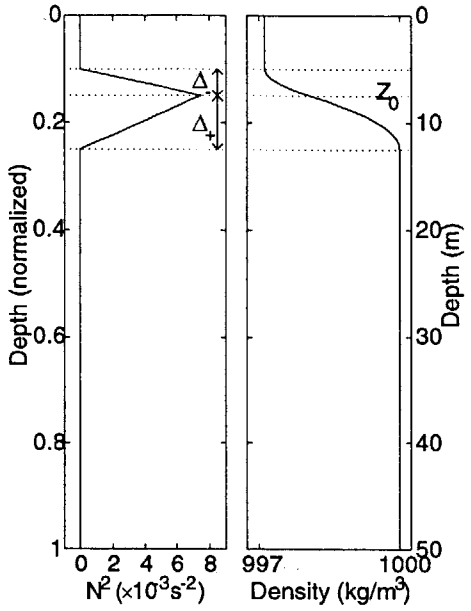

Figure 3-3: Idealized buoyancy frequency and density profiles used in the numerical internal seiche and damping coefficient computations.

The density profile corresponding to 3.59 is

$$\overline{\rho}(z) = \begin{cases} \rho_0 - \Delta\rho\left[1 - \dfrac{(z - z_0 + \Delta_-)^2}{\Delta_-(\Delta_+ + \Delta_-)}\right] & z_0 - \Delta_- < z < z_0 \\ \rho_0 - \Delta\rho\dfrac{(z - z_0 - \Delta_+)^2}{\Delta_+(\Delta_+ + \Delta_-)} & z_0 < z < z_0 + \Delta_+ \end{cases} \tag{3.60}$$

for N^2 defined using the Boussinesq approximation; $N^2 = g\rho_0^{-1}\mathrm{d}\overline{\rho}/\mathrm{d}z$. The maximum N^2 is thus given by

$$N_0^2 = g\frac{\Delta\rho}{\rho_0}\frac{2}{\Delta_+ + \Delta_-} \ .$$

We arrive at a convenient, consistent, and representative set of parameters by choosing $N_0^2 = 7.5 \times 10^{-3}\mathrm{s}^{-2}$, with the profile geometry

$$z_0 = 0.15H \qquad \Delta_- = 0.05H \qquad \Delta_+ = 0.1H \ .$$

For the chosen value of $H = 50\text{m}$, this corresponds to a surface layer which is $0.1H = 5\text{m}$ deep, and a gradient region which spans $0.15H = 7.5\text{m}$. With $\rho_0 = 1000\text{kg/m}^3$, the required surface-to-bed density difference is formally $\triangle\rho \approx 2.87\text{kg/m}^3$. This corresponds, for example, to a strong midsummer temperature difference of $\sim 6°\text{C}$ (hypolimnion) to $\sim 28°\text{C}$ (surface).

Viscosity within the boundary-layer

There is relatively little available information about viscosities (ν) or diffusivities in lake benthic boundary layers. The analysis in sections 3.2.3 and 3.3 was performed using a parameterization for bed stress (3.13) in which ν was allowed to vary as a function of position (i.e. with bed coordinates $\mathbf{s}$). In the final expression for α (3.37), ν is simply incorporated into the definition of boundary-layer thickness $\delta(\mathbf{s})$. Effectively, the dependence of α on ν is replaced by a dependence on δ; thus α can be computed using either parameter, with the formal relationship between the two being of lesser importance.

Using a numerical model with a $k-\varepsilon$ closure scheme, Hagatun and Eidsvik (1986) estimated boundary-layer viscosities for ocean surface waves (period $\sim 10\text{s}$) of the order $\nu_t \sim 10^{-4}u^2/\omega$. To apply this to much longer period seiches in the model configurations described above (without justification, in order to get a crude estimate of ν_t), we estimate the magnitude of the free stream velocity u from an estimated maximum seiche-induced vertical displacement, $\zeta_{\max}$, i.e., $u \sim \mathcal{O}\left(\mu^{-1}w_{\max}\right) \sim \mathcal{O}\left(\mu^{-1}\omega_0\zeta_{\max}\right)$. With $H = 50\text{m}$, a reasonable value for the displacement is $\zeta_{\max} \sim \mathcal{O}(0.5\text{m})$, or 10% of the water depth. Using the V1H1 seiche frequencies computed below ($\omega_0 \approx 1.4 \times 10^{-4}\text{s}^{-1}$), we find $u \sim \mathcal{O}\left(1.5\text{cms}^{-1}\right)$ and $\nu_t \sim \mathcal{O}\left(3 \times 10^{-4}\text{m}^2/\text{s}\right)$. With this, from the scaling analyses the boundary-layer thickness is predicted to be $\delta = (2\nu/\omega)^{\frac{1}{2}} \sim \mathcal{O}(2\text{m})$. In fact, in a real lake there is no basis for relating ν to the velocity field or frequency of any one seiche. In actuality the properties of the boundary-layer are determined by the overall seiche climate, as well as numerous other physical processes (such as seiche energy focusing, and progresive wave breaking), most of which are unsteady, and as yet poorly understood.

In one of the few field studies of boundary-layer viscosity, Gloor *et al.* (2000) estimated $\nu_t \sim 3 \times 10^{-5}\text{m}^2/\text{s}$ in Lake Alpnach (depth = 35m; see also Wüest and Gloor, 1998). This is an order of magnitude smaller than ν_t computed from the Hagatun and Eidsvik (1986) formula. Gloor *et al.* (2000, 1994) estimated boundary-layer thickness (δ_{obs}) directly from temperature

data, and observed substantial variations in δ_{obs} over each wave period. They also found a strong spatial dependence, with δ_{obs} ranging from $0-5$m (inversely correlated with buoyancy). In section 3.7.2, where we compute α for a series of model V1H1 seiche solutions, the results are expressed both in units of $\varepsilon = \delta/H$ and with $\delta = 2$m.

Finally, recall that we retained the spatial variation of $\nu(\mathbf{s})$ (and hence $\delta(\mathbf{s})$) throughout the analyses in §3.2 and 3.3. In lakes, viscosity and turbulence in the boundary-layer are likely magnified within the pycnocline due to the focusing and breaking of small-scale internal waves. (Note that this is distinctly different from the remainder of the water column, in which ν or $K_z \sim N^{-1}$ within the hypolimnion and the lower pycnocline; see, eg., Imboden and Wüest 1995, Michalski and Lemmin 1995.) In the epilimnion the boundary-layer is affected by wind-driven currents, which can also increase ν. In addition, near-bed diffusivities and the thickness of the boundary-layer are both unsteady (Gloor *et al.*, 2000). Unfortunatley, very little is known about these processes, and it is thus difficult to take spatial and temporal variations of ν,δ into account when computing α. Nonetheless, by carrying $\nu(\mathbf{s})$ through the analysis, the resulting expression for α (3.37) at least qualitatively illustrates the effect of differential ν,δ on seiche decay.

3.6.3 Numerical solutions

Eleven numerical V1H1 stream function solutions are evaluated for each of the symmetric ($\beta = (1, 1.5, 2, 3, 5, 10, 15, 20, 30, 50, 100)$) and asymmetric ($x_0 = n\triangle x_0$, $n = 0$ to 10) basins (see section 3.6.2). A sample of both sets are shown in figures 3-4 and 3-5, showing the evolution of seiche structure with changing bathymetry. The solutions are computed from (3.55)/(3.56) using a 40×40 (uniform) grid, and then interpolated over a finer grid (150×100 horizontal, vertical) for better resolution of the velocity field near the bed. The corresponding V1H1 seiche frequencies (normalised by the maximum value of the buoyancy frequency, $\max\left(N^2\right) = 0.0075$ s^{-2}) are presented in figure 3-6. In both cases $\omega_0/N_{\max}$ is remarkably insensitive to changes in bathymetry, varying by only $\sim$10 % over the range of computed parameter values. Note that, for a rectangular basin ($\beta \rightarrow \infty$ in the symmetric solutions), the governing equation and stream

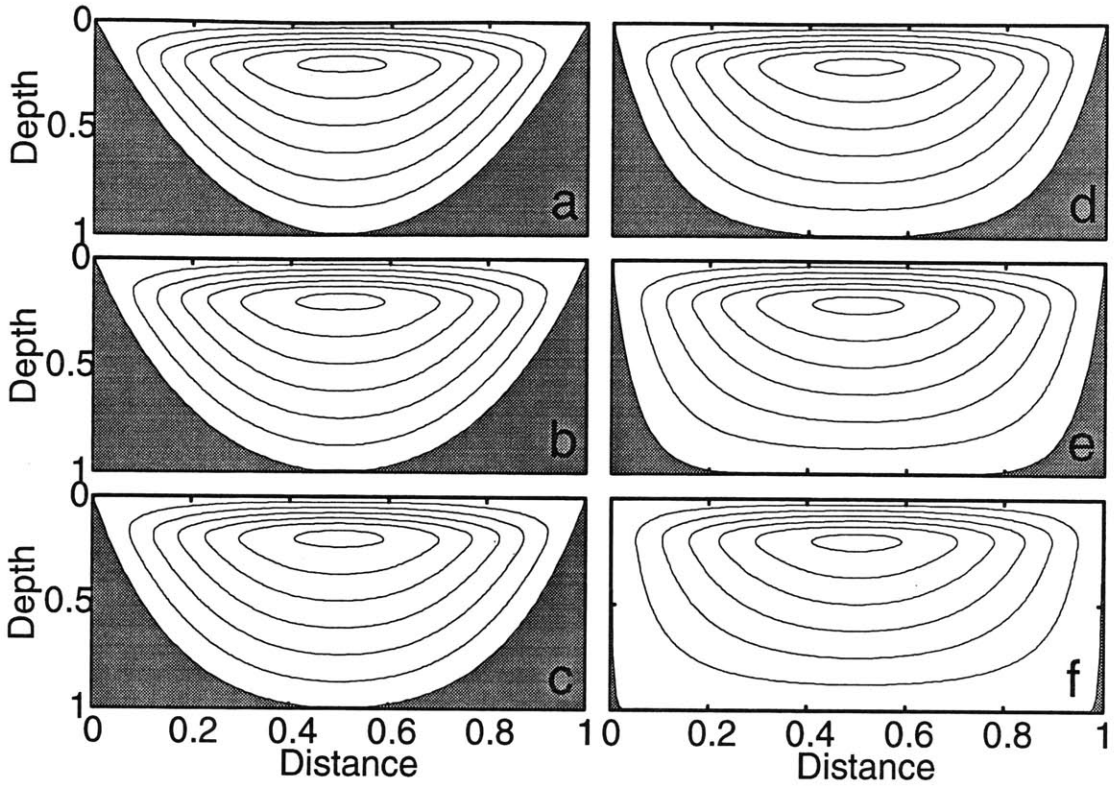

Figure 3-4: Streamfunction contours describing V1H1 internal seiche structure as a function of basin concavity β (from parabolic $\beta \to 0$ to rectangular $\beta \to \infty$), for the symmetric bathymetries defined in equation 3.57. The concavities are a) $\beta = 1$, b) $\beta = 2$, c) $\beta = 3$, d) $\beta = 5$, e) $\beta = 10$, f) $\beta = 100$. Five additional solutions were computed ($\beta = 1.5, 15, 20, 30, 50$), but are not shown. The contours range from $\psi_0 = 0$ on the boundary to $\psi_0 = 1$ in the center of the fluid.

function are separable, i.e., $\psi_0 = \chi(z) \sin kx$, with $k = n\pi/L$ ($n = 1, 2, ...$), and

$$\chi'' + \frac{N^2}{g}\chi' + k^2\left(\frac{N^2}{\omega_0^2} - 1\right)\chi = 0 \ . \tag{3.61}$$

Specifying the horizontal mode number (i.e., $n = 1$ for the V1H1 seiche), accurate numerical solutions to this system can be obtained very easily, since the location of each eigenvalue within the manifold of solutions is known (in particular, the V1H1 frequency represents an extremum eigenvalue; this is not the case for the two-dimensional problem, see Fricker and Nepf, 2000). Using a discretisation of 500 points, we evaluate $\omega_0/N_{\max} \approx 1.511 \times 10^{-3} \approx 0.302\mu$ from (3.61),

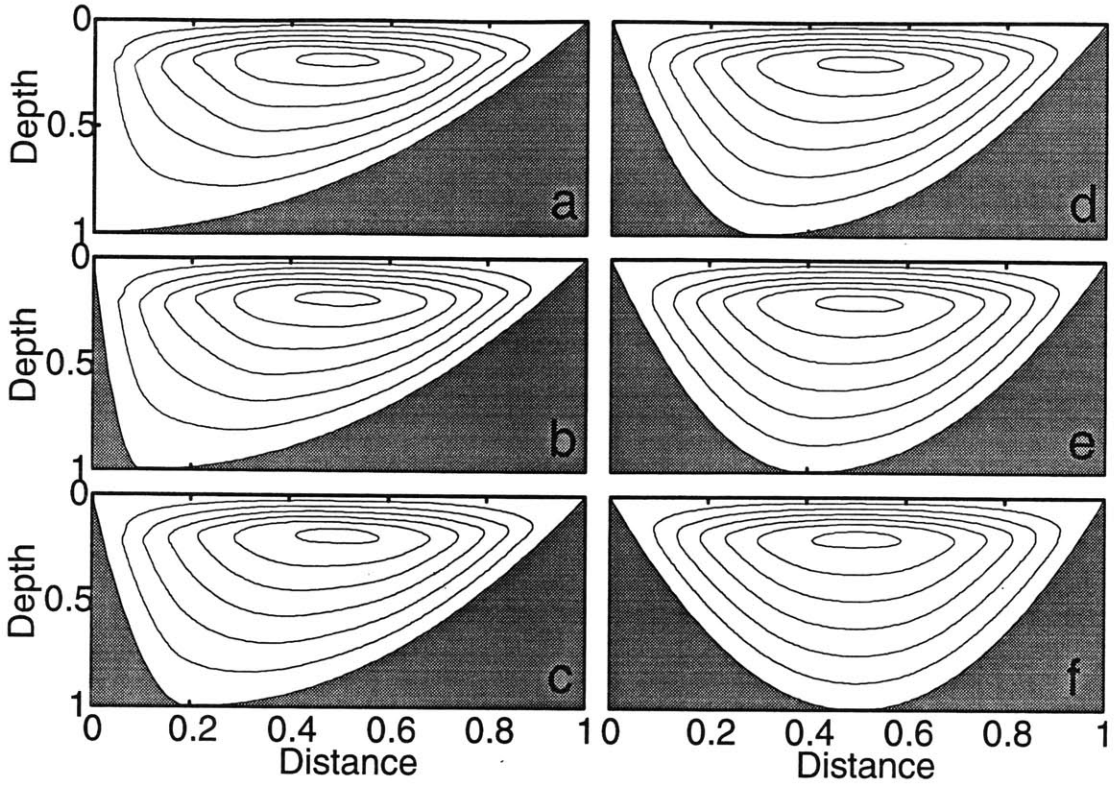

Figure 3-5: Streamfunction contours describing V1H1 internal seiche structure as a function of x_0 (the location of maximum depth) for the symmetric bathymetries defined in equation 3.58. The figures correspond to a) $x_0 = 0$, b) $x_0 = 0.1$, c) $x_0 = 0.2$, d) $x_0 = 0.3$, e) $x_0 = 0.4$, f) $x_0 = 0.5$. Five additional solutions ($x_0 = 0.5, 1.5, 2.5, 3.5, 4.5$) are not shown. The contours range from $\psi_0 = 0$ on the boundary to $\psi_0 = 1$ in the center of the fluid.

versus $\omega_0/N_{\max} \approx 1.512 \times 10^{-3}$ for $\beta = 100$ in the two-dimensional formulation (3.55). The 'exact' rectangular basin frequency is marked by a dashed line in figure 3-6.

3.7 Results and discussion

3.7.1 Buoyancy and the benthic boundary-layer

From the matching conditions for the boundary-layer and outer flows $\mathbf{u_0}|_\partial = -\mathbf{U_0}|_\partial$, the velocity field throughout the entire fluid is given by

$$\mathbf{q_0} = \mathbf{u_0} - \left(\mathbf{R}\mathrm{e}^{-(1+\mathrm{i})\sigma^{-1}\xi_n} + \mathbf{R}'\mathrm{e}^{-(1+\phi\mathrm{i})\sigma^{-1}|\eta|\xi_n}\right)\mathbf{u_0}|_\partial \ .$$

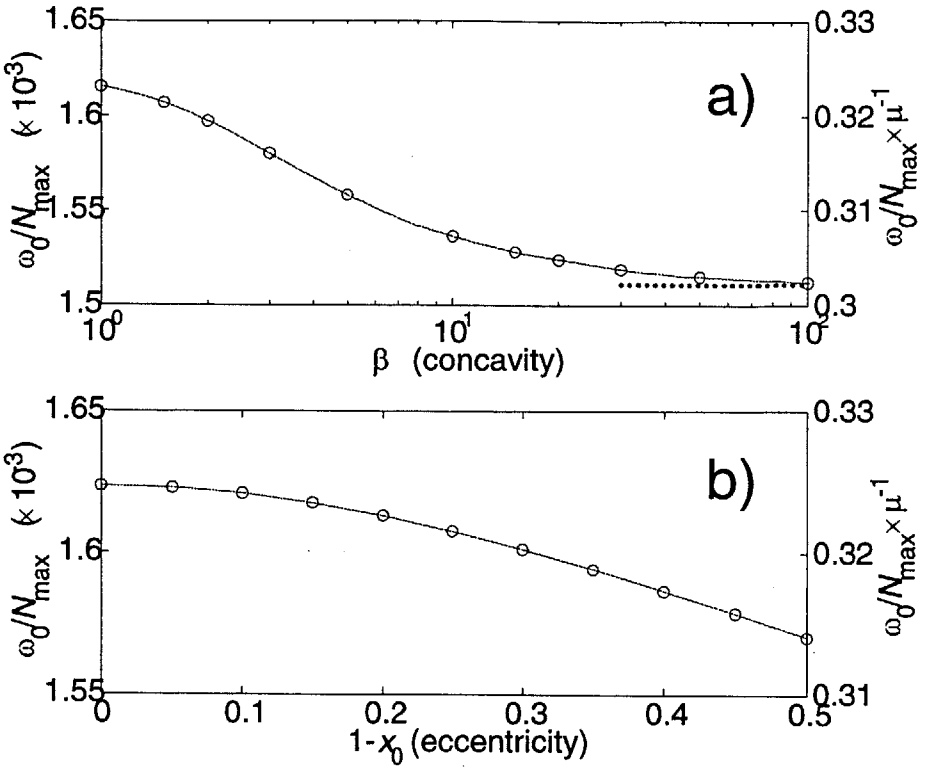

Figure 3-6: V1H1 seiche frequency as a function of concavity β and eccentricity $(1 - x_0)$ for the V1H1 solutions shown in figures 3-4 and 3-5. In both cases the left-hand side represents the parabolic (or nearly-parabolic) basin. The rectangular basin frequency is marked with a dashed line in figure a).

From the results in section 3.4.1, where we showed that the decay rate can also be computed as the integral of bed stress (Henderson and Miles, 1994), we see that the difference between the surface and internal wave decay rates essentially corresponds to the difference between the boundary-layer flow $\mathbf{U_0}$ for homogeneous versus stratified fluids. To explore the effect of stratification on $\mathbf{U_0}$ and α, consider the decay rate for longitudinal seiches in the xz-plane derived in section 3.5.2,

$$\frac{\alpha}{\omega_0} = \text{bed term} + \frac{1}{2E}\int_{wall} \delta(x,z)\,\frac{1}{2}\overline{\rho}\left(u_0^2 + \left|1 - \frac{N^2}{\omega_0^2}\right|^{\frac{1}{2}} w_0^2\right) \mathrm{d}x\mathrm{d}z \ . \tag{3.62}$$

Although the side wall terms were shown to be $\mathcal{O}(\delta/B) < 1$ for longitudinal seiches, it is convenient to use the vertical wall portion of α to illustrate the impact of buoyancy on the structure of the boundary-layer.

Note that the w-contribution to the wall boundary integral in (3.62) vanishes at locations z_c where the local buoyancy frequency matches the seiche frequency, $N(z_c) = \omega_0$. (In fact, the bed integral vanishes entirely wherever $\omega_0^2/N^2 = \sin^2\theta_{bed}$; see equation (3.50).) For a typical mid-summer thermal stratification $N(z_c) = \omega_0$ occurs at two depths in the water column, at the top and 'bottom' of the pycnocline. Returning to the z-momentum equation for the boundary-layer flow (3.14),

$$\mathrm{i}\omega_0\overline{\rho}\left(1-\frac{N^2}{\omega_0^2}\right)W_0 = \overline{\rho}\nu\nabla^2 W_0 + \frac{\partial(\overline{\rho}\nu)}{\partial x_k}\left(\frac{\partial W_0}{\partial x_k}+\frac{\partial U_{0k}}{\partial z}\right) \quad ,$$

we see that the integral vanishes when the leading-order acceleration and buoyancy terms on the left-hand side cancel each other. Mathematically, the solution for W_0 in (3.74) is not valid at z_c because 'higher-order' terms in the momentum equation are not negligible there as assumed (or more accurately over a small region $z_c \pm \varepsilon$; Dore 1969). Fortunately, the error introduced in α by neglecting these terms and simply applying W_0 at z_c is negligible at leading order, so that no modification to W_0 or α is necessary. It is easier to understand the physical significance of this cancellation by considering the w-momentum equation for the outer flow, applied at the wall,

$$\mathrm{i}\omega_0\eta^2\,\overline{\rho}w_0|_\partial = -\left.\frac{\partial P_0}{\partial z}\right|_\partial \quad . \tag{3.63}$$

At z_c, where the buoyancy and acceleration terms match ($\eta^2(z_c) = 1 - N^2(z_c)/\omega_0^2 = 0$), the vertical pressure gradient is zero. In fact, since $\eta^2(z_c)$ changes sign at z_c, the pressure gradient at the wall has opposite sign inside and outside the pycnocline. This has important implications for the structure of the boundary-layer flow in these two regions, as we illustrate next.

The velocity field at the vert cal side wall is

$$\mathbf{q}_{0wall} = \begin{pmatrix} q_{0h} \\ q_{0v} \end{pmatrix} = \begin{pmatrix} u_0(x,z)\left(1-\mathrm{e}^{-(1+\mathrm{i})\frac{y}{\delta}}\right) \\ w_0(x,z)\left(1-\mathrm{e}^{-(1+\phi\mathrm{i})|\eta|\frac{y}{\delta}}\right) \end{pmatrix} \quad , \tag{3.64}$$

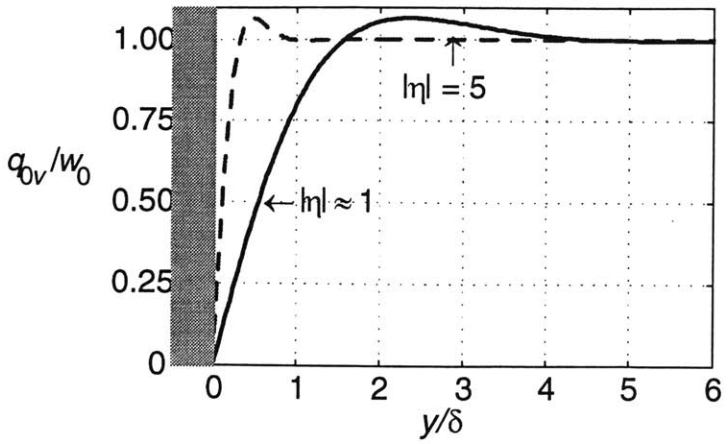

Figure 3-7: Comparison of the boundary layer structure and shear length δ' for q_{0v} (3.64) at the side wall, outside ($|\eta| \approx 1$) and inside ($|\eta| > 1$) the pycnocline. The velocity profile corresponds to the time of maximum free stream velocity.

where we have omitted spatial variations in viscosity for simplicity (i.e. $\sigma \Rightarrow 1$, $\delta = (2\nu/\omega_0)^{\frac{1}{2}} \Rightarrow$ constant). The horizontal velocity is simply the conventional Stokes solution for an oscillating flow over a flat plate. The vertical velocity, on the other hand, is modified by the scale factor $|\eta|$. In particular, note that the vertical component of shear at the wall is

$$\left.\frac{\partial q_{0v}}{\partial y}\right|_{wall} = (1+\phi\mathrm{i})\,\frac{|\eta|}{\delta} w_0\,(x,z) \quad . \tag{3.65}$$

We can define a shear length $\delta' = \delta/|\eta|$ which describes the rescaled distance over which the free stream velocity w_0 decays to zero at the wall (figure 3-7). The relationship between δ' and the physical boundary-layer thickness δ_{BL} is unclear, since δ_{BL} at any location is obviously the same for all components of the velocity field, and is determined by many physical factors. Within the pycnocline the increased pressure gradient outside the boundary-layer due to large buoyancy forces ($\partial P_0/\partial z \propto \eta^2$; see (3.63)) leads to a small δ' in this region. This in turn means a substantially increased wall stress $\propto w_0/\delta'$ (3.65), and a much larger contribution to α ($\propto \int u \cdot \tau \mathrm{d}x_n$, (3.39)). At points z_c near the top and bottom of the pycnocline, q_{0v} is indeterminate, δ' becomes very large, and the vertical pressure gradient, shear stress, and contribution to α vanish. In reality, in the region $z_c \pm \varepsilon$, higher-order terms are important in

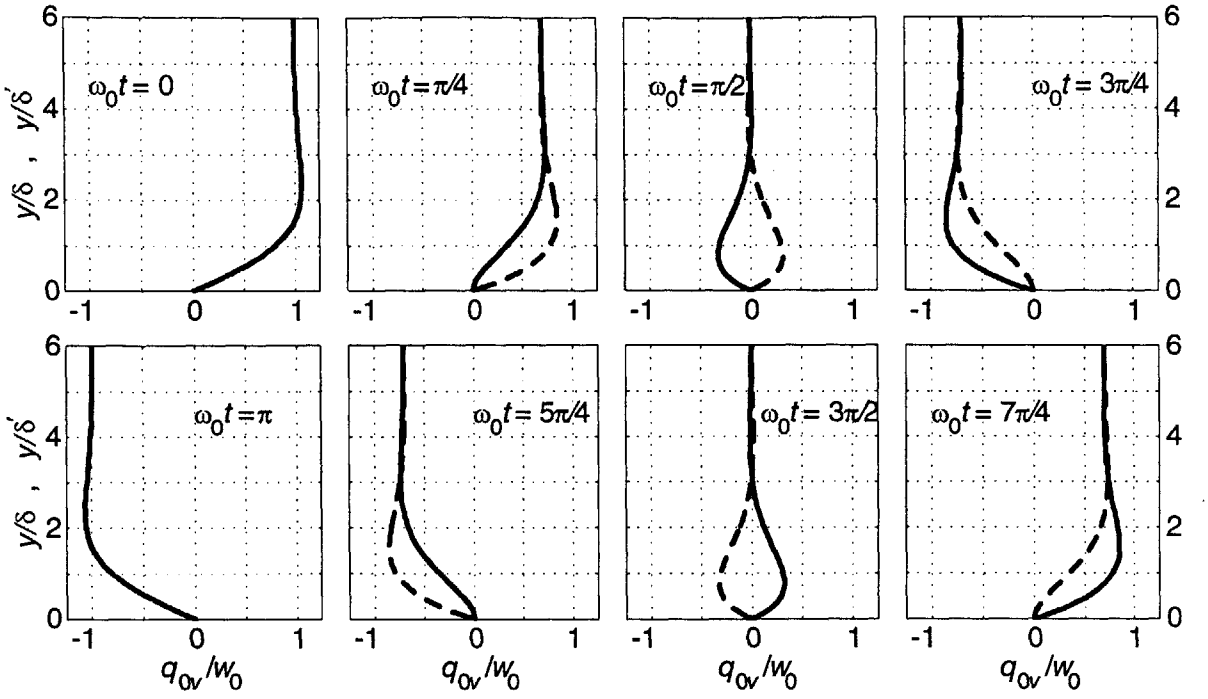

Figure 3-8: Evolution of the wall boundary layer over one wave period (the coordinate axes are rotated so that y is vertical). The solid line shows the conventional Stokes BL (thickness scale δ) which applies for the region where $N < \omega_0$, while the dashed line shows the modified structure (δ') of the BL within the pycnocline ($N > \omega_0$).

the momentum balance, so that q_{0v} is well-behaved, and δ' is bounded.

The structure of q_{0v} also depends on the phase coefficient ϕ, which changes sign at z_c along with $\partial P_0/\partial z$ (3.63). Outside the pycnocline $\phi > 0$, $|\eta| \approx 1$, and $\delta' \approx \delta$, and the boundary-layer structure of q_{0v} is again the standard Stokes solution. However, within the pycnocline ($\phi < 0$, $|\eta| > 1$, $\delta' < \delta$) the structure of the flow is modified; writing out the full solution for both cases,

$$\mathrm{Re}\left[\frac{q_{0v}}{w_0} e^{i\omega_0 t}\right] = \begin{cases} \cos\omega_0 t - e^{-\frac{y}{\delta}} \cos\left(\frac{y}{\delta} - \omega_0 t\right) & \text{outside pycnocline} \\ \cos\omega_0 t - e^{-\frac{y}{\delta'}} \cos\left(\frac{y}{\delta'} + \omega_0 t\right) & \text{within pycnocline} \end{cases} .$$

These solutions are plotted in figure 3-8 for several values of t to illustrate the differences (over a wave period) in boundary-layer structure in the two regions. Note that, because of the

relationship between the dynamic density field and the vertical velocity (3.5), i.e.,

$$\rho = -\mathrm{i}\frac{\overline{\rho}N^2}{g\omega_0} q_{0v} \ ,$$

the boundary-layer velocity profiles in figure 3-8 also describe the isopycnal displacements. The negative phase coefficient ϕ within the pycnocline causes the boundary-layer flow to lag the free stream velocity instead of lead. Note that the acceleration of fluid inside and outside the pycnocline differs by 180°. For example, moving from $\omega_0 t = \pi$ to $\omega_0 t = 2\pi$, the conventional Stokes profile (solid line) accelerates faster than the modified pycnocline profile during the first quarter-period (until $\omega_0 t = 3\pi/2$), but then accelerates slower, allowing the pycnocline flow to catch up again at $\omega_0 t = 2\pi$, i.e. when the outer flow reaches a maximum. Interestingly, despite this change in boundary-layer structure the phase change has no impact on the decay rate, since ϕ does not appear in the expression for α (see 3.37); the magnitude of α is thus only affected by the buoyancy factor η. This is a consequence of the fact that α is period-averaged, as described in section 3.4. Using the notation $\widehat{f}(\mathbf{x},t) = \mathrm{Re}\left[f(\mathbf{x})\,\mathrm{e}^{\mathrm{i}\omega t}\right]$ introduced in section 3.4.2, from (3.65) we find

$$\widehat{\tau}\cdot\widehat{\mathbf{u}}|_{wall} = \overline{\rho}\nu\frac{|\eta|}{\delta}\frac{w_0^2}{2}\bigg|_{wall}\left[1+\sqrt{2}\sin\left(2\phi\omega_0 t+\frac{1}{4}\pi\right)\right] \ .$$

The second term in the square brackets vanishes when averaged over a wave period, regardless of the sign of ϕ. Describing the vertical outer flow in terms of the vertical displacement field, $w_0 = \partial\zeta_0/\partial t$, we can rewrite (3.63) as

$$\left.\frac{\partial P_0}{\partial z}\right|_\partial \approx \begin{cases} \omega_0^2\,\overline{\rho}\zeta_0|_\partial & \text{outside pycnocline} \\ -\overline{\rho}N^2\zeta_0|_\partial & \text{within pycnocline} \ . \end{cases} \tag{3.66}$$

This clearly illustrates the relationship between the fluid motion and the pressure gradient at the top of the boundary-layer. Outside the pycnocline, where the pressure gradient is simply due to the oscillation of the fluid (pressure ~acceleration), $\partial P_0/\partial z$ and the dynamic displacement ζ_0 have the same sign. However, within the pycnocline an additional pressure gradient arises because the water moves to a location of different buoyancy. For example, when an isopycnal moves upward, buoyancy forces push it down; the pressure gradient thus has opposite sign to

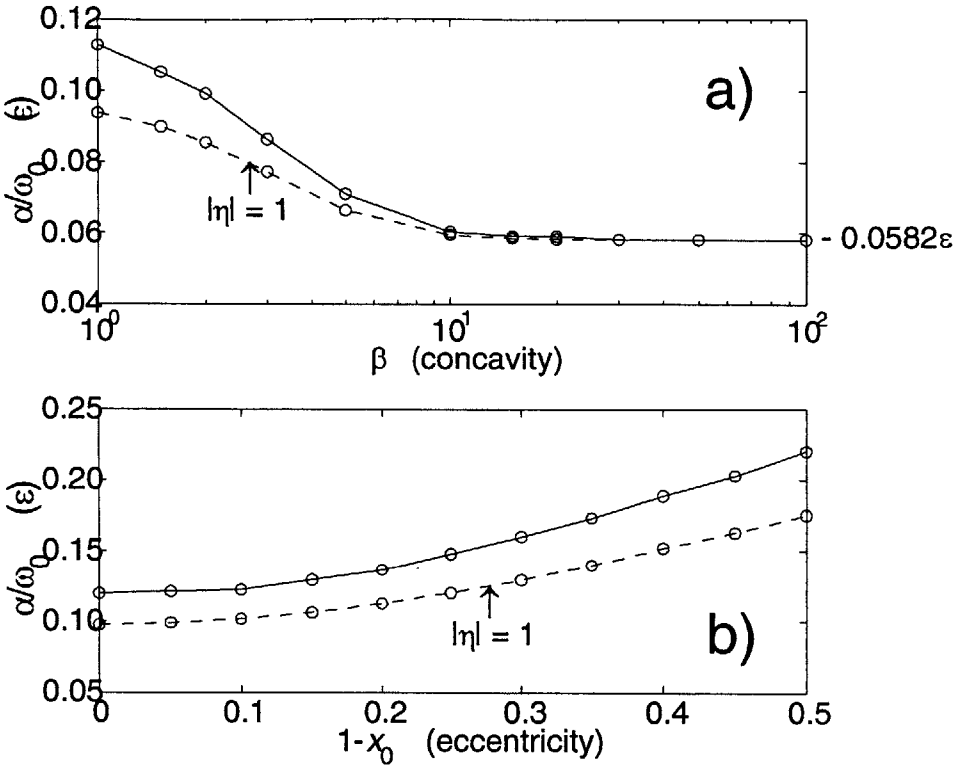

Figure 3-9: Decay rate (α) as a function of concavity β and eccentricity ($1 - x_0$) for the V1H1 seiche solutions shown in figures 3-4 and 3-5. In both cases the left-hand side represents the parabolic (or nearly-parabolic) basin. The decay rate for the rectangular basin ($\beta \to \infty$ in figure a)) is $\alpha \approx 0.0582\varepsilon$. $|\eta| = 1$ corresponds to the the decay rate when buoyancy effects are neglected.

ζ_0 (and is also larger than the acceleration term), as (3.66) shows.

3.7.2 Decay rates

Decay rates for the 22 numerical V1H1 seiche solutions in section 3.6.3 are computed using (the bed portion of) (3.50). The results are presented in figure 3-9 (solid lines). The dashed lines correspond to α for $|\eta| = 1$, i.e., when buoyancy effects are neglected (denoted $\alpha_{|\eta|=1}$). The symmetric basin results in figure 3-9a) show that buoyancy causes α to be $\sim$20 % larger than $\alpha_{|\eta|=1}$ in the parabolic basin ($\beta \to 0$). Interestingly, this is comparable to the contribution of internal damping to the decay of surface waves in cylinders (Henderson and Miles 1994; Martel, Nicolás, and Vega 1998; Miles and Henderson 1998). As β increases and the basin becomes

more rectangular we find $\alpha \rightarrow \alpha_{|\eta|=1}$, because buoyancy effects are confined to the vanishingly small vertical end wall contributions (see the rectangular basin result (3.51) in §3.5.2). The rectangular basin decay rate is approximated by the $\beta = 100$ result, $\alpha/\omega_0 \approx 0.0582\varepsilon$. This can again be compared to the separable rectangular basin solution, for which the decay rate expression reduces to

$$\frac{\alpha}{\omega_0} = \frac{\overline{\rho}(H)\chi'^2(H)\int_{bed}\delta(x)\sin^2 kx\mathrm{d}x}{2L\int_0^H \overline{\rho}(\chi'^2+k^2\chi^2)\,\mathrm{d}z} \approx \frac{\delta_{bed}\overline{\rho}(H)(\chi'(H))^2}{4\int_0^H \overline{\rho}(z)(\chi'(z))^2\,\mathrm{d}z} \quad ,$$

assuming constant δ_{bed}. Using the V1 eigenvector (i.e., $\chi(z)$) which was computed with ω_0 in section 3.6.3 (for 500 grid points), we find $\alpha/\omega_0 \approx 0.0588\varepsilon$, in excellent agreement with the two-dimensional result. The results in figure 3-9a) clearly demonstrate the limitations of using a rectangular basin model to describe the structure and decay of internal seiches. Not only do the parabolic and rectangular basin decay rates differ by a factor of > 2, but also, since α and $\alpha_{|\eta|=1}$ become equal as $\beta \rightarrow \infty$, the rectangular basin decay rate cannot adequately describe the effect of buoyancy.

In the asymmetric basins (figure 3-9b)), in all cases buoyancy/bathymetry effects lead to a 20-26% increase in α versus $\alpha_{|\eta|=1}$. In addition, both α and $\alpha_{|\eta|=1}$ almost double as the eccentricity increases from 0 to 0.5. This is primarily because the near-bed velocities increase over the milder sloping region as the bed slope decreases. This can easily be seen in figure 3-5, which shows the contraction of the stream function contours (corresponding to an increase in $u_{bed} \sim \partial\psi/\partial x_n$) as the basin becomes progressively more skewed. Note that since ω_0 is essentially independent of basin shape (figure 3-6), the observed variations in α in both the symmetric and asymmetric basins are due solely to changes in the velocity field and the factor $|\eta|$.

3.8 Conclusions

We have derived a generalised expression for the rate of viscous damping of internal seiches (α) by modifying an inviscid formulation (velocity field $\mathbf{u}$) with the addition of a viscous benthic boundary-layer flow (i.e., $\mathbf{q} = \mathbf{u} + \mathbf{U}$), and performing a perturbation analysis. The decay rate is proportional to the integral of kinetic energy at the bed, modified by a coefficient

($\eta = \eta\left(\overline{\rho}(z), h(x,y), \omega_0\right)$) which accounts for the effects of buoyancy and bathymetry. The surface wave decay rate (i.e., homogeneous fluid; Mei and Liu, 1973) is retrieved from α by setting $\eta = 1$. Physically, α can be interpreted as the rate of a) stress working by the seiche on the bed boundary (Henderson and Miles 1994), b) viscous dissipation of energy within the boundary-layer, or c) pressure working by the seiche on the boundary-layer (Mei and Liu 1973).

A series of V1H1 internal seiche numerical solutions were computed using a two-dimensional (linear, inviscid) stream function model, formulated as a matrix eigenvalue problem. These solutions were then used to compute α. The results show that bathymetry and buoyancy effects (i.e. η) give rise to a $\sim$20% increase in α, except for basins with rectangular bathymetry, where the η-contribution becomes vanishingly small. This underscores the limitations of using a simple rectangular basin model to describe seiche structure (particularly bed velocities) and decay. Damping rates computed for a set of asymmetric basins show that α increases with increasing basin eccentricity, due to the magnification of velocities over the progressively shallower bed slope. This result suggests that bathymetries which include a region of convex bed slope, i.e., a shoal over which velocities are substantially magnified (see, eg., Fricker and Nepf 2000), should exhibit still greater magnification of seiche damping, especially when the depth of the shoal coincides with the location of the pycnocline (maximum N^2).

Using the stress working perspective (Henderson and Mile 1994), bed stresses τ_{bed} are computed using the leading-order inviscid-plus-boundary-layer velocity field, $\mathbf{q_0}$, which is a modified form of Stokes' solution for an oscillating flow over a flat plate. The magnification of α (versus $\alpha_{\eta=1}$) is caused by increasing bed shear $\sim \mathbf{u_0}|_\partial / \delta'$ due to decreasing shear length $\delta' \approx (2\nu/\omega_0)^{\frac{1}{2}} / (N \sin\theta_{\mathbf{bed}})$ within the pycnocline (ν = viscosity, N = buoyancy frequency, $\sin\theta_{\mathbf{bed}}$ = bed slope). For vertical or upslope motion, the structure of the boundary-layer within the pycnocline is also modified by a phase factor $\phi = \text{sign}\left(\eta^2\right)$ which changes sign (at depth(s) z_c) where the local buoyancy frequency matches the seiche frequency, $N(z_c) = \omega_0$. The change in ϕ causes the boundary-layer flow to lag the outer flow instead of lead. This results from the fact that the dynamic pressure gradient at the top of the boundary-layer within the pycnocline has opposite sign to the dynamic vertical displacement field ζ_0 (i.e., $\partial P_0/\partial z|_\partial \propto \phi\, \zeta_0|_\partial$ with $\phi = -1$, where $w_0 = \partial\zeta_0/\partial t$).

3.9 Appendix: Solution for the boundary-layer flow

In mixed vector/tensor notation, the boundary-layer governing equations are

$$\mathrm{i}\omega\mathbf{U} = \mathrm{i}\omega\frac{N^2}{\omega^2}W\mathbf{k} + \frac{1}{\overline{\rho}}\frac{\partial}{\partial x_k}\left[\overline{\rho}\nu\left(\frac{\partial U_j}{\partial x_k} + \frac{\partial U_k}{\partial x_j}\right)\right]e_j \ , \tag{3.67}$$

where e_j is a basis vector (for example $e_j = \{\mathbf{i},\mathbf{j},\mathbf{k}\}$ or $\{\mathbf{t}_1,\mathbf{t}_2,\mathbf{n}\}$). Since the zeroth-order flow in the boundary-layer is parallel to the boundary, i.e. $\{U_{0j}\} = (U_{0t_1}, U_{0t_2})$, it is more convenient to write (3.67) solely in terms of $\mathbf{U}_{0T}$ and the $\mathbf{T} = (\mathbf{t}_1,\mathbf{t}_2)$ basis. To begin, we can express $\mathbf{k}$ in terms of the boundary basis trivially as

$$\mathbf{k} = (\mathbf{t}_1\cdot\mathbf{k})\,\mathbf{t}_1 + (\mathbf{t}_2\cdot\mathbf{k})\,\mathbf{t}_2 + (\mathbf{n}\cdot\mathbf{k})\,\mathbf{n} = (\mathbf{T}\cdot\mathbf{k})\cdot\mathbf{T} + (\mathbf{n}\cdot\mathbf{k})\,\mathbf{n} \ .$$

The velocities $\mathbf{U}$ (or $\mathbf{u}$) can be written using either basis, $\mathbf{U} = (U,V,W) = (U_{t_1}, U_{t_2}, U_n)$. The zeroth-order vertical velocity can therefore be expressed in terms of the $\mathbf{T}$ as

$$W_0 = \mathbf{k}\cdot\mathbf{U}_0 = U_{0t_1}\mathbf{k}\cdot\mathbf{t}_1 + U_{0t_2}\mathbf{k}\cdot\mathbf{t}_2 = \mathbf{U}_{0T}\cdot(\mathbf{T}\cdot\mathbf{k}) \ ,$$

since $U_n = 0$. This relation is used to eliminate W from (3.67) (as well as the boundary-layer equation (3.25) and the expression for the decay rate α (3.37)).

To continue, using the scalings in (3.16) and the definition of the boundary-layer thickness δ (3.15), the $\mathbf{T}$-components of (3.67) become

$$\begin{aligned} 2\mathrm{i}\frac{\omega}{\omega_0}\mathbf{U}_{0T} &= 2\mathrm{i}\frac{\omega}{\omega_0}\frac{N^2}{\omega^2}\left(\mathbf{U}_{0T}\cdot(\mathbf{T}\cdot\mathbf{k})\right)((\mathbf{T}\cdot\mathbf{k})\cdot\mathbf{T}) + \delta^2\frac{1}{\overline{\rho}}\frac{\partial}{\partial x_k}\left[\overline{\rho}\sigma^2\left(\frac{\partial\mathbf{U}_{0T}}{\partial x_k} + \boldsymbol{\nabla}_T U_{0k}\right)\right] \\ &\approx 2\mathrm{i}\frac{\omega}{\omega_0}\frac{N^2}{\omega^2}\left(\mathbf{U}_{0T}\cdot(\mathbf{T}\cdot\mathbf{k})\right)((\mathbf{T}\cdot\mathbf{k})\cdot\mathbf{T}) + \sigma^2\widehat{\nabla}^2\mathbf{U}_T + \mathcal{O}\left(\frac{\delta^2}{H^2}\right) \ . \end{aligned}$$

(Note that the $\mathbf{n}$-equation includes higher-order terms, and thus represents an inhomogeneous governing equation for the $\mathbf{U}_1$, etc.) The $\mathcal{O}(\varepsilon^2)$ terms involve derivatives of $\overline{\rho}$ and σ^2, which are assumed to be slowly-varying functions of space within the boundary-layer. Writing out

the (zeroth-order) $\mathbf{t}_1$ and $\mathbf{t}_2$ equations separately

$$\begin{aligned}\left[\frac{\partial^2}{\partial\xi_n^2} - 2\mathrm{i}\sigma^{-2}\left(1 - \frac{N^2}{\omega_0^2}(\mathbf{t}_1\cdot\mathbf{k})^2\right)\right]U_{0t_1} &= -2\mathrm{i}\sigma^{-2}\frac{N^2}{\omega_0^2}(\mathbf{t}_1\cdot\mathbf{k})(\mathbf{t}_2\cdot\mathbf{k})\,U_{0t_2}\\ \left[\frac{\partial^2}{\partial\xi_n^2} - 2\mathrm{i}\sigma^{-2}\left(1 - \frac{N^2}{\omega_0^2}(\mathbf{t}_2\cdot\mathbf{k})^2\right)\right]U_{0t_2} &= -2\mathrm{i}\sigma^{-2}\frac{N^2}{\omega_0^2}(\mathbf{t}_1\cdot\mathbf{k})(\mathbf{t}_2\cdot\mathbf{k})\,U_{0t_1}\end{aligned}$$

clearly shows that the pair is coupled, due to both buoyancy and bathymetry effects. For a homogeneous fluid ($N^2 = 0$, i.e. for surface waves) the equations both reduce to the simple Stokes boundary-layer problem for $\mathbf{U}_{0T} = (U_{0t_1}, U_{0t_2})$. As written, they can be summarised in the matrix equation

$$\left(\frac{\partial^2}{\partial\xi_n^2} - 2\mathrm{i}\sigma^{-2}\mathbf{M}\right)\mathbf{U}_{0T} = 0 \tag{3.68}$$

by defining

$$\mathbf{M} \equiv \mathbf{I} - \frac{N^2}{\omega_0^2}\left(p_1^2 + p_2^2\right)\mathbf{R}' \;, \qquad \mathbf{R}' \equiv \frac{1}{p_1^2 + p_2^2}\begin{pmatrix} p_1^2 & p_1p_2 \\ p_1p_2 & p_2^2 \end{pmatrix} \;, \tag{3.69}$$

in which $p_i = \mathbf{t}_i \cdot \mathbf{k}$ are the projections of the $\mathbf{t}_i$ in the vertical. To solve (3.68) we take $U_{0t_1}, U_{0t_2} \sim \mathrm{e}^{\lambda t}$, and evaluate the λ as solutions to the determinantal equation

$$\left|\lambda^2\mathbf{I} - 2\mathrm{i}\sigma^{-2}\mathbf{M}\right| = 0 \;.$$

The solutions are simply $\lambda^2 = 2\mathrm{i}\sigma^{-2},\ 2\mathrm{i}\sigma^{-2}\eta^2$, where we have set

$$\eta^2 \equiv 1 - \frac{N^2}{\omega_0^2}\left(p_1^2 + p_2^2\right) \;. \tag{3.70}$$

Omitting the two positive roots to $\left(\lambda^2\right)^{\frac{1}{2}}$ because we require $\mathbf{U}_0\left(\boldsymbol{\xi}_T, \xi_n \to \infty\right) \to 0$, the general solution for $\mathbf{U}_{0T}$ is

$$\mathbf{U}_{0T} = \mathbf{C}\left(\boldsymbol{\xi}_T\right)\mathrm{e}^{-(1+\mathrm{i})\sigma^{-1}\xi_n} + \mathbf{D}\left(\boldsymbol{\xi}_T\right)\mathrm{e}^{-(1+\phi\mathrm{i})\sigma^{-1}|\eta|\xi_n} \;,$$

where $\mathbf{C} = (C_1, C_2)$, $\mathbf{D} = (D_1, D_2)$, and $\phi = \mathrm{sign}\left(\eta^2\right)$. Placing this solution into the governing

equations gives the relations

$$(\mathbf{I}-\mathbf{M})\,\mathbf{C}=\mathbf{0} \qquad (\eta^2\mathbf{I}-\mathbf{M})\,\mathbf{D}=\mathbf{0}\ ,$$

which reduce to

$$\mathbf{R}'\mathbf{C}=\mathbf{0} \qquad \mathbf{R}\mathbf{D}=\mathbf{0}\ , \tag{3.71}$$

upon substitution of $\mathbf{M}$ (3.69). Here we have introduced the new matrix

$$\mathbf{R}\equiv\mathbf{I}-\mathbf{R}'=\frac{1}{p_1^2+p_2^2}\begin{pmatrix} p_2^2 & -p_1p_2 \\ -p_1p_2 & p_1^2 \end{pmatrix}\ . \tag{3.72}$$

Using the fact that $\mathbf{R}+\mathbf{R}'=\mathbf{I}$, as well as equations (3.71), we can also write

$$\mathbf{R}\mathbf{C}=\mathbf{C} \qquad \mathbf{R}'\mathbf{D}=\mathbf{D}\ . \tag{3.73}$$

These relations are used below.

Moving now to the matching/boundary conditions $\mathbf{u}|_\partial = -\,\mathbf{U}|_\partial$, we find from the general solution for $\mathbf{U_{0T}}$ that

$$\mathbf{U}_{0T}\,(\boldsymbol{\xi}_T,0)=\mathbf{C}+\mathbf{D}=-\,\mathbf{u_0}|_\partial\ .$$

Operating on this equation with $\mathbf{R}'$ and using (3.71) and (3.73) gives

$$\mathbf{C}=-\mathbf{R}\,\mathbf{u_0}|_\partial\ .$$

Likewise for $\mathbf{D}$ we find

$$\mathbf{D}=\mathbf{R}'\,\mathbf{u_0}|_\partial\ .$$

The final solution for the boundary-layer flow is therefore

$$\mathbf{U}_{0T}\left(\boldsymbol{\xi}_T, \xi_n\right) = -\left(\mathbf{R}\mathrm{e}^{-(1+\mathrm{i})\sigma^{-1}\xi_n} + \mathbf{R}'\mathrm{e}^{-(1+\phi\mathrm{i})\sigma^{-1}|\eta|\xi_n}\right)\mathbf{u_0}|_\partial \ , \tag{3.74}$$

with $\mathbf{R}$ and $\mathbf{R}'$ as defined in (3.72) and (3.69).

We briefly note a few additional properties of the matrices $\mathbf{R}$, $\mathbf{R}'$, and $\mathbf{M}$ which are used in the derivation of α. First, from the definitions of $\mathbf{R}$ and $\mathbf{R}'$ (3.72 and 3.69) it is easily verified that

$$\mathbf{R}\mathbf{R}' = \mathbf{0} \ , \qquad \mathbf{R}^2 = \mathbf{R} \ , \qquad \mathbf{R}'^2 = \mathbf{R}' \ .$$

Using these relations and the definition of $\mathbf{M}$ (3.69), we find

$$\mathbf{R}\mathbf{M} = \mathbf{R} \ , \qquad \mathbf{R}'\mathbf{M} = \eta^2\mathbf{R}' \ .$$

Bibliography

[1] Acheson, J. D., 1992. Elementary Fluid Mechanics. Oxford University Press Inc.

[2] Craig, P. D., 1991. Incorporation of damping into internal wave models. *Cont. Shelf Res.*, **11**(6): 563-577.

[3] Dore, B. D., 1968a. Oscillations in a non-homogeneous viscous fluid. *Tellus*, **20**: 514-523.

[4] Dore, B. D., 1968b. Viscous damping effects in long waves on the rotating earth. *Quart. J. Mech. and Appl. Math.*, **21**: 105-114.

[5] Dore, B. D., 1969. The decay of oscillations of a non-homogeneous fluid within a container. *Proc. Camb. Phil. Soc.*, **65**: 301-307.

[6] Fischer, H. B., E. J. List, R. C. Y. Koh, J. Imberger, and N. H. Brooks, 1979. Mixing in Inland and Coastal Waters. Academic Press, Inc.

[7] Fricker, P. D. and H. M. Nepf, 2000. Stratification, bathymetry, and internal seiche structure. *J. Geophys. Res.*, **105**(C6): 14,237-14,252.

[8] Gloor, M., A. Wüest, and M. Münnich, 1994. Benthic boundary mixing and resuspension induced by internal seiches. *Hydrobiologia,* **284**: 59-68.

[9] Gloor, M., A. Wüest, and D. M. Imboden, 2000. Dynamics of mixed bottom boundary layers and its implications for diapycnal transport in a stratified, natural water basin. *J. Geophys. Res.*, **105**(C4): 8629-8646.

[10] Henderson, D. M., and J. W. Miles, 1994. Surface-wave damping in a circular cylinder with a fixed contact line. *J. Fluid Mech.*, **275**: 285-299.

[11] Hukuda, H., 1986. On the damping of gravity oscillations in closed basins. *Dyn. Atmos. Oceans,* **10**: 97-109.

[12] Imberger, J., 1998. Flux paths in a stratified lake: A review. In: Physical Processes in Lakes and Oceans. Coastal and Estuarine Studies 54. American Geophysical Union, Washington DC.

[13] Imboden, D. M. and A. Wüest, 1995. Mixing Mechanisms in Lakes. In: Physics and Chemistry of Lakes, Eds. A. Lerman, D. M. Imboden, and J. R. Gat. Springer-Verlag.

[14] Johns, B., 1968. A boundary layer method for the determination of the viscous damping of small amplitude gravity waves. *Quart. J. Mech. and Appl. Math.*, **21**: 93-103.

[15] Kerswell, R. R., and C. F. Barenghi, 1995. On the viscous decay rates of inertial waves in a rotating circular cylinder. *J. Fluid Mech.*, **285**: 203-214.

[16] Landau, L. D., and E. M. Lifshitz, 1987. Fluid Mechanics, 2nd edition. Course of Theoretical Physics, Volume 6. Pergamon Press.

[17] Martel, C., J. A. Nicolás, and J. M. Vega, 1998. Surface-wave damping in a brimful circular cylinder. *J. Fluid Mech.*, **360**: 213-228.

[18] Mei, C. C., and P. L.-F. Liu, 1973. The damping of surface gravity waves in a bounded liquid. *J. Fluid Mech.*, **59**: 239-256.

[19] Mei, C. C., 1992. The Applied Dynamics of Ocean Surface Waves. Advanced Series on Ocean Engineering - Volume 1. World Scientific.

[20] Michalski, J. and U. Lemmin, 1995. Dynamics of vertical mixing in the hypolimnion of a deep lake: Lake Geneva. *Limnol. Oceanog.*, **40**(4): 809-816.

[21] Miles, J. W., and D. M. Henderson, 1998. A note on interior vs. boundary-layer damping of surface waves in a circular cylinder. *J. Fluid Mech.*, **364**: 319-323.

[22] Münnich, M., 1996. Influence of bottom topography on internal seiches in stratified media. *Dyn. Atmos. and Oceans*, **23**: 257-266.

[23] Orlić, M., 1984. The influence of bottom friction on transverse internal seiches in rotating rectangular channels. *Arch. Met. Geophy. Biocl.*, Ser. A 33: 175-185.

[24] Sanford, T. B., and R.-C. Lien, 1999. Turbulent properties in a homogeneous tidal bottom boundary layer. *J. Geophys. Res.*, **104**(C1): 1245-1257.

[25] Ursell, F., 1952. Edge waves on a sloping beach. *Proc. R. Soc.*, **A 214**: 79-97.

Chapter 4

The effect of buoyancy and bathymetry on internal seiche decay

Abstract[1]

We compute viscous decay rates (α) for internal seiches in lakes as the rate of stress working by the seiche on the bed boundary. Stresses are computed using a velocity field which is modified by adding a viscous benthic boundary-layer flow. This flow is modeled as a modified form of Stokes' solution for an oscillating flow over a flat plate, in which the outer flow drops to zero at the bed over the distance $\delta' = \delta / |\eta|$, ($\delta = \sqrt{2\nu/\omega}$, with ν the viscosity), which we denote as the 'shear length'. The resulting expression for α corresponds to the integral of kinetic energy at the bed (as for surface waves) multiplied by a coefficient (η) which accounts for the effects of buoyancy and bathymetry. Within the pycnocline, the momentum equation reveals that BL stresses are balanced by substantially magnified buoyancy forces (corresponding to larger η), instead of acceleration. To balance buoyancy, the viscous stresses ($\tau \propto u_{\text{bed}}/\delta'$) become magnified through a reduction in $\delta' \propto |\eta|^{-1}$. The relationship between the shear length and the physical benthic boundary-layer thickness is explored.

As an application, decay rates are computed for the dominant internal seiches (VnH1, n = 1,2,3) in the Upper Mystic Lake (UML, Winchester, Massachusetts). We find that higher vertical modes have progressively slower damping rates, and that buoyancy effects contribute to the rapid decay of the V1H1 seiche. Although α for the V3H1 mode is also magnified, it is still ~five times smaller than the V1H1

[1]To be submitted to *JGR - Oceans.*

decay rate, which accounts for the relative persistence of the V3H1 mode. Since there is no apparent resonance between wind forcing and seiche response in the UML system, differences in α are believed to be a major factor determining seiche climate.

4.1 Introduction

We investigate the effects of buoyancy and bathymetry on the viscous damping of internal seiches in lakes. Surface and internal wave decay rates (α) in shallow water are related to bed velocity structure (for example, $\alpha \propto$ shear stress, or kinetic energy). Previous studies have shown that seiche structure (and therefore α) is determined by bathymetry and stratification ($h(x)$ and $\overline{\rho}(z)$), and that bed velocities can be substantially magnified for certain lake configurations. We show here that, for baroclinic seiches, α is modified by an additional factor which describes the impact of buoyancy and bathymetry on bed shear. These effects can lead to substantially enhanced damping in lakes whenever a region of magnified bed velocities coincides with the pycnocline. Temperature data and numerical simulations of the dominant seiches in the Upper Mystic Lake (Winchester, Massachusetts) are used to demonstrate this effect.

The damping of large-scale waves in lakes is due primarily (i.e. at leading order) to viscous dissipation of wave energy at the boundaries[2] [*Gloor et al.*, 2000; *Fricker and Nepf* 2000a; Chapter 2]. Decay rates are thus often computed by adding a viscous benthic boundary-layer (BL) or bed stress parameterization to an inviscid model. Using the former approach, α can be derived from a perturbation analysis as the complex portion of the leading-order frequency shift. This method was applied to surface waves by *Dore* [1968a] and *Mei and Liu* [1973], to internal and interfacial waves by *Johns* [1968], *Dore* [1968b; 1969], and *Fricker and Nepf* [2000b; Chapter 3], and to the flow in a rotating cylinder by *Kerswell and Barenghi* [1995]. Alternatively, using the bed stress parameterization, α can be computed as the rate of stress working by the waves on the boundary, i.e., $\alpha \propto \int_\partial u\tau_{bed} ds$. *Henderson and Miles* [1994] used this technique to assess surface wave damping in a cylinder, using Stokes' solution for an oscillating flow over a plate to describe the BL flow q, and approximating the wall and bed stresses using the normal shear, $\tau_{bed} = \rho\nu\partial q/\partial x_n$. The resulting expression for α is identical to the perturbation method solution [*Fricker and Nepf*, 2000b; Chapter 3]. *Gloor et al.* [2000] and *Fricker and Nepf* [2000a; Chapter 2] used the conventional parameterization $\tau_{bed} = C_d\overline{\rho}u_d^2$

[2]This assumption is likely valid for large systems such as lakes. However, in small systems such as laboratotory tanks, damping is also affected by dissipation within the free surface boundary-layer and by contact-line dynamics at the walls (Henderson and Miles 1994). In addition, recent studies have shown that dissipation within the body of the fluid is not necessarily negligible in small containers; Howell *et al.* 2000, Martel *et al.* 1998, Miles and Henderson 1998.

(d = height above the bed) to determine α from model internal seiche solutions. Finally, several authors have computed decay rates by adding stress terms directly to the momentum equations. *Hukuda* [1986] used a linear stress relation with bottom friction coefficient $\tau = Cu$, followed by a perturbation analysis, to e aluate surface wave damping. *Orlič* [1984] employed depth-averaged surface, bed, and interface stresses with a two-layer model of transverse seiches in a channel. And *Craig* [1991] added both internal shear stress terms to the governing equation and a modified boundary condition with friction coefficient to compute internal seiche solutions in a uniform stratification. However, despite this large body of literature, a generalized formulation for internal seiches for arbitrary stratification and bathymetry has only recently been explored [*Fricker and Nepf* 2000b; Chapter 3].

4.2 Internal seiche decay

The decay rate for internal seiches can be determined by adding a viscous benthic boundary layer flow $\mathbf{U}$ to the inviscid velocity field $\mathbf{u}$ [*Fricker and Nepf*, 2000b; Chapter 3]:

$$\mathbf{q} = \mathbf{u} + \mathbf{U} \ , \qquad \mathbf{q}|_{\partial} = \mathbf{0} \ , \tag{4.1}$$

in which $\mathbf{U}$ vanishes a short distance away from the bed (denoted by ∂, with boundary coordinate s). Using (4.1) as a starting point, wave and seiche decay rates can be computed a) using a perturbation analysis [see, e.g., *Mei and Liu*, 1973; *Fricker and Nepf*, 2000a; Chapter 3], or as b) the rate of stress working by the seiche on the boundary [*Henderson and Miles*, 1994], c) the rate of viscous dissipation of energy within the benthic BL, or d) the rate of pressure working by the seiche on the BL [*Mei and Liu*, 1973]. Using the bed stress perspective [*Henderson and Miles*, 1994], α for surface seiches is given by

$$\alpha = \frac{1}{4E} \mathrm{Re}\left[\int_{\partial} u_j^* \tau_{nj} ds\right] \ , \qquad E = \int_{\Omega} \frac{1}{2}\overline{\rho}\,|\mathbf{u}|^2 \, dxdz \ , \tag{4.2}$$

where $(\,)^*$ represents the complex conjugate, E is the total seiche energy, and $\tau_{nj} = n_i \tau_{ij}$, with $\{n_i\} = \mathbf{n}$ the boundary unit normal vector. For longitudinal seiches (and the 2D formulation) we assume the side wall contributions to α are negligible (formally $\mathcal{O}(H/B)$, with B the lake

width). In the boundary integral u_j is the inviscid or outer flow velocity field, while the stresses $\tau_{nj} \propto \partial q_i/\partial x_n$ are evaluated using the modified flow.

From the linearized density-continuity relation $\mathrm{D}\rho/\mathrm{D}t = 0$ and (4.1), the dynamic density field $\rho'(x,z,t) \equiv \rho(x,z,t) - \overline{\rho}(z)$ is related to the vertical velocity by

$$\rho' = -i\omega \frac{d\overline{\rho}}{dz}(w+W) \ .$$

Using this relation the momentum equations can be partitioned into separate outer flow and boundary-layer (BL) equations,

$$i\omega\overline{\rho}u_j = -g\frac{1}{i\omega}\frac{d\overline{\rho}}{dz}w\delta_{j2} + \frac{\partial P'}{\partial x_j} \ , \tag{4.3}$$

$$i\omega\overline{\rho}U_j = -g\frac{1}{i\omega}\frac{d\overline{\rho}}{dz}W\delta_{j2} + \frac{\partial \tau_{jk}}{\partial x_k} \ , \qquad \tau_{jk} = \overline{\rho}\nu\left(\frac{\partial U_j}{\partial x_k} + \frac{\partial U_k}{\partial x_j}\right) \ , \tag{4.4}$$

respectively. Here $u_j = \{u, w\}$, $U_j = \{U, W\}$ and $\delta_{12} = \mathbf{i}\cdot\mathbf{k} = 0$, $\delta_{22} = \mathbf{k}\cdot\mathbf{k} = 1$ is the Kronecker delta, with $\mathbf{i}$ and $\mathbf{k}$ basis vectors in the x and z directions. The outer flow equation (4.3) is simply the conventional balance between acceleration, buoyancy, and dynamic pressure P'. Following the standard formulation for thin BLs, in (4.4) the momentum balance involves the viscous stresses τ instead of P'. The boundary condition for this system is simply the matching condition $\mathbf{U}|_\partial = -\mathbf{u}|_\partial$. In addition, leading-order continuity and the no-flux condition on $\mathbf{u}$ also require that $\mathbf{n}\cdot\mathbf{U} = 0$, so that $\mathbf{U}$ is parallel to the boundary. We can therefore define a unit vector $\mathbf{t}$ which is parallel to the boundary (i.e. $\mathbf{t}\cdot\mathbf{n} = 0$), such that $\mathbf{U} = U_t\mathbf{t}$. Applying the continuity scalings $w/u \sim W/U \sim H/L = \mu$, and assuming constant viscosity ν, at leading order (4.4) reduces to

$$\delta^2\frac{\partial^2\mathbf{U}}{\partial x_n^2} = i\omega\left[1 - \frac{N^2}{\omega^2}\sin^2\theta_{bed}\right]\mathbf{U} \ , \qquad \delta = \sqrt{\frac{2\nu}{\omega}} \ll 1 \ , \tag{4.5}$$

with $x_n = \mathbf{n}\cdot\mathbf{x}$, and $\mathbf{n}(s)$ the unit normal vector at the boundary and $\mathbf{k}\cdot\mathbf{t} = n_x = \sin\theta_{bed}$ the local bed slope. In (4.5) we have also used the fact that $\partial\tau_{jk}/\partial x_k \approx \overline{\rho}\nu\partial U/\partial x_n$, as well as the conventional BL scaling $\delta = \sqrt{2\nu/\omega}$. Written in this form, (4.5) suggests that the BL can be broken up into two distinct regions. Outside the pycnocline, where $N \approx 0$, the bed stresses are balanced by acceleration, and the BL has conventional Stokes form. However, within the

pycnocline (specifically, when $\omega < N \sin\theta_{bed}$) the stresses are balanced by buoyancy forces. This has implications for the structure of the BL within the pycnocline, as we demonstrate below.

To solve (4.5) it is convenient to define the buoyancy/bathymetry factor $\eta(z)$

$$\eta^2 \equiv 1 - \frac{N^2(z)}{\omega^2} \sin^2\theta_{bed} \ , \qquad (4.6)$$

which can be further rewritten as $\eta^2 = |\eta(z)|^2 \phi$, with phase coefficient $\phi = \text{sign}(\eta^2)$. From (4.5), and using the boundary condition $\mathbf{U}|_\partial = -\mathbf{u}|_\partial$ (see (4.1)), the velocity field $\mathbf{q}$ for the entire system is

$$\mathbf{q}(x,z) = \mathbf{u}(x,z) - \mathbf{u}|_\partial \, e^{-(1+\phi i)\frac{x\eta}{\delta'}} \ , \qquad \delta' = \frac{\delta}{|\eta|} \ . \qquad (4.7)$$

This is simply the Stokes solution for an oscillating flow over a plate, modified by the buoyancy and bathymetry effects described by η^2 (4.6). In (4.7) we introduced the rescaled thickness δ', which we describe as the shear length, in order to make the distinction between this parameter and the physical (observed) BL thickness. To estimate the magnitude $|\eta|$, and hence the size of δ' relative to δ, note from the dimensional scalings in the previous paragraph that the bed slope is $\sin\theta_{bed} \sim H/L$. Using the constant-$N$ result $N/\omega \sim L/H$ (see, e.g., *Maas and Lam* [1995]), for a system with pycnocline thickness h_{pyc} ($\sim (0.1 - 0.2)\, H$) we estimate $N/\omega \sim L/h_{\text{pyc}}$. Thus, within the pycnocline we expect $|\eta| > 1$, so that the magnitude of δ' ($\propto \delta/|\eta|$) is smaller than δ in this region. The impact of increasing δ' on the BL structure is depicted in Figure 4-1, which shows BL velocity profiles (for maximum $|\mathbf{q}(t)|$ during the wave period) for the region outside the pycnocline (i.e., $|\eta| = 1$, the conventional Stokes solution), as well as a representative value $|\eta| = 5$ within the pycnocline. While the two profiles have the same form, the profile within the pycnocline is contracted due the rescaled thickness δ'. Equation (4.5) shows that, within the pycnocline, the magnitude of the BL stresses (the left-hand side of the equation) must increase in order to balance the magnified buoyancy term. We thus expect buoyancy/bathymetry effects to lead to an increase in the decay rate.

Equation (4.7) was also obtained by *Wunsch* [1969] for progressive internal waves in a uniform stratification (constant N) encountering a constant-slope boundary [see also *Cacchione*

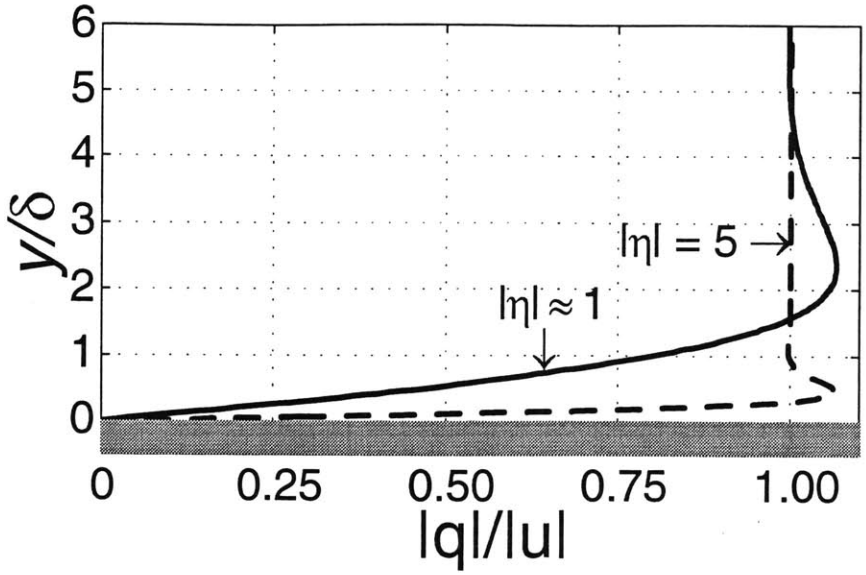

Figure 4-1: Boundary layer velocity profiles for $|\eta| = 1$ and $|\eta| = 5$.

and Wunsch, 1974; *Cacchione and Southard*, 1974]. In a series of wave tank experiments, *Cacchione and Wunsch* [1974] studied the impact of the relationship between incident wave angle and bed slope, for the subcritical ($\omega/N < \sin\theta_{bed}$; $\eta^2 < 0$), critical ($\omega/N = \sin\theta_{bed}$; $\eta^2 = 0$), and supercritical ($\omega/N > \sin\theta_{bed}$; $\eta^2 > 0$) cases. They demonstrated that as ω/N approaches $\sin\theta_{bed}$, amplification of the incident waves leads to instabilities and mixing along the entire slope. (For non-uniform stratification and non-constant slope, the results of *De Silva et al.* [1997] suggest that amplification and mixing is highly localized to the critical region, i.e., where $\eta^2 = 0$) However, *Cacchione and Wunsch* [1974] did not investigate variations in BL thickness, and specifically, by restricting attention to constant-N fluids, did not consider a system in which δ' varies with position along the boundary. (Such measurements would have been difficult at any rate, since the thickness of the BL in the experiments was ~ 3 mm.) As far as we are aware, such observations have only recently been made (in Lake Alpnach), as we discuss in Section 4.4 below.

Returning to the analysis of α, using (4.7) and the definition of δ (4.5), the bed stresses are

$$\boldsymbol{\tau}_{0n}|_{\partial} = \overline{\rho}\nu\frac{\partial \mathbf{q}_0}{\partial x_n}\bigg|_{\partial} = \overline{\rho}\nu\,(1+\phi i)\,\frac{\mathbf{u}_0}{\delta'}\bigg|_{\partial} = (1+\phi i)\,\frac{1}{2}\omega_0\overline{\rho}\delta\,|\eta|\,\mathbf{u}_0\bigg|_{\partial} \quad . \tag{4.8}$$

As this relation shows, the bed shear is $\partial \mathbf{q_0}/\partial x_n|_\partial \sim \mathbf{u_0}/\delta'|_\partial$; the shear length δ' is therefore the distance over which the free stream velocity drops to zero at the bed. Substituting (4.8) into (4.2), the decay rate for internal seiches is

$$\frac{\alpha}{\omega_0} = \frac{\delta}{4E}\int_\partial |\eta| \frac{1}{2}\overline{\rho}\,|\mathbf{u_0}|^2\, ds \ . \tag{4.9}$$

This is simply the integral of the kinetic energy at the bed weighted by $|\eta|$, which accounts for the effects of buoyancy and bathymetry. Clearly α increases with increasing $|\eta|$. Note that when $|\eta| = 1$, α reduces to the decay rate for surface waves ($\alpha_{|\eta|=1}$) [see, e.g., *Henderson and Miles*, 1994]. Internal seiche damping is often estimated by assuming that α is proportional to the fraction of seiche kinetic energy within the BL (i.e. α with $|\eta| = 1$; see, e.g., *Fischer et al.* [1979]). For comparison we compute both α and $\alpha_{|\eta|=1}$.

Finally, it was stated above that α also represents rate of dissipation of seiche energy within the viscous benthic BL,

$$\frac{dE}{dt} = -2\alpha E \simeq -\frac{1}{2}\,\mathrm{Re}\left[\int_{V_{BL}} \boldsymbol{\tau}_{0n} \cdot \frac{\partial \mathbf{q}_0^*}{\partial x_n} ds dx_n\right] \ .$$

The rate of internal seiche damping thus also corresponds to the rate of generation of turbulence energy within the BL (see *Fricker and Nepf*, [2000b]). The decay rate α therefore provides an estimate for the amount of wind energy that is ultimately available for benthic mixing.

4.2.1 Numerical model for the inviscid flow

To model the structure of longitudinal internal seiches we use a 2-dimensional (linear, inviscid) stream function formulation,

$$\mathbf{u} \equiv \left(\frac{\partial \psi}{\partial z}, -\frac{\partial \psi}{\partial x}\right) \ .$$

For wave motion we assume

$$f(\mathbf{x}, t) \rightarrow \mathrm{Re}\left[f(\mathbf{x})\, e^{i\omega t}\right]$$

for all the dynamic fields $f = (\psi, \rho', P')$. Eliminating the pressure and density from the linearized 2D momentum and continuity equations

$$i\omega\overline{\rho}\mathbf{u} = -\nabla P' + \mathbf{g}\rho' w \ , \qquad i\omega\rho' + \frac{d\overline{\rho}}{dz}w = 0 \ , \tag{4.10}$$

yields the governing equation (see, e.g., *Yih* [1980], Ch. 2, § 15)

$$\overline{\rho}^{-1}\nabla \cdot (\overline{\rho}\nabla\psi) - \frac{N^2}{\omega^2}\frac{\partial^2\psi}{\partial x^2} = 0 \ , \tag{4.11}$$

where $\nabla = (\partial/\partial x, \partial/\partial z)$ and $\overline{\rho}(z)$ is the mean density (related to the hydrostatic pressure, $\partial\overline{P}/\partial z = g\overline{\rho}$). Using the rigid lid approximation $w(x,0) = 0$ the no-flux boundary condition on $\mathbf{u}$ gives

$$\mathbf{n} \cdot \mathbf{u}|_\partial = \frac{\partial\psi}{\partial s}(s) = 0 \quad \rightarrow \quad \psi|_\partial = 0 \ , \tag{4.12}$$

where $\mathbf{n} = (n_x, n_z)$ is the boundary unit normal. Analytical solutions to (4.11) and (4.12) are only possible for a few simple configurations of stratification and bathymetry; models with irregular bathymetry and non-uniform stratification must be solved numerically. When discretized, the (4.11)/(4.12) system can be written as a matrix eigenvalue problem

$$\mathbf{M}\Psi = \omega^2\Psi \ .$$

Solution of this equation yields a finite number of internal seiche eigensolutions Ψ and their corresponding frequencies. (Note, however, that solutions can only be obtained for systems which are not subject to wave ray focusing; see *Maas and Lam* [1995]). For a detailed discussion of the numerical method see *Fricker and Nepf* [2000a].

4.3 The Upper Mystic Lake

As a test case, we evaluate decay rates for the dominant seiches in the Upper Mystic Lake (UML; Winchester, MA). The Mystic Lake system, comprised of the Upper and Lower lakes plus two shallow forebays, is the focal point of the surface and ground water flows exiting the Aberjona

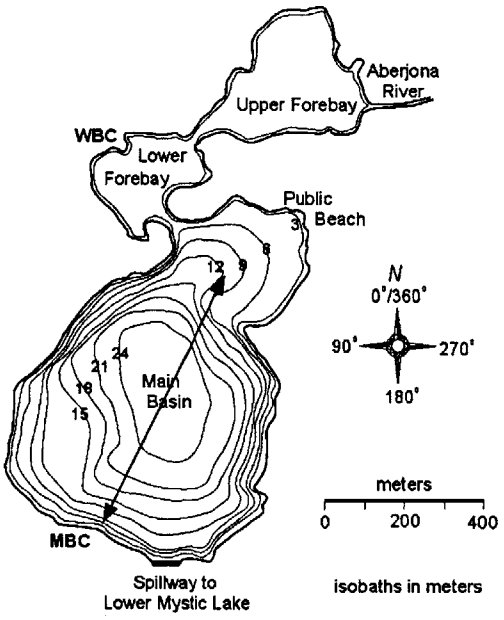

Figure 4-2: The Upper Mystic Lake, Winchester, Massachusetts.

Watershed (Boston, MA). Internal seiches in the UML have been measured for several summers as part of an ongoing investigation of contaminant transport in the Aberjona and Mystic Lake systems. The UML is a small dimictic lake, $\sim$ 1 km long, 600 m wide, and 25 m deep (Figure 4-2), with bathymetry consisting of a main basin plus a shallow lobe (maximum depth $\sim$9 m) covering the northern third of the lake (Figure 4-3). Summer stratification conditions are extremely consistent each year; the epilimnion grows to a maximum depth of 5 meters and reaches $\sim$ 28°C, while the hypolimnion remains at $\sim$ 6°C. The location of the pycnocline relative to the shoal has a major impact on the structure of seiches in the UML, generating substantially magnified seiche-induced bed velocities in this region [*Fricker and Nepf*, 2000a]. The objective of the present study is to assess the impact of stratification and bathymetry on the viscous damping of the seiches, and relate the observations to predicted decay rates (4.9).

4.3.1 Internal wave and wind data

Three thermistor chains were deployed in the UML to record the internal wave activity during the 1996 summer field season (April to November). The horizontal positions of the chains,

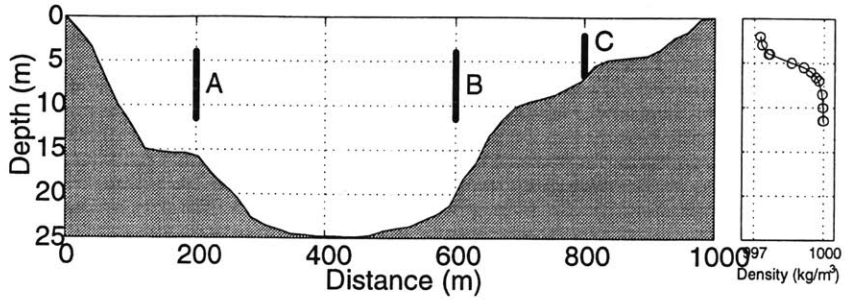

Figure 4-3: Bathymetry of the UML along the dominant wind forcing axis.

marked A, B, C, are shown in Figure 4-3. Each system was comprised of six thermistors and a pressure sensor to determine depth. The thermistors on chains A and B (main basin) were spaced at 1.5 m intervals, with the top thermistor deployed approximately 4 m below the surface. This arrangement was chosen to optimally span the pycnocline for typical mid-summer stratification conditions in the UML. In the shallower northern part of the lake chain C was placed 2 m below the surface with thermistors 1.0 m apart. Temperatures were recorded at five minute intervals. Concurrent measurements of wind speed and direction were made at 10-minute intervals using an anemometer at the southern end of the lake, placed approximately 12 m above the water surface on a flag pole at the Medford Boat Club (MBC, Figure 4-2). Winds in the Mystic Lake system are consistently from the south during summer and the north in winter, because of both the local geography and weather patterns. The forcing is therefore predominantly along the major axis of the UML all year (indicated by an arrow in Figure 4-2).

A sample of internal wave data at chain C is presented in Figure 4-4 for a one-week period during mid-summer (1996). Wind data for the same period are also shown. The temperature data show that the seiche climate in the UML is unsteady, and that the system undergoes rapid transition among modes. For example, beginning roughly on Jday 193 the dominant mode is the ~12-hour oscillation clearly evident in the fourth thermistor record (5m depth, ~18°C). This seiche persists through Jday 197. At the end of Jday 195 we see the onset of a shorter-period seiche (~2h) in the fifth thermistor record (6m, ~13°C) which appears to be forced by a short, strong wind event, and is damped over 5-10 periods (and is possibly re-excited by the weaker wind event at 0:00h on Jday 196).

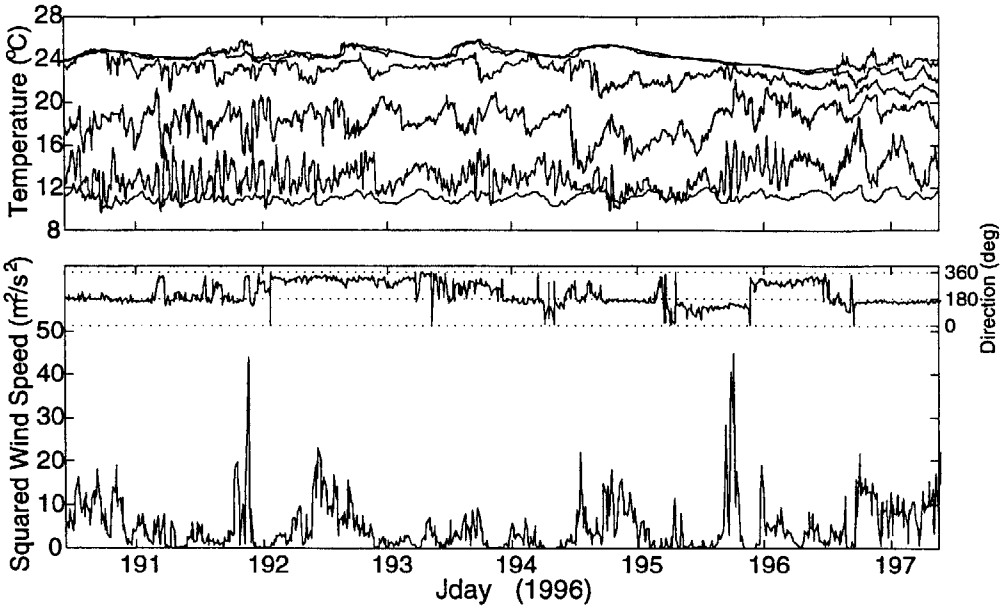

Figure 4-4: Internal wave data from thermistor chain C, with concurrent wind data.

Figure 4-5 shows a spectrogram of the temperature data at thermistor 5 (chain C), computed for a three-week period which includes the data in Figure 4-4. The wind data are also presented. The spectrogram shows distinct oscillations at ~ 0.6 cph and $0.1 - 0.2$ cph, and again reveals the transient nature of the seiche response in the UML. Comparing the wind and wave data, the 0.6 cph oscillation appears to be forced by stronger, short-duration winds (for example, the events at Jday 189, 192, 196, and 202, which are marked by dashed lines). The persistence of the lower-frequency mode might suggest that this oscillation is matched by a component of the wind spectrum. However, as discussed Section 4.3.3, this is unlikely.

4.3.2 Viscosity and δ

Recall that, in order to compute an expression for α, we described the shear stresses near the bed using a viscosity parameterization (4.4). Unfortunately, very little information is available regarding viscosities or diffusivities in lake benthic boundary layers, or even about the size of the BL. *Hagatun and Eidsvik* [1986] computed a time- and space-dependent turbulent eddy viscosity for the benthic BL under ocean surface waves (period $\sim$ 10s), using a numerical model

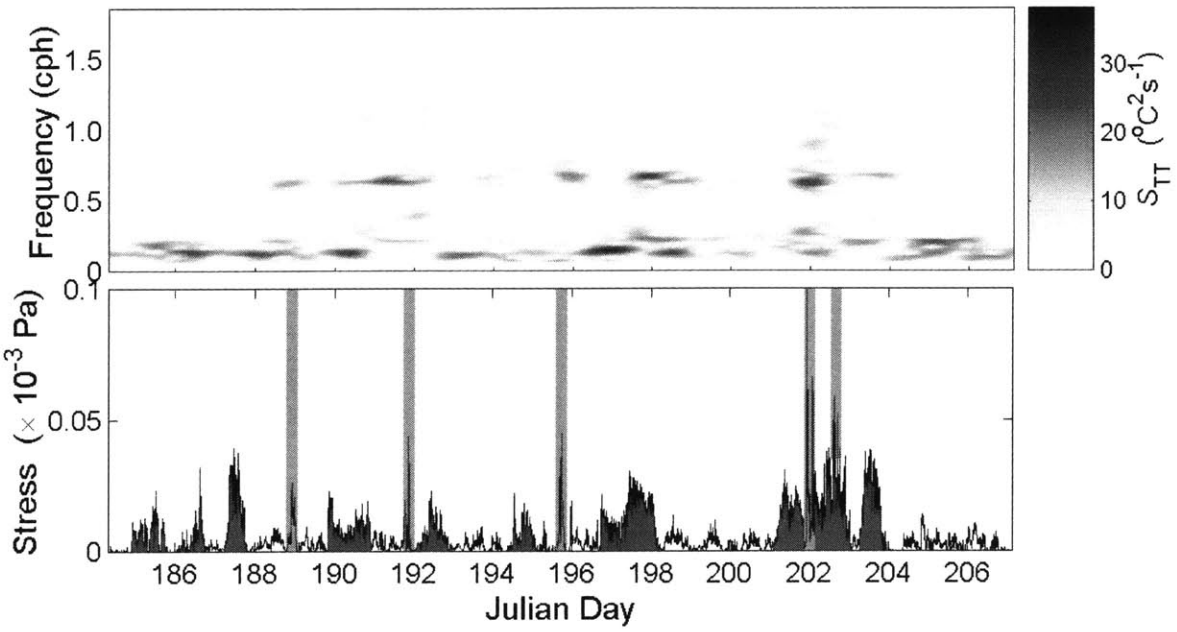

Figure 4-5: Spectrogram of temperature data collected at thermistor chain C (fifth thermistor, at depth 6m). Frequencies are reported in cycles per hour (cph). The bottom figure shows the concurrent wind data.

with $k - \varepsilon$ closure. Over a wave period they found $\nu_t \sim 10^{-4}\frac{U^2}{\omega}$, with U the magnitude of the free-stream velocity just above the BL. Applying this to the much longer-period seiches in the UML, using the frequency of the dominant V3H1 mode ($\omega \approx 2 \times 10^{-4}\mathrm{s}^{-1}$) and estimating the outer flow velocity as $\mathcal{O}(1\ \mathrm{cm/s})$, we find $\nu_t \sim 5 \times 10^{-5}\mathrm{m}^2/\mathrm{s}$ and $\delta = \sqrt{2\nu/\omega} \sim 0.7\mathrm{m}$. *Hagatun and Eidsvik* [1986] also estimated the thickness of the BL as the height above the bed where the velocity reached U (and where $\tau = 0$). They observed a maximum $\delta \sim 5 \times 10^{-2}\frac{U}{\omega}$ during the wave period. This formula yields $\delta \sim 2.5\mathrm{m}$ for the UML.

More recently, *Gloor et al.* [2000] measured $\nu \sim 3 \times 10^{-5}\mathrm{m}^2/\mathrm{s}$ in the near-bed waters in Lake Alpnach (see also *Wüest and Gloor* [1998]), a surprisingly similar result to *Hagatun and Eidsvik* [1986]. The similarities between the UML and Lake Alpnach (both are small lakes, with depths of 25m and 35m, respectively) allow much more confidence that $\nu \gtrsim 10^{-5}\mathrm{m}^2/\mathrm{s}$ is a good estimate of BL viscosities in the UML. *Gloor et al.* [2000] also observed temporal evolution (both oscillatory and unsteady) and spatial variations in boundary mixed-layer thickness (δ_{ML}),

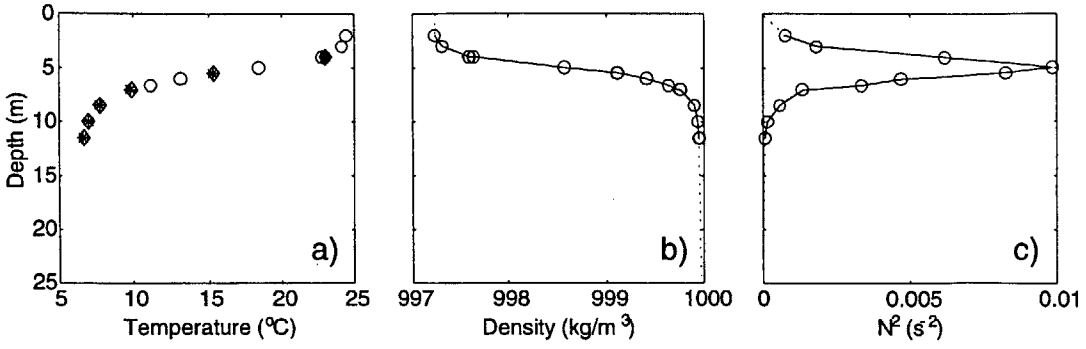

Figure 4-6: Mean temperature, density, and N^2 profiles for Jday 190-197.

which was inferred from temperature microprofile data as the height above the bed where the temperature gradient dT/dz showed a discontinuity. They estimated δ_{ML} in the range $0-5$m (inversely correlated with buoyancy), with $\delta_{ML}=1$m a representative value. We discuss these observations in more detail below. To compute decay rates for the seiches in the UML in the following section we use a BL thickness of $\delta=1$m.

4.3.3 Seiches in the UML

To evaluate internal seiche solutions for the UML, a representative mid-summer density (or buoyancy frequency) profile is computed using the thermistor chain data in Figure 4-4 (chain C) and the simultaneous data at chains A and B. The temperature at each of the 18 thermistors is first averaged, and then assembled in a composite profile which is used to estimate $\overline{\rho}(z)$ and $N^2(z)$ (Figure 4-6). The UML is modeled using idealizations of N^2 and the bathymetry $h(x)$ along the wind forcing axis (Figure 4-3). Model stream function solutions for the V1H1, V2H1, and V3H1 seiches modes are shown in Figure 4-7. The $\psi(x,z)$ are computed on a 40×40 grid and then interpolated over a finer grid (150 horizontal $\times$ 100 vertical) to facilitate the evaluation of $\mathbf{u}_{bed}$ (see *Fricker and Nepf* [2000a]). As an illustration of the velocity field computed from these solutions, $\mathbf{u}(x,z)$ for the V1H1 mode is shown in Figure 4-8 (20×20). This plot represents the spatial envelope of the sinusoidal standing wave motion.

The computed V1H1 frequency (0.58 cph) matches the higher-frequency oscillation in the spectrogram (Figure 4-5), identifying this mode as the V1H1 seiche (in general, this peak

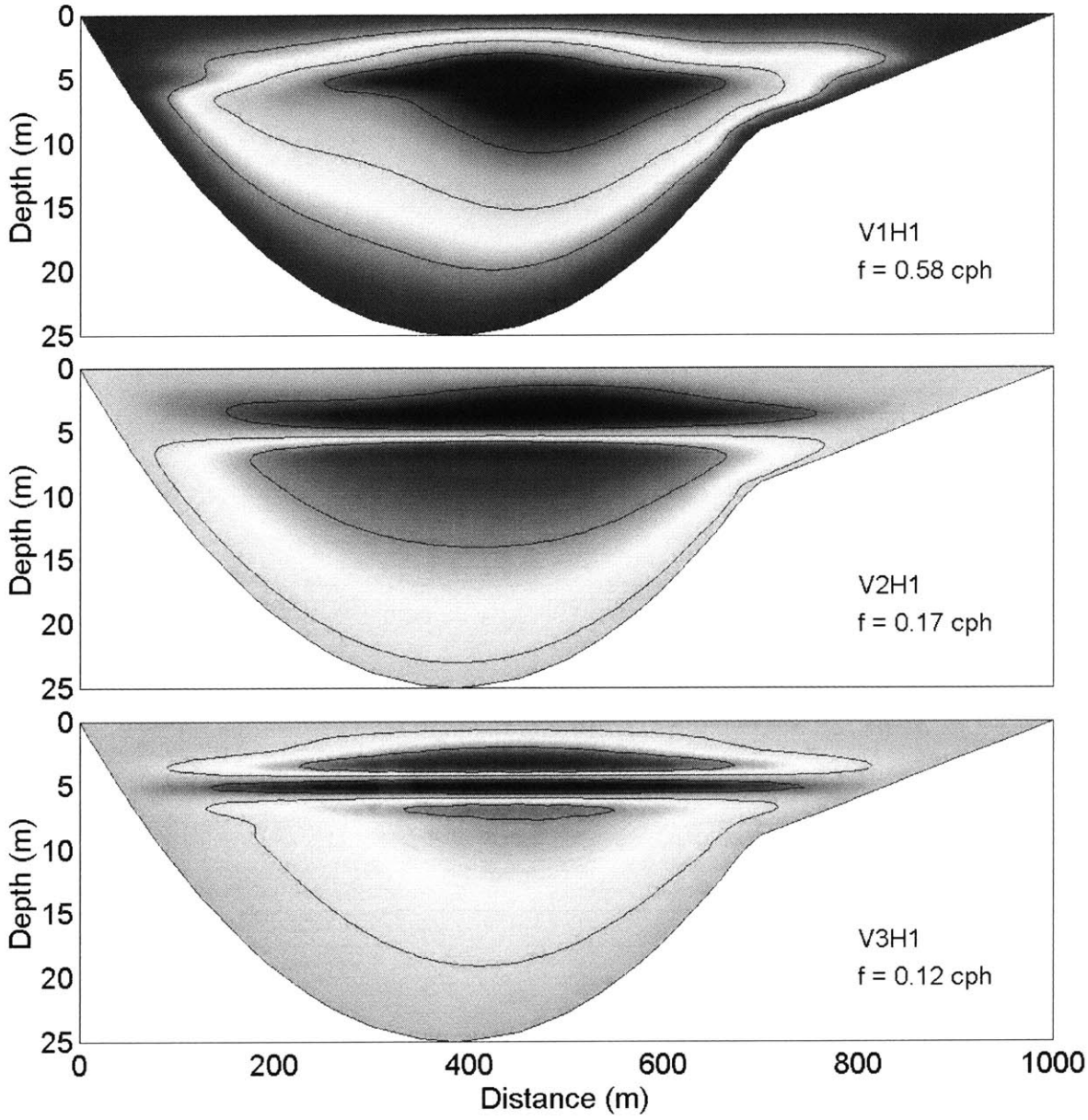

Figure 4-7: Streamfunction contours for the dominant modes in the Upper Mystic Lake (VnH1, n = 1,2,3).

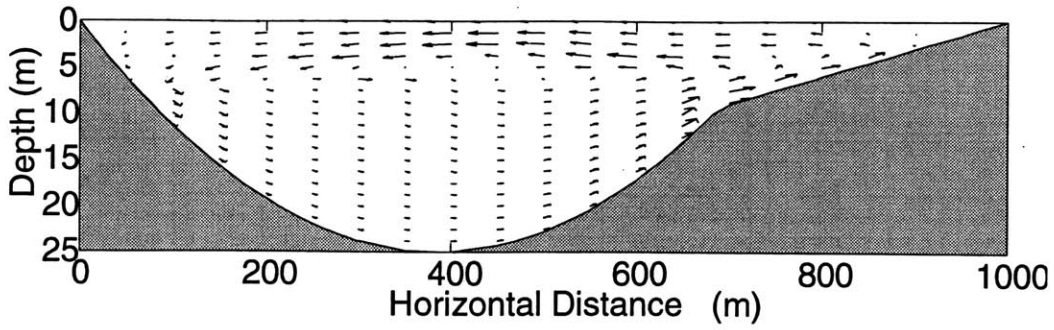

Figure 4-8: Velocity field computed from the V1H1 stream function contours in Figure 4-7.

appears at 0.55 – 0.65 cph in the wave spectra, depending on season). From the V2H1 (0.17 cph) and V3H1 (0.12 cph) numerical results we see that the lower, broader band in the spectrogram corresponds to these two seiches. The two oscillations are often difficult to identify separately, but can be clearly seen in Figure 4-5 at Jday 198, for example. Spectral analysis of UML thermistor data shows an oscillation centered at $\sim$ 0.08 cph throughout the summer; even though this peak is usually broad, by using a larger bin size (i.e. $>$ 512 points) the analysis is capable of distinguishing a separate peak at $\sim$ 0.2 cph whenever the higher-frequency mode is present. Despite this, the presence (in fact, dominance) of the V3 mode in the UML was not appreciated before the results of this study, because V3 spatial phase structure was not distinguishable from V2 motion in earlier thermistor chain records due to the positioning of the thermistors in previous years [*Fricker and Nepf*, 2000; *Trowbridge*, 1995]. In addition, the overly simplistic models used in previous studies were unable to precisely resolve the V2 and V3 frequencies [*Trowbridge*, 1995], and thus the existence of the V3 mode was not anticipated.

A sample of temperature data from chain A (southern end of the main basin) is presented in Figure 4-9. The in-phase motion at the first and third thermistors and antiphase motion at the second is clearly evident in the record. The thermistors at this location are spaced 1.5 m apart; the V3 motion is therefore confined to a small region of the water column, which generally makes it difficult to detect the presence of the V3H1 mode. As mentioned above, this mode is the dominant oscillation in the UML, with a spectral amplitude one order of magnitude larger than the V1H1. Whether or how this mode is preferentially excited is unclear. Numerous studies have shown that higher vertical modes (particularly V2H1) are often dominant in small lakes,

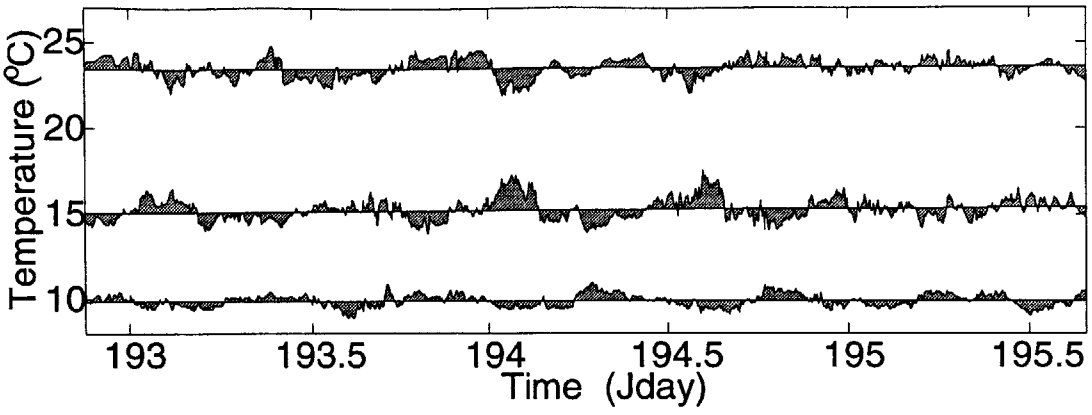

Figure 4-9: Thermistor chain data at chain A, showing V3 phase structure.

usually because the seiche frequency matches a component of the wind spectrum [*Münnich et al.*, 1992; *Wiegand and Chamberlain*, 1987; *LaZerte*, 1980). However, in the Mystic Lake system the wind forcing shows no particular periodicity, except for a weak diurnal peak in the wind spectrum (~ 0.04 cph). We therefore conclude that the seiche climate in the UML is predominantly determined by other factors, such as bathymetry, stratification, and as discussed in the next section, by the viscous damping rate of each seiche.

4.4 Results and discussion

Using equation (4.9) the decay rates for the dominant seiches in the UML are computed from the numerical solutions in Figure 4-7. The results are shown in Table 4.1. Comparing α with $\alpha_{|\eta|=1}$, the buoyancy and bathymetry effects accounted for by η cause the decay rates to increase by approximately one order of magnitude. The decay rate for the V1H1 mode in particular is exceptionally large; $\alpha/\omega \approx 0.05$ implies that the wave amplitude decays by $\sim$80% over five wave periods, i.e. $A\,(5\mathrm{T})\,/A_0 \approx 0.2$. This is much closer to the observed behavior of the V1H1 seiche than predicted by $\alpha_{|\eta|=1}$, for which $A/A_0 = 0.2$ at $t \approx 36\mathrm{T}$. By fitting an exponentially-decaying sinusoid to the V1H1 response which is excited on Jday 195.7 (see Figure 4-4), we estimate a V1H1 decay rate of $\alpha/\omega \sim 0.35 \pm 0.05$, in good agreement with the model prediction.

While the V3H1 decay rate is increased by more than an order of magnitude, α_{V3H1} is still

sufficiently small that this mode can persist in the UML. The dominance of this seiche is clearly evident in the field data, for example in Figure 4-4, in which the ~10hr V3H1 oscillation can be seen throughout most of the seven-day record in both the ~18°C and bottom thermistors (which was lying on the bed). The results in Table 4.1 show that α decreases for progressively higher vertical modes. Interestingly, field studies of dominant higher vertical modes often report that the V1H1 is excited by strong winds along with the other seiches, but then rapidly decays, leaving the more persistent higher modes (usually V2H1; see *Wiegand and Chamberlain* [1987]; *LaZerte* [1980]). These observations suggest that $\alpha \downarrow$ for $n \uparrow$ is a common result. The fact that the same trend is observed for $\alpha_{|\eta|=1}$ in Table 4.1 implies that this behavior is primarily due to features of the (bed) velocity field, and not $|\eta|$. A likely explanation is that the fraction of total seiche energy which is located at the bed (or, in terms of velocities, $|u_{\text{bed}}| / \sqrt{2E/\rho_0}$) decreases for higher vertical modes.

Recall from 4.8 that the shear at the bed is

$$\left.\frac{\partial \mathbf{q}}{\partial x_n}\right|_{bed} = (1+\phi i)\left.\frac{\mathbf{u}}{\delta'}\right|_{\partial} \quad .$$

In the UML, the region of the water column where the density gradient is strongest (where N is a maximum, and δ' a minimum) coincides roughly with the depth of the northern shoal (see Figure 4-3). The bathymetry at this location also tends to generate substantially magnified bed velocities, as the numerical V1H1 solution in Figure 4-8 shows. The increased decay rate for the V1H1 seiche (in fact all the seiches) is therefore due to the combined effect of enhanced u_{bed} and $|\eta| \gg 1$, which generate substantially magnified bed stresses. Recent studies have explored the role of bathymetry and stratification in determining seiche structure [*Münnich*, 1996; *Maas and Lam*, 1995], and bed velocities in particular [*Fricker and Nepf*, 2000a]. The results in Table 4.1 reveal that the dependence of α on $h(x)$ and $\overline{\rho}(z)$ is governed both by u_{bed} and by additional buoyancy and bathymetry effects accounted for in the factor η.

Although the relationship between δ' and the physical benthic BL thickness (δ_{BL}) is unclear, it is interesting to note that the dependence of δ' on buoyancy described above resembles observations by *Gloor et al.* [2000]. In field studies in Lake Alpnach these authors found an inverse relationship between δ_{ML} and the local buoyancy frequency (Figure 4-10). Their

mode	$\alpha_{\lvert\eta\rvert=1}/\omega$	α/ω	$\alpha_{\text{obs}}/\omega$
V1H1	0.0071	0.049	0.035 ± 0.005
V2H1	0.0021	0.022	-
V3H1	0.0009	0.012	-

Table 4.1: Decay coefficients for the dominant UML seiches. The first column shows the decay rate when buoyancy effects are neglected. The V1H1 decay rate estimated from the wind-induced event at Jday 195.7 is listed in the third column

study also showed that δ_{ML} varies substantially over time, and is determined by numerous physical processes, most of which are still poorly understood. It is therefore not possible to say conclusively that the behavior of δ' explains the observations by *Gloor et al.* in Lake Alpnach. However, the fact that both δ' and the observed δ_{ML} are inversely related to buoyancy suggests that the modified Stokes flow model (4.7) does adequately describe at least part of the physics of the benthic BL. This was recently reinforced by direct observations of near-bed velocity profiles in Lake Alpnach which resemble the Stokes solution (*Wüest*, pers. comm.).

Finally, we note that several temperature microprofile studies have revealed that, at some times and locations, the temperature gradient inside lake benthic BLs can be as much as one order of magnitude smaller than in the fluid just above the BL (in fact, this is one way of estimating δ_{ML} from field data [see *Gloor et al.*, 2000; *Lemckert and Imberger*, 1998; *Gloor et al.*, 1994]). Because of this homogenization of fluid, the assumption that the mean stratification $\overline{\rho}(z)$ (and $N^2(z)$) away from the bed can be extended into the BL might not be universally valid. The homogenization of fluid diminishes density gradients near the bed, and hence reduces the value of α. In addition, benthic mixing causes fluid to advect out of the BL in horizontal buoyancy-driven intrusions, further changing the BL structure [see, e.g., *Gloor et al.*, 2000; *Goudsmit et al.*, 1997]. As mentioned previously, none of these processes is well understood at the present time, and thus it is difficult to know how the expression for α in (4.9) should be modified. However, since unsteady effects, fluid homogenization, and other physical processes can potentially be of importance, the α computed here likely represents an upper limit on the seiche decay rate.

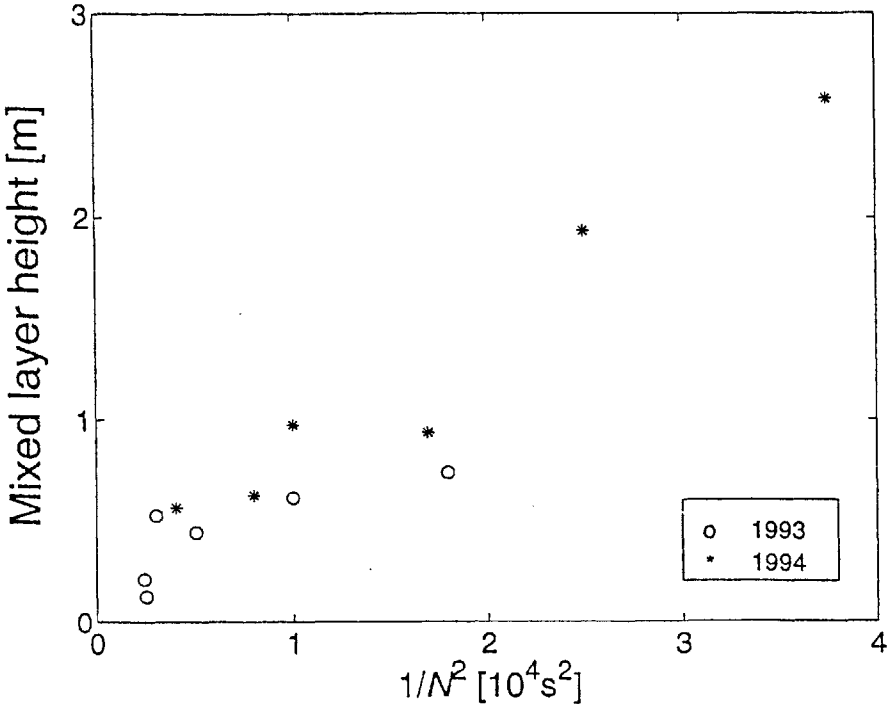

Figure 4-10: Boundary layer thickness versus buoyancy frequency, from observations in Lake Alpnach (reproduced from *Gloor et al.*, 2000 (Figure 10); © American Geophysical Union).

4.5 Conclusions

The decay rate α for internal seiches is computed as the rate of bed stress working (4.2), and is equivalent in form to the integral of kinetic energy at the bed modified by a buoyancy/bathymetry factor

$$|\eta| = \left|1 - \frac{N^2}{\omega^2}\sin^2\theta_{bed}\right|^{\frac{1}{2}} \quad ; \tag{4.13}$$

equation (4.2). Buoyancy and bathymetry effects cause roughly a tenfold increase in α (versus $\alpha_{|\eta|=1}$) for the dominant seiches in the Upper Mystic Lake (VnH1, n = 1,2,3). This magnification is caused largely by enhanced bed velocities over a shoal whose depth coincides with the pycnocline (i.e. where N^2 is large). In addition, the damping rate decreases by a factor of ~ 2 for progressively higher vertical modes. This is likely due to the decrease in relative energy at the bed for higher modes. These trends help explain both the rapid decay of the V1H1 and the persistence of the V3H1 seiches observed in the UML thermistor chain data.

The velocity field in the benthic boundary layer is modeled as a modified form of Stokes' solution for an oscillating flow over a flat plate, in which the outer flow drops to zero at the bed over the distance $\delta' = \delta/|\eta|$ ($\delta = \sqrt{2\nu/\omega}$, with ν the viscosity). The magnification of α described above can be attributed to increased bed shear $\sim \mathbf{u}|_{bed}/\delta'$ within the pycnocline due to the buoyancy and bathymetry effects described by $|\eta|$. We therefore describe δ' as the shear length, making the distinction between this parameter and the physical (i.e., observed) boundary- or mixed-layer thickness δ_{ML}. Within the pycnocline we approximate (see (4.13))

$$\delta' \approx \delta \frac{\omega}{N \sin\theta_{bed}} \ , \tag{4.14}$$

and thus the shear length shows the same inverse relationship with buoyancy that *Gloor et al.* [2000] observed for the mixed-layer height (δ_{ML}) in Lake Alpnach. The similarity between these observations and the behavior predicted in (4.14), as well as the measurement of Stokes-like bed velocity profiles in Lake Alpnach (Wüest, pers. comm.), is strong evidence of the validity of the modified-Stokes BL model, and the decay rate expression in (4.9).

Bibliography

[1] Cacchione, D. A. and J. B. Southard, 1974. Incipient sediment movement by shoaling internal gravity waves. *J. Geophys. Res.*, **79**(15): 2237–2242.

[2] Cacchione, D. and C. Wunsch, 1974. Experimental study of internal waves over a slope. *J. Fluid Mech.*, **66**(2): 223–239.

[3] Craig, P. D., 1991. Incorporation of damping into internal wave models. *Cont. Shelf Res.*, **11**(6): 563-577.

[4] De Silva, I. P. D., J. Imberger, and G. N. Ivey, 1997. Localized mixing due to a breaking internal wave ray at a sloping bed. *J. Fluid Mech.*, **350**: 1–27.

[5] Dore, B. D., 1968a. Oscillations in a non-homogeneous viscous fluid. *Tellus*, **20**: 514-523.

[6] Dore, B. D., 1968b. Viscous damping effects in long waves on the rotating earth. *Quart. J. Mech. and Appl. Math.*, **21**: 105-114.

[7] Dore, B. D., 1969. The decay of oscillations of a non-homogeneous fluid within a container. *Proc. Camb. Phil. Soc.*, **65**: 301-307.

[8] Fischer, H. B., J. E. List, R. C. Y. Koh, J. Imberger, and N. H. Brooks, 1979. Mixing in Inland and Coastal Waters. Academic Press, New York.

[9] Fricker, P. D., and H. M. Nepf, 2000a. Bathymetry, stratification, and internal seiche structure. *J. Geophys. Res.*, **105**(C6): zzz-zzz.

[10] Fricker, P. D., and H. M. Nepf, 2000b. Viscous decay of internal seiches. In preparation.

[11] Gloor, M., A. Wüest, and M. Münnich, 1994. Benthic boundary mixing and resuspension induced by internal seiches. *Hydrobiologia,* **284**: 59-68.

[12] Gloor, M., A. Wüest, and D. M. Imboden, 2000. Dynamics of mixed bottom boundary layers and its implications for diapycnal transport in a stratified, natural water basin. *J. Geophys. Res.,* **105**(C4): 8629-8646.

[13] Goudsmit, G.-H., F. Peeters, M. Gloor, A. Wüest, 1997. Boundary versus internal diapycnal mixing in stratified natural waters. *J. Geophys. Res.,* **102**(C13): 27,903-27,914.

[14] Hagatun, K. and K. J. Eidsvik, 1986. Oscillating turbulent boundary layer with suspended sediments. *J. Geophys. Res.,* **91**(C11): 13,045-13,055.

[15] Henderson, D. M., and J. W. Miles, 1994. Surface-wave damping in a circular cylinder with a fixed contact line. *J. Fluid Mech.*, **275**: 285-299.

[16] Howell, D. R., B. Buhrow, T. Heath, C. McKenna, W. Hwang, and M.F. Schatz, 2000. Measurements of surface-wave damping in a container. *Physics of Fluids*, **12**(2): 322-326.

[17] Hukuda, H., 1986. On the damping of gravity oscillations in closed basins. *Dyn. Atmos. Oceans* **10**: 97-109.

[18] Johns, B., 1968. A boundary layer method for the determination of the viscous damping of small amplitude gravity waves. *Quart. J. Mech. and Appl. Math.*, **21**: 93-103.

[19] Kerswell, R. R., and C. F. Barenghi, 1995. On the viscous decay rates of inertial waves in a rotating circular cylinder. *J. Fluid Mech.*, **285**: 203-214.

[20] LaZerte, B. D., 1980. The dominant higher order vertical modes of the internal seiche in a small lake. *Limnol. Oceanog.*, **25**(5): 846-854.

[21] Lemckert, C., and J. Imberger, 1998. Turbulent benthic boundary layer mixing events in fresh water lakes. In: Physical Processes in Lakes. Coastal and Estuarine Studies Volume 54, pages 503-516. J. Imberger, Editor.

[22] Maas, L. R. M., and F.-P. A. Lam, 1995. Geometric focusing of internal waves. *J. Fluid Mech.*, **300**: 1-41.

[23] Martel, C., J. A. Nicolás, and J. M. Vega, 1998. Surface-wave damping in a brimful circular cylinder. *J. Fluid Mech.*, **360**: 213-228.

[24] Mei, C. C., and P. L.-F. Liu, 1973. The damping of surface gravity waves in a bounded liquid. *J. Fluid Mech.*, **59**: 239-256.

[25] Miles, J. W., and D. M. Henderson, 1998. A note on interior vs. boundary-layer damping of surface waves in a circular cylinder. *J. Fluid Mech.*, **364**: 319-323.

[26] Münnich, M., 1996. Influence of bottom topography on internal seiches in stratified media. *Dyn. Atmos. and Oceans*, **23**: 257-266.

[27] Münnich, M., A. Wüest, and D. M. Imboden, 1992. Observations of the second vertical mode of the internal seiche in an alpine lake. *Limnol. Oceanog.*, **37**(8): 1705-1719.

[28] Orlić, M., 1984. The influence of bottom friction on transverse internal seiches in rotating rectangular channels. *Arch. Met. Geophy. Biocl.*, Ser. A 33: 175-185.

[29] Solo-Gabriele, H, 1995. Metal Transport in the Aberjona River System: Monitoring, Modeling, and Mechanisms. Ph.D. Thesis, MIT.

[30] Spliethoff, H. M., and H. F. Hemond, 1996. History of toxic metal discharge to surface waters of the Aberjona Watershed. *Env. Sci. and Tech.*, **30**(1): 121-128.

[31] Trowbridge, P. R., 1995. Rapid Redox Transformations of Arsenic and the Characterization of the Internal Seiches in the Upper Mystic Lake, Medford, Massachusetts. M.S. Thesis, MIT.

[32] Wiegand, R. C. and V. Chamberlain, 1987. Internal waves of the second vertical mode in a stratified lake. *Limnol. Oceanog.*, **32**(1): 29-42.

[33] Wüest, A. and M. Gloor, 1998. Bottom boundary mixing: The role of near-sediment density stratification. In: Physical Processes in Lakes. Coastal and Estuarine Studies Volume 54, pages 485-502. J. Imberger, Editor.

[34] Wunsch, C., 1969. Progressive internal waves on slopes. *J. Fluid Mech.*, **35**: 131–144.

[35] Yih, C.-S., 1980. Stratified Flows. Academic Press, New York.

Appendix A

List of Symbols

B	Lake width
E, E_n, E_{mn}	Total seiche energy (mode n, mn)
E_{kin}, E_{pot}	Seiche kinetic, potential energy
H	Lake depth (scale)
L	Lake length (scale)
$\mathbf{M}$	BL equation matrix operator
N	Buoyancy frequency
$P(x,z,t)$	Dynamic pressure
$\overline{P}(z)$	Mean pressure (hydrostatic)
$\mathbf{R}, \mathbf{R}'$	BL vertical projection matrices
$\mathbf{T} = (\mathbf{t}_1, \mathbf{t}_2)$	BL transverse unit vectors
$\mathbf{U} = U, V, W$	BL velocities (in the $(\mathbf{i}, \mathbf{j}, \mathbf{k})$ basis)
U_n	BL normal velocity
$\mathbf{U}_T = (U_{t_1}, U_{t_2})$	BL transverse velocities
V, dV	Volume, volume element
V_{BL}	Volume of BL
g	Gravitational acceleration
$h(x), h(x,y)$	Lake bathymetry (2D, 3D)

h_1, h_2	Layer thicknesses (2-layer formulation)
$\mathbf{i}, \mathbf{j}, \mathbf{k}$	Unit vectors (Cartesian, absolute basis)
k, k_m	Horizontal wavenumber (mode m)
$m_x, m_y, m_z;\ m, n;\ n_h, n_v$	Mode numbers (x, y, z; horizontal, vertical)
$\mathbf{n}, n_x$	Boundary unit normal vector ($x-$component)
$p_i = \mathbf{t}_i \cdot \mathbf{k} \quad (i = 1, 2)$	Tangent vector vertical projections
$\mathbf{q}, q_i \quad (= \mathbf{u} + \mathbf{U})$	Total fluid velocity field
$s, \mathbf{s}$	Boundary coordinate(s)
t	Time
$\mathbf{u} = (u, v, w)\,,\ \mathbf{u_0},\ etc.$	Inviscid fluid velocity field
$\mathbf{x} = (x, y, z)$	Spatial coordinates (absolute basis)
$x_n = \mathbf{n} \cdot \mathbf{x}$	Boundary normal coordinate
$\mathbf{x}_T = \mathbf{T} \cdot \mathbf{x} = (\mathbf{x}_{t_1}, \mathbf{x}_{t_2})$	Boundary tangential coordinates
$\triangle\rho$	Density difference (surface-bed, or 2-layer)
Ω	Lake volume
α	Seiche amplitude decay rate
$\delta,\ \delta(s)\,,\ \delta(\mathbf{s})$	BL thickness
$\delta' \quad (= \delta/\lvert\eta\rvert)$	Shear length
$\delta(x - x_0)\,;\ \delta_{ab}$	Dirac delta function; Kronecker delta
$\varepsilon \quad (= \delta/H)$	Perturbation parameter
$\zeta(\mathbf{x}, t)\,, \xi(\mathbf{x}, t)$	Dynamic horizontal, vertical fluid displacements
$\eta(s)\,, \eta(\mathbf{s})$	BL buoyancy coefficient
$\theta \quad (= \text{sign}(\eta^2))$	BL phase coefficient
μ	Aspect ratio $(= H/L)$
ν	Kinematic viscosity
$\xi_n, \xi_{t_1}, \xi_{t_2}$	Scaled (dimensionless) BL coordinates
$\rho(\mathbf{x}, t) \quad (= \rho'(\mathbf{x}, t))$	Dynamic density (isopycnal) fluctuations

$\overline{\rho}(z)$	Mean density
$\rho_0; \rho_s, \rho_1, \rho_2$	Density scale; surface, layer densities
$\sigma(\mathbf{s}), \sigma(s)$	Scaled BL viscosity $(= \nu(s)/\nu_{\max})$
$\tau, \tau_{ij}; \tau_s$	Stress; surface stress
$\phi(z), \phi_n(z)$	Vertical structure function (mode n)
$\chi(z), \chi_n(z)$	Vertical structure function (mode n)
$\psi(x,z), \psi_n(x,z), \psi_{mn}(x,z)$	Streamfunction (mode n, mn)
$\psi_0(x,z), \psi_1(x,z), ..$	Streamfunction (perturbation expansion)
$\omega, \omega_n, \omega_{mn}$	Seiche frequency (mode n, mn)
$\omega_0, \omega_1, ..$	Seiche frequency (perturbation expansion)
$\mathcal{H}(z - z_0)$	Heaviside function
$\mathcal{L}$	Linear differential operator
∂	Lake boundary (bed plus free surface)
∂_c	Core/BL interface

Appendix B

Governing equations

We begin with a scaling analysis of the momentum (i.e. inviscid Navier-Stokes) and continuity equations for a stratified fluid. Benney (1966) performed the same analysis in a study of long, finite amplitude surface and internal waves, in a paper which is regarded as a seminal work in the application of the KdV equation to internal waves. The development here differs somewhat from Benney (1966) by introducing additional scaling parameters.

The Navier-Stokes (Euler) equations, excluding viscous and Coriolis terms, are

$$\rho\frac{\partial \mathbf{u}}{\partial t} + \rho\mathbf{u}\cdot\boldsymbol{\nabla}\mathbf{u} = -\boldsymbol{\nabla}P - \rho g\mathbf{k} \ , \tag{B.1}$$

with, for example $\mathbf{u}(\mathbf{x},t) = (u,v,w)$ and $\boldsymbol{\nabla} = (\partial/\partial dx, \partial/\partial dy, \partial/\partial dz)$ in Cartesian coordinates. For an incompressible fluid we have the continuity relations

$$\boldsymbol{\nabla}\cdot\mathbf{u} = 0 \ , \qquad \frac{D\rho}{Dt} = \frac{\partial\rho}{\partial t} + \mathbf{u}\cdot\boldsymbol{\nabla}\rho = 0 \ . \tag{B.2}$$

The various fields and coordinates in these equations are scaled as follows:

$$\begin{array}{lll} (x,y) \rightarrow L(x,y) & (u,v) \rightarrow U(u,v) & P \rightarrow \rho_0 g H P \\ z \rightarrow Hz & w \rightarrow Ww & \rho \rightarrow \rho_0\rho \\ t \rightarrow Tt & & \end{array} \tag{B.3}$$

For basin-scale waves the length scales H and L are defined by the depth and length of the lake, respectively. Since we are seeking standing wave (and hence oscillatory) solutions, the timescale T can be taken as ω^{-1}, with ω the oscillation period of a given internal seiche mode. Furthermore it can be assumed that the mean flow in the system is zero, so that the velocities u, v, w correspond explicitly to the seiche motion. The pressure and density fields, on the other hand, can be decomposed into mean and perturbation terms,

$$P(\mathbf{x},t) \rightarrow \overline{P}(z) + \alpha P'(\mathbf{x},t) \qquad \rho(\mathbf{x},t) \rightarrow \overline{\rho}(z) + \alpha\rho'(\mathbf{x},t) \ ,$$

where α is a small dimensionless parameter related to the 'wave amplitude' (or equivalently to the magnitude of the velocities). Note the subtle but important point that

$$\frac{\partial\rho}{\partial z} \rightsquigarrow \frac{\triangle\rho}{H}\frac{d\overline{\rho}}{dz} + \alpha\frac{\rho_0}{H}\frac{\partial\rho'}{\partial z} \qquad \frac{\partial\rho}{\partial t} \rightsquigarrow \alpha\frac{\rho_0}{T}\frac{\partial\rho'}{\partial t} \ ,$$

where $\triangle\rho$ scales on the surface-to-bed density difference.

Using the above scalings in the **u**-continuity relation immediately gives the requirement

$$\frac{WL}{UH} \backsim 1 \ . \tag{B.4}$$

Again using B.3, and expansions for ρ, the density-continuity relation becomes (after dividing by ρ_0/T)

$$\alpha\frac{\partial\rho'}{\partial t} + \alpha\gamma\mathbf{u}\cdot\boldsymbol{\nabla}\rho' + \gamma\varepsilon w\frac{d\overline{\rho}}{dz} = 0 \ ,$$

where we have defined $\varepsilon = \frac{\triangle\rho}{\rho_0}$ and the normalized amplitude

$$\gamma \equiv \frac{UT}{L} \backsim \frac{WT}{H} \backsim \frac{|\zeta|}{H} \ ,$$

using the fact that $w = \partial\zeta/\partial t$ ($WT \sim |\zeta|$). Note that the leading-order balance in the continuity equation requires $\alpha \backsim \gamma\varepsilon$ (i.e. the isopycnal fluctuations scale on the wave motion as $\rho_0\alpha \sim$

$\triangle\rho\frac{\overline{\eta}}{H}$). Turning next to the momentum equations, applying B.3 and dividing by $\rho_0 U/T$ gives

$$\begin{aligned}(\overline{\rho}+\varepsilon\gamma\rho)\left[\frac{\partial \mathbf{u}_h}{\partial t}+\gamma\mathbf{u}\cdot\boldsymbol{\nabla}\mathbf{u}_h\right] &= -\frac{\varepsilon\gamma^2}{F^2}\boldsymbol{\nabla}_h P \\ \mu^2(\overline{\rho}+\varepsilon\gamma\rho)\left[\frac{\partial w}{\partial t}+\gamma\mathbf{u}\cdot\boldsymbol{\nabla}w\right] &= -\frac{\varepsilon\gamma^2}{F^2}\left(\frac{\partial P}{\partial z}+\rho\right)-\frac{\gamma}{F^2}\left(\frac{d\overline{P}}{dz}+\overline{\rho}\right)\ ,\end{aligned} \tag{B.5}$$

writing the horizontal ($\mathbf{u}_h=(u,v)$, $\boldsymbol{\nabla}_h=(\partial/\partial dx,\partial/\partial dy)$) and vertical equations separately. Here we have defined the Froude number $F\equiv U/c_s$ (with $c_s^2=gH$ the shallow water surface wave speed) and the aspect ratio $\mu\equiv H/L$ ($\backsim W/U$). We next discuss the values of these parameters.

B.1 The parameters μ, ε, γ, and F_i

The four small parameters introduced above are

$$\mu=\frac{H}{L}\qquad \varepsilon=\frac{\triangle\rho}{\rho_0}\qquad \gamma=\frac{\overline{\eta}}{H}\qquad F_i=\frac{F}{\sqrt{\varepsilon}}=\frac{U}{\sqrt{g\varepsilon H}}\ ,$$

where F_i is an effective internal Froude number. For basin-scale motions, H and L scale on the depth and length of the lake, respectively, and thus the aspect ratio $\mu\ll 1$ in general. The normalized density difference $\frac{\triangle\rho}{\rho_0}$ is also small for natural systems, and especially for lakes, where the stratification is commonly due to thermal effects alone. For example, in the UML in midsummer the temperature in the mixed layer reaches approximately 28°C ($\sim$997 kg/m^3), while the hypolimnion remains at about 6°C (1000 kg/m^3). And regarding γ, while the spatial features of the wave motion are governed by the bathymetrey and stratification of the lake, the amplitude of the seiche (which might not be small) is ultimately determined by the strength of the wind forcing. For example, for a two-layer fluid system (with upper layer depth h_1) in a rectangular basin ($L\times H$), the maximum steady-state linear displacement of the interface due to steady forcing $\tau=\rho u_*^2$ is

$$\eta_{\max}=\frac{Lu_*^2}{2g\varepsilon h_1}\ ,$$

which occurs at the sides of the basin. Note that $W = \frac{2\eta_{max}}{h_1}$ is the Wedderburn number (Thompson and Imberger, 1980), a dimensionless parameter which describes upwelling potential.

From the above arguments, we see that the parameters μ, ε, γ are effectively independent of one another, and as such there are no mutually-imposed conditions on their values. On the other hand, the Froude number must be a function of $(\mu, \varepsilon, \gamma)$. To determine the relationship we turn again to the two-layer system. For the homogeneous system (i.e. no forcing), the eigensolution for the fluid velocity u_n in each layer $n = 1, 2$ (with thickness h_1 and h_2) is related to the interface displacement amplitude ζ by

$$|u_n| = c\frac{|\zeta|}{h_n} \sim \gamma \frac{\sqrt{h_1 h_2}}{h_n}\sqrt{g\varepsilon H} \ ,$$

where we have used the internal wave phase speed $c^2 = g\varepsilon\frac{h_1 h_2}{H}$ and the scaling $|\zeta| \backsim H\gamma$ from above. The Froude number is therefore

$$F_i = \frac{U}{\sqrt{g\varepsilon H}} \sim \gamma \frac{\sqrt{h_1 h_2}}{h_n} \sim \gamma \ . \tag{B.6}$$

Returning now to the momentum equations B.5, the leading-order terms (in the z-equation) satisfy the hydrostatic balance (in dimensional form)

$$\frac{d\overline{P}}{dz} = -\overline{\rho}g \ ,$$

and can therefore be eliminated from the dynamic equations. At next order, the acceleration and advection terms are much smaller in the z-equation than in the horizontal equations ($\mu^2 \ll 1$), and could justifiably be neglected ($\partial w/\partial t = 0$ corresponds to the hydrostatic approximation). However, recognizing that L scales on the 'horizontal wavelength' of a given internal seiche mode, these terms may in fact be much larger for higher horizontal modes. In addition, retaining the vertical acceleration does not alter the difficulty of the numerical problem. For these reasons, and simply for the sake of avoiding the hydrostatic approximation, $\partial w/\partial t$ is retained. Finally,

recalling B.6 the governing equations are

$$\begin{aligned}(\overline{\rho}+\varepsilon\gamma\rho)\left[\frac{\partial \mathbf{u}}{\partial t}+\gamma\mathbf{u}\cdot\boldsymbol{\nabla}\mathbf{u}\right] &= -\boldsymbol{\nabla}P-\rho\mathbf{k} \\ \frac{\partial \rho}{\partial t}+\gamma\mathbf{u}\cdot\boldsymbol{\nabla}\rho+w\frac{d\overline{\rho}}{dz} &= 0 \qquad \boldsymbol{\nabla}\cdot\mathbf{u}=0\ .\end{aligned} \tag{B.7}$$

Fully linearized equations follow from B.7 from the simple requirement that the wave amplitude is small $\gamma \ll 1$.

B.2 Internal wave energies (linear, inviscid)

Using the relationship between the vertical velocity and displacement fields $w = \partial\zeta/\partial t$, the linearized density-continuity relation (from B.7) can be integrated with respect to time, giving the relation between the density and isopycnal deviations

$$\rho' = -\overline{\rho}_z\zeta\ . \tag{B.8}$$

Next, multiplying the linearized momentum equations (B.7, in dimensional form) by $\mathbf{u}$ gives

$$\frac{\partial}{\partial t}\left(\frac{1}{2}\overline{\rho}\mathbf{u}^2\right) = -\boldsymbol{\nabla}\cdot(\mathbf{u}P) - g\rho' w\mathbf{k}\ , \tag{B.9}$$

after invoking $\mathbf{u}$-continuity to rearrange the pressure terms. Defining the kinetic and potential energies per unit volume

$$\mathcal{E}_{kin}(\mathbf{x},t) \equiv \frac{1}{2}\overline{\rho}\mathbf{u}^2 \qquad \mathcal{E}_{pot}(\mathbf{x},t) \equiv \int g\rho' w dt \tag{B.10}$$

and the energy flux density

$$\Phi(\mathbf{x},t) \equiv \mathbf{u}P\ ,$$

we see that B.9 corresponds to an energy continuity relation,

$$\frac{\partial \mathcal{E}}{\partial t} + \boldsymbol{\nabla}\cdot\Phi = 0\ , \tag{B.11}$$

with $\mathcal{E} = \mathcal{E}_{kin} + \mathcal{E}_{pot}$ the total energy for a linear, inviscid system. For a lake, if we integrate B.11 over the lake volume Ω, using Gauss' theorem to rearrange the divergence term, we find

$$\frac{d}{dt}\int_{\Omega} \mathcal{E} dV = 0 \ ,$$

since $\mathbf{n} \cdot \Phi|_{\partial} = 0$ (i.e. $\mathbf{n} \cdot \mathbf{u}|_{\partial} = 0$) on all boundaries (in the inviscid formulation). This shows that, in the absence of friction, the total energy of the seiche is conserved over time.

For progressive waves in open systems, the energy densities in B.10 are typically integrated over a wave period or wavelength to yield more useful averaged quantities. Since the t and $\mathbf{x}$ coordinates are coupled in characteristics ($\mathbf{k} \cdot \mathbf{x} \pm ct$), these averaged energies are generally independent of both time and horizontal position (with integration over either time or horizontal space giving the same result). This is not the case for seiches, however, for which the time and space coordinates may be separated. The above energies may thus be integrated over either t or $\mathbf{x}$ separately, yielding useful information about the spatial distribution of energy (or temporal evolution when viscosity is included).

Since we are interested in wave solutions, we now explicity specify a sinusoidal temporal variation for the fields $f = (\mathbf{u}, \rho', P')$:

$$f(\mathbf{x}, t) \rightarrow \mathrm{Re}\left[f(\mathbf{x}) e^{i\omega t}\right] \ , \tag{B.12}$$

with ω the internal seiche frequency. Hereinafter the primes on the dynamic fields are dropped for convenience. Using B.8 and the definition of the buoyancy frequency $N^2 = -g/\overline{\rho}\, d\overline{\rho}/dz$, we also define the energies

$$E_{kin}(\mathbf{x}) = \frac{1}{2}\overline{\rho}\mathbf{u}^2(\mathbf{x}) \qquad E_{pot}(\mathbf{x}) = g\rho w = \frac{1}{2}\overline{\rho}\frac{N^2}{\omega^2}w^2 \ ,$$

such that (including an unspecified phase ϕ)

$$\mathcal{E}_{kin}(\mathbf{x}, t) = E_{kin}(\mathbf{x})\left(\mathrm{Re}\left[e^{i(\omega t+\phi)}\right]\right)^2 \qquad \mathcal{E}_{pot}(\mathbf{x}, t) = E_{pot}(\mathbf{x})\left(\mathrm{Re}\left[ie^{i(\omega t+\phi)}\right]\right)^2 \ .$$

Note that the total energy density $\mathcal{E} = \mathcal{E}_{kin} + \mathcal{E}_{pot}$ at any given location within the fluid is not constant over time, since $E_{kin}(\mathbf{x}) \neq E_{pot}(\mathbf{x})$ in general. However, integrating the total energy

over the lake volume gives

$$E(t) = \int_\Omega \mathcal{E} dV = \int_\Omega E_{kin}(\mathbf{x})\, dV \cos^2(\omega t + \phi) + \int_\Omega E_{pot}(\mathbf{x})\, dV \sin^2(\omega t + \phi) \ .$$

In order for this quantity to remain constant, as determined above, we must have

$$E = \int_\Omega E_{kin}(\mathbf{x})\, dV = \int_\Omega E_{pot}(\mathbf{x})\, dV = \text{constant} \ . \tag{B.13}$$

This effectively corresponds to energy equipartition for standing waves in a basin. While the total energy in the system remains constant, the distribution of energy oscillates between kinetic and potential, 180° out of phase. The energetics of the system resemble a frictionless ball rolling up and down sinusoidal hills, indefinitely exchanging potential energy for kinetic. The analogy of seiches to a harmonic oscillator is therefore obvious.

B.3 Three-dimensional formulation

We now derive the governing equation and boundary conditions for linear internal seiches. Any one of the five fields (u, v, w, g, P) can be isolated in a single equation by eliminating the other four from the linearized governing equations (from B.7). However, to obtain a complete system of governing equation plus boundary conditions for a single field it is necessary to use the dynamic pressure P, since this is the only function whose boundary conditions can be expressed in terms of itself alone (consider the no-flux condition $\mathbf{n} \cdot \mathbf{u}|_\partial = 0$, which couples the velocity equations).

Begin by eliminating ρ $(= i\omega\overline{\rho}N^2 w/g)$ from the momentum equations and rearranging,

$$i\omega \frac{1}{\overline{\rho}} \nabla P = \omega^2 \mathbf{u} - N^2 w \mathbf{k} \ . \tag{B.14}$$

Replacing the velocities in the $\mathbf{u}$-continuity relation (i.e. $\nabla \cdot \mathbf{u} = 0$) then gives the governing equation

$$\nabla_h^2 P - \overline{\rho} \frac{\partial}{\partial z} \left(\frac{1}{\overline{\rho}} \frac{\omega^2}{N^2 - \omega^2} \frac{\partial P}{\partial z} \right) = 0 \ , \tag{B.15}$$

where we have defined the horizontal Laplacian

$$\nabla_h^2 \equiv \frac{\partial^2}{\partial x^2} + \frac{\partial^2}{\partial y^2} \ .$$

The boundary conditions are derived from the no-flux requirement on the velocities, again using B.14;

$$\mathbf{n} \cdot \mathbf{u} = 0 \quad \rightarrow \quad \Gamma P \equiv \mathbf{n}_h \cdot \nabla_h P - n_z \frac{\omega^2}{N^2 - \omega^2} \frac{\partial P}{\partial z} = 0 \tag{B.16}$$

on ∂, where $\mathbf{n}_h = (n_x, n_y)$. It is convenient to set

$$\gamma(z) \equiv \frac{1}{\overline{\rho}} \frac{1}{N^2 - \omega^2}$$

in B.15 and in the discussion of orthogonalities presented below. Finally, at the free surface $z = \zeta_s$ there is a deviation in the pressure due to the displacement of the surface itself. The dynamic pressure P at the surface is given by

$$P(\zeta_s) = g\overline{\rho}(\zeta_s)\zeta_s \ .$$

Employing the fact that $w(\zeta_s) = i\omega\zeta_s$, this equation can be combined with the z-momentum equation in B.14 to give

$$\frac{\partial P}{\partial z} + \frac{N^2 - \omega^2}{g} P = 0 \ . \tag{B.17}$$

If the rigid lid approximation $w(\zeta_s) = P(\zeta_s) = 0$ is used, B.17 reduces to $(\partial P/\partial z)_{surface} = 0$, and can be simply incorporated into B.16. Equations B.15, B.16, and B.17 represent the complete system which governs linear internal seiches in 3D. This system is analogous to a Sturm-Liouville system, and admits an infinite set of orthogonal eigensolutions (internal seiche modes) and their corresponding eigenvalues (frequencies).

B.3.1 Orthogonality properties

The eigenmodes P_n can be used in principal to describe the response of a stratified lake to surface wind stress as a Fourier sum, provided the orthogonality properties of these solutions are known. For this reason, and because the orthogonality conditions are also needed to perform the perturbation anlysis in Chapter 5, we now determine the orthogonality conditions on the P_n.

Begining with B.15 for mode n (with corresponding frequency ω_n, and hence γ_n), multiply the equation by P_m^* $(= P_m)$ and integrate over the lake volume,

$$\int_\Omega \frac{1}{\overline{\rho}} P_m \left[\nabla_h^2 P_n - \overline{\rho} \frac{\partial}{\partial z} \left(\omega_n^2 \gamma_n \frac{\partial P_n}{\partial z} \right) \right] dV = 0 \ .$$

The reason for the factor $\overline{\rho}^{-1}$ in this integral becomes apparent later. After rearranging the integrand,

$$\int_\Omega \frac{1}{\overline{\rho}} \left[\nabla_h \cdot (P_m \nabla_h P_n) - \overline{\rho} \frac{\partial}{\partial z} \left(\omega_n^2 \gamma_n P_m \frac{\partial P_n}{\partial z} \right) - \nabla_h P_m \cdot \nabla_h P_n + \overline{\rho} \omega_n^2 \gamma_n \frac{\partial P_m}{\partial z} \frac{\partial P_n}{\partial z} \right] dV \ , \tag{B.18}$$

the first two terms can be converted into a surface integral using Gauss' theorem,

$$\int_\partial \frac{1}{\overline{\rho}} P_m \left(\mathbf{n}_h \cdot \nabla_h P - n_z \omega_n^2 \gamma_n \overline{\rho} \frac{\partial P_n}{\partial z} \right) ds = 0 \ .$$

This integral vanishes identically because of the boundary conditions B.16, leaving only the last two terms in B.18. The orthogonality conditions on P are not necessarily obvious at this point (as we shall see in the next section, the 2D streamfunction analysis is somewhat more straightforward). To take the next step, recall that the integrated kinetic and potential energies in the lake must be equal (see B.13). Equation B.18 can be rearranged using the trivial relation

$$\gamma = \gamma^2 \overline{\rho} \left(N^2 - \omega^2 \right) \ ,$$

and then partitioned into the two orthogonality conditions

$$\int_\Omega \frac{1}{2}\overline{\rho}\left(\frac{1}{\omega_n^2}\frac{1}{\overline{\rho}^2}\nabla_h P_m\cdot\nabla_h P_n+\omega_n^2\gamma_n^2\frac{\partial P_m}{\partial z}\frac{\partial P_n}{\partial z}\right)dV = E_n\delta_{nm} \tag{B.19}$$

$$\int_\Omega \frac{1}{2}\overline{\rho}N^2\gamma_n^2\frac{\partial P_m}{\partial z}\frac{\partial P_n}{\partial z}dV = E_n\delta_{nm} \tag{B.20}$$

after dividing by $2\omega_n^2$. Here E_n is the total energy of seiche mode n; these expressions correspond to the integrals of the kinetic ($=\frac{1}{2}\overline{\rho}|\mathbf{u}|^2$) and potential ($=\frac{1}{2}\overline{\rho}\frac{N^2}{\omega^2}w^2$) energies, respectively, and are necessarily equivalent (see B.13).

As a final point, note that the results in this section can be derived much more directly using the same technique employed in Chapter 5. Specifically, since the P-governing equation (B.15) is derived by replacing the velocities with P in the $\mathbf{u}$-continuity relation ($\nabla\cdot\mathbf{u}=0$), the above analysis can also be performed by evaluating the integral

$$\int_\Omega P_m\nabla\cdot\mathbf{u}_n^* dV = 0 \ .$$

Rearranging this and again using Gauss' theorem gives

$$\int_\partial \mathbf{n}\cdot\mathbf{u}_n^* P_m dS - \int_\Omega \nabla P_m\cdot\mathbf{u}^* dV = 0 \ .$$

Eliminating the first integral ($\mathbf{n}\cdot\mathbf{u}_n|_\partial = 0$) and using the momentum equations (B.14) we find

$$\int_\Omega \overline{\rho}\left(\mathbf{u}_m\cdot\mathbf{u}_n^* - \frac{N^2}{\omega_m^2}w_m w_n^*\right)dV = 0 \ .$$

Written in this form the orthogonality conditions are readily apparent; interchanging $m\leftrightarrow n$ and subtracting the new equation from the original yields (with $\mathbf{u}=\mathbf{u}^*$, $\omega=\omega^*$)

$$\left(\frac{1}{\omega_m^2}-\frac{1}{\omega_n^2}\right)\int_\Omega \overline{\rho}N^2 w_m w_n dV = 0 \ .$$

If $m=n$ this expression vanishes trivially. On the other hand, if $m\neq n$ the integral itself must vanish. This can be summarized in the orthogonality conditions (normalized to correspond to

the energy)

$$\int_\Omega \frac{1}{2}\overline{\rho}\frac{N^2}{\omega_m^2} w_m w_n dV = E_m \delta_{mn} \qquad \int_\Omega \frac{1}{2}\overline{\rho}\mathbf{u}_m \cdot \mathbf{u}_n dV = E_m \delta_{mn} \ ,$$

from which we retrieve B.19 and B.20 by replacing the $\mathbf{u}$ with P (using B.14).

B.4 Two-dimensional formulation

For realistic lake models (i.e. descriptions of stratification and bathymetry), it is difficult to obtain numerical solutions to the full 3D problem (equations B.15 and B.16), for reasons outlined in Appendix C. Because of these difficulties, and because we are primarily interested in longitudinal seiches, a 2D formulation is used throughout most of this thesis. Some of the strengths and limitations of this approach are explored in Chapter 2, when model solutions for the Upper Mystic Lake are compared to field data (§ 2.4).

In two dimensions ((horizontal, vertical) $= (x, z)$), a formulation for internal seiches can be derived using a streamfunction $\psi(x, z)$ for the velocity field,

$$(u, w) = \mathrm{Re}\left[\left(\frac{\partial \psi}{\partial z}, -\frac{\partial \psi}{\partial x}\right) e^{i\omega t}\right] \ .$$

Replacing the velocities with ψ, the momentum equations become

$$i\omega\overline{\rho}\frac{\partial \psi}{\partial z} = -\frac{\partial P}{\partial x} \qquad i\omega\overline{\rho}\frac{\partial \psi}{\partial x} = \frac{\partial P}{\partial x} + g\rho \ .$$

The pressure can be eliminated from this pair by cross-differentiating ($\partial/\partial z$ on the x-equation and $\partial/\partial x$ on the z-equation) and adding. Finally, replacing the density with (see B.7 or B.8)

$$i\omega\rho = \frac{d\overline{\rho}}{dz}\frac{\partial \psi}{\partial x}$$

gives the 2D seiche governing equation

$$\nabla \cdot (\overline{\rho}\nabla\psi) - \overline{\rho}\frac{N^2}{\omega^2}\frac{\partial^2 \psi}{\partial x^2} = 0 \ , \tag{B.21}$$

where $\nabla = (\partial/\partial x, \partial/\partial z)$.

The boundary conditions for $\psi(x,z)$ are computed from the standard no-flux condition on $\mathbf{u}$. It is somewhat easier to perform this analysis using vector notation. Writing the 2D gradient vector as $\nabla = (\partial/\partial x, 0, \partial/\partial z)$ and the velocity $\mathbf{u} = \nabla \times \psi\mathbf{j} = \nabla\psi \times \mathbf{j}$ (where $\mathbf{j} = \mathbf{k} \times \mathbf{i}$ is the y-unit vector), we find

$$\mathbf{n} \cdot \mathbf{u} = \mathbf{n} \cdot (\nabla\psi \times \mathbf{j}) = -(\mathbf{n} \times \mathbf{j}) \cdot \nabla\psi \ .$$

Since $\mathbf{n} \cdot (\mathbf{n} \times \mathbf{j}) = 0$, we can define $\mathbf{t} \equiv \mathbf{n} \times \mathbf{j}$ as the unit tangent vector to the boundary (i.e. $\mathbf{t}$ is orthogonal to $\mathbf{n}$). The condition $\mathbf{n} \cdot \mathbf{u}|_\partial = 0$ (where ∂ represents the bed plus free surface) therefore becomes

$$\mathbf{t} \cdot \nabla\psi|_\partial = \frac{\partial\psi}{\partial x_t}(0, x_t) = 0 \ .$$

This can simply be integrated to give the Dirichlet condition

$$\psi|_\partial = 0 \ . \tag{B.22}$$

The integration constant is taken as zero without loss of generality.

B.4.1 Orthogonality properties

The orthogonality conditions for the 2D system are computed exactly the same way as in Section B.3.1. Writing B.21 explicity for mode n, and then multiplying by ψ_m^* $(= \psi_m)$ and integrating over the 'volume' of the lake (denoted by Ω; $dV = dxdz$) gives

$$\int_\Omega \left(\psi_m \nabla \cdot (\overline{\rho}\nabla\psi_n) - \overline{\rho}\frac{N^2}{\omega_n^2}\psi_m \frac{\partial^2\psi_n}{\partial x^2} \right) dV = 0 \ .$$

Rearranging and grouping the divergence-type terms gives

$$\int_\Omega \left[\nabla \cdot (\overline{\rho}\psi_m \nabla\psi_n) - \frac{\partial}{\partial x}\left(\overline{\rho}\frac{N^2}{\omega_n^2}\psi_m \frac{\partial\psi_n}{\partial x} \right) - \overline{\rho}\nabla\psi_m \cdot \nabla\psi_n + \overline{\rho}\frac{N^2}{\omega_n^2}\frac{\partial\psi_m}{\partial x}\frac{\partial\psi_n}{\partial x} \right] dV = 0 \ .$$

The first two terms in this integral can be re-expressed as a surface (contour) integral using Gauss' Theorem,

$$\int_{\partial} \overline{\rho}\psi_m \left(\mathbf{n} \cdot \nabla\psi_n - n_x \frac{N^2}{\omega_n^2} \frac{\partial \psi_n}{\partial x} \right) ds = 0 \ ,$$

which vanishes because of the boundary conditions $\psi_m|_{\partial} = 0$. Here s is the boundary coordinate and $\mathbf{n} = (n_x, n_z)$ is the outer unit normal vector at the boundary. This leaves the last two terms

$$\int_{\Omega} \overline{\rho} \nabla\psi_m \cdot \nabla\psi_n dV = \frac{1}{\omega_n^2} \int_{\Omega} \overline{\rho} N^2 \frac{\partial \psi_m}{\partial x} \frac{\partial \psi_n}{\partial x} dV \ .$$

Interchanging the indices $n \leftrightarrow m$ in this expression and subtracting the original gives

$$\left(\frac{1}{\omega_m^2} - \frac{1}{\omega_n^2} \right) \int_{\Omega} \overline{\rho} N^2 \frac{\partial \psi_n}{\partial x} \frac{\partial \psi_m}{\partial x} dV = 0 \ .$$

This relation holds when either the integral vanishes or when $\omega_n = \omega_m$. This can be summarized in the orthogonality condition

$$\int_{\Omega} \overline{\rho} \frac{N^2}{\omega_n^2} \frac{\partial \psi_m}{\partial x} \frac{\partial \psi_n}{\partial x} dx dz = 2E_m \delta_{mn} \ , \tag{B.23}$$

which in turn implies

$$\int_{\Omega} \overline{\rho} \nabla\psi_m \cdot \nabla\psi_n dx dz = 2E_m \delta_{mn} \ . \tag{B.24}$$

Here E_m is the total (and constant) energy of the system for seiche mode m. With $n \rightarrow m$, the integrals in B.23 and B.24 correspond to the total potential and kinetic energies for mode m respectively, which are equal to the total E_m (see B.13).

References

Thompson, R. O. R. Y., and J. Imberger, 1980. Response of a numerical model of a stratified lake to wind stress. *Proc. 2nd Int. Symp. on Stratified Flows*, Trondheim, Norway, Vol. 1, 562-570.

Appendix C

Numerical formulation

C.1 The 2D system

Expanding the ψ-governing equation (B.21) and applying the spatial scalings $x \rightarrow Lx$, $z \rightarrow Hz$ yields

$$\frac{1}{\mu^2}\left(\frac{\partial^2\psi}{\partial z^2} + \frac{N^2}{g}\frac{\partial\psi}{\partial z}\right) + \frac{\partial^2\psi}{\partial x^2} = \frac{N^2}{H\omega^2}\frac{\partial^2\psi}{\partial x^2}$$

(where $\mu = H/L$), provided z is also non-dimensionalized within the buoyancy frequency N. Note that the frequency has been isolated on one side of this equation, allowing the system to be formulated as an eigenvalue problem. Discretizing this expression using central differences gives

$$\frac{1}{\mu^2}\frac{\triangle x^2}{\triangle z^2}\left(\delta_z^2\psi_{ik} + \left(\frac{N_k^2\triangle z}{2g}\right)\delta_{2z}\psi_{ik}\right) + \delta_x^2\psi_{ik} = \frac{N_k^2}{H\omega^2}\delta_x^2\psi_{ik} \ , \tag{C.1}$$

where we have defined $\psi_{ik} \equiv \psi\left(x_i, z_k\right)$, and $\delta_z^2 = \left(\psi_{ik+1} - 2\psi_{ik} + \psi_{ik-1}\right)$, etc. Setting

$$a^2 \equiv \frac{1}{\mu^2}\frac{\triangle x^2}{\triangle z^2} \ , \qquad M_k \equiv \frac{N_k^2\triangle z}{2g} \ ,$$

C.1 becomes

$$\omega^2\left[a^2\left(\delta_z^2\psi_{ik} + M_k\delta_{2z}\psi_{ik}\right) + \delta_x^2\psi_{ik}\right] = H^{-1}N_k^2\delta_x^2\psi_{ik} \ . \tag{C.2}$$

This equation is obviously not scale-independent; changing the aspect ratio μ, and hence a, changes the relative magnitudes of terms on the left-hand side. For lakes, μ^{-1} is so large that the $\delta_x^2\psi_{ik}$ term on the left is often very small relative to the others, and is frequently neglected (corresponding to the hydrostatic approximation, as described in Section B.1).

Finally, when C.2 is combined with the boundary condition $\psi|_\partial = 0$, the complete numerical problem has matrix eigenvalue form

$$\omega^2 \mathbf{M}\boldsymbol{\psi} = \mathbf{N}\boldsymbol{\psi} \ .$$

If either matrices $\mathbf{M}$ or $\mathbf{N}$ has an inverse, as is generally the case for the 2D problem, then this equation can be recast in standard from, eg. $\mathbf{A}\boldsymbol{\psi} = \omega^2\boldsymbol{\psi}$. This numerical formulation therefore yields a finite set of seiche mode solutions and their corresponding frequencies.

C.2 Brief outline of the 3D problem

The 3D numerical problem is considerably more complicated than the 2D ψ-system. To place the P-governing equation 3.10 in a form which can be discretized, we first expand the $\partial/\partial z$ term, and then multiply by $\left(\omega^2 - N^2\right)^2$ to remove all terms in the denominator. Collecting the terms at each order in ω, we have

$$\omega^4 \boldsymbol{\nabla}\cdot(\overline{\rho}\boldsymbol{\nabla}P) - \omega^2\left[2N^2\boldsymbol{\nabla}\cdot(\overline{\rho}\boldsymbol{\nabla}P) - \frac{\partial}{\partial z}\left(\overline{\rho}N^2\frac{\partial P}{\partial z}\right)\right] + \overline{\rho}N^4\nabla_h^2 P = 0 \ , \qquad \text{(C.3)}$$

recalling that $\boldsymbol{\nabla}_h = (\partial/\partial x, \partial/\partial y)$. To complete the matrix formulation the boundary conditions in 3.11 can be incorporated as

$$\omega^2 \mathbf{n}\cdot\boldsymbol{\nabla}P - N^2\mathbf{n}_h\cdot\boldsymbol{\nabla}_h P = 0 \ . \qquad \text{(C.4)}$$

We now outline the difficulties in formulating the system C.3 and C.4 as an eigenvalue problem.

To begin, the governing equation C.3 is quadratic in ω^2. Specifically, the discretized equa-

tions and boundary conditions have the form

$$\left(\omega^4 \mathbf{A} + \omega^2 \mathbf{B} + \mathbf{C}\right) \mathbf{P} = 0 \ , \tag{C.5}$$

and therefore represent a nonlinear eigenvalue problem (dimension $\mathbb{N} \times \mathbb{N}$, say). The problem can be linearized by defining the vector

$$\widehat{\mathbf{P}} = \omega^2 \mathbf{P} \ , \tag{C.6}$$

which, combined with C.5/C.4 gives the $2\mathbb{N} \times 2\mathbb{N}$ system

$$\begin{pmatrix} \mathbf{0} & \mathbf{I} \\ -\mathbf{C} & \mathbf{0} \end{pmatrix} \begin{pmatrix} \mathbf{P} \\ \widehat{\mathbf{P}} \end{pmatrix} = \omega^2 \begin{pmatrix} \mathbf{I} & \mathbf{0} \\ \mathbf{B} & \mathbf{A} \end{pmatrix} \begin{pmatrix} \mathbf{P} \\ \widehat{\mathbf{P}} \end{pmatrix} \ . \tag{C.7}$$

(Note that this is one of two possible choices.) Now, the matrices $\mathbf{A}$, $\mathbf{B}$, and $\mathbf{C}$ are generally singular (i.e. do not have inverses) because the boundary conditions C.4 are Neumann-type. Equation C.7 must therefore be solved as shown rather than in standard form (i.e. $\mathbf{MQ} = \lambda \mathbf{Q}$), thereby requiring a more expensive numerical algorithm. Thus, to summarize, the 3D problem is computationally more difficult than the 2D case because a) there is one additional space dimension to begin with, b) the size of the system must be doubled in order to make it linear, and c) the system must be solved as a generalized eigenvalue problem. These factors make the 3D problem exceedingly difficult to solve; to the author's knowledge it has never been attempted.

C.3 Numerical Code

The following is a finite difference code written in MATLAB© for evaluating solutions to Equation (C.2).

```
%*****************************************
%                  STREAM                 *
%                                         *
% Solve eigenvalue problem for variable   *
% bathymetry, continuous stratification,  *
% using a stream function formulation     *
%                                         *
% Equation:                               *
%  del^2(pF) - p(N^2)/w^2Fxx  = 0         *
% or                                      *
%  Fzz - (N2/g)Fz + Fxx = (N^2/w^2)Fxx    *
%                                         *
% BC: F(boundary) = 0                     *
%                                         *
% Sections:                               *
%  (1) Grid Generation                    *
%  (2) Density Profile                    *
%  (3) Bathymetry, X and Z Boundary Points *
%  (4) X and Z 'Inside' Points            *
%  (5) Coefficients                       *
%  (6) Equation                           *
%  (7) Pack Matrix, Compute Eigenvalues   *
%                                         *
%*****************************************

clear bath bath1 bath2 gridX gridZ Xbm Xbp Xb Xbp1 Xbp2 X Zb Zb1 Zb2
clear rho N2 DELM DELP
clear inm jnm inp jnp inb jnb Im Imm Ip Ipp J
clear dx dxm dxp dxb dz dzm dzp dzb c d C DX Cb Cm Cp D1m D1p D1b D2b D2m D2p
clear A B AP BP CM non0 is0 Vnon0 V D1

%****************************************
%******** (1) GRID GENERATION ********
%****************************************

L = 1000; H = 25;

Nx = 40; Nz = 40;

delX = 1/Nx; delZ = 1/Nz;
mu2 = H^2/L^2;
a2 = (delX/delZ)^2/mu2;

gridX = [0:Nx]/Nx;  gridZ = [0:Nz]/Nz;
GridX = ones(Nz+1,1)*gridX;  GridZ = ones(Nx+1,1)*gridZ;% grid mesh


%****************************************
%************ (2) Density Profile *************
```

```
%*****************************************
%                                        *
% The stratification can be specified using *
% either the density or the buoyancy frequency. *
% This example is constant-linear-constant *
% density profile                        *
%*****************************************

g = 9.81;

dhyp = Nz;
rhoepi = 997;              % epilimnion density
rhohyp = 1000;             % hypolimnion density
delrho = rhohyp-rhoepi;
depi = 5;                  % epilimnion thickness in grid points
dmet = 7;                  % metalimnion thickness in grid points

rho = [rhoepi*ones(1,depi) rhoepi+delrho*[1:dmet]/dmet rhohyp*ones(1,dhyp-dmet-depi-1)];
N2 = [zeros(1,depi) delrho*ones(1,dmet) zeros(1,dhyp-dmet-depi-1)];

DELM = 1+N2/(2*g)*delZ;
DELP = 1-N2/(2*g)*delZ;

Boussinesq = 0;
if Boussinesq == 1
    DELM = ones(1,length(N2));
    DELP = ones(1,length(N2));
end


%************************************************
%***** (3) Bathymetry, X and Z Boundary Points ******
%************************************************
%                                               *
% Xb are the X-boundary points along a given    *
% row 2(Nx+1) of them - the 'centre' value is   *
% is usually duplicated Zb are the Z-boundary   *
% points down a given column (Nz+1) of them     *
%************************************************

% **** Example: Parabolic Basin ****

N = 100;  X = [0:N]/N;      % This is for graphing purposes - not used in this code
bath = 1-4*(X-1/2).^2;

Xbm = 0.5*(1-sqrt(1-gridZ));
Xbp = 0.5*(1+sqrt(1-gridZ));

Xb = [Xbm fliplr(Xbp)];
```

```
Zb = 1-(1 - 2*gridX).^2;


%*****************************************
%********* (4) X and Z 'Inside' Points ***********
%*****************************************
%                                                *
% The following points are a fractional distance  *
% from the bed, either in x, or in z, or in both  *
%                                                *
% inm,jnm - X,Z indices, left side (minus)        *
% inp,jnp - X,Z indices, right side (plus)        *
% inb,jnb - X,Z indices, bed                      *
%                                                *
% Im -  X indices, left side, 1st grid            *
%   points inside the boundary (Nz)               *
% Ip -  X indices, right side, last               *
%   grid points inside the boundary               *
% J - corresponding Z value (Nz)                  *
%                                                *
% Fractional differences between                  *
% the near-boundary points and the bed            *
%                                                *
% dxm,dzm - left side (minus)                     *
% dxp,dzp - right side (plus)                     *
% dxb,dzb - bed                                   *
%                                                *
%*****************************************

clear indum jndum dxdum dzdum inm jnm Im dxm dzm inp jnp Ip dxp dzp

k = 0; l = 0;
for j = 1:Nz-1
% LEFT
    k = k+1;
    indum = find(gridX == ceil(Nx*Xbm(j))/Nx);
    inm(k) = indum;
    jnm(k) = j;
    dxm(k) = (indum -1) - Nx*Xbm(j);
    dzm(k) = Nz*Zb(indum) - (j-1);
    Im(j) = indum;
    Imm(j) = indum;
    if dzm(k) > 1
        dzm(k) = 1;
    end
    while dzm(k) <= 1
        indum = indum + 1;
        dzdum = Nz*Zb(indum) - (j-1);
```

```
        if dzdum <= 1
            k = k+1;
            inm(k) = indum;
            jnm(k) = j;
            dxm(k) = 1;
            dzm(k) = dzdum;
            Im(j) = indum;
        end
    end

% RIGHT
    l = l+1;
    indum = find(gridX == floor(Nx*Xbp(j))/Nx);
    inp(l) = indum;
    jnp(l) = j;
    dxp(l) = (indum-1) - Nx*Xbp(j);
    dzp(l) = Nz*Zb(indum) - (j-1);
    Ip(j) = indum;
    Ipp(j) = indum;
    if dzp(l) > 1
        dzp(l) = 1;
    end
    while dzp(l) <= 1
        indum = indum - 1;
        dzdum = Nz*Zb(indum) - (j-1);
        if dzdum <= 1
            l = l+1;
            inp(l) = indum;
            jnp(l) = j;
            dxp(l) = -1;
            dzp(l) = dzdum;
            Ip(j) = indum;
        end
    end
    J(j)=j;
end

% ******* Vertical scan of second-to-last row *******
j = Nz;      % just a reminder
clear dxb dzb inb jnb
% Bottom LEFT
indumm = find(gridX == ceil(Nx*Xbm(j))/Nx);
indump = find(gridX == floor(Nx*Xbp(j))/Nx);

Imm(j) = indumm;
Ipp(j) = indump;
k = 1;
inb(k) = indumm;
jnb(k) = j;
```

```
dxb(k) = (gridX(indumm)-Xbm(j))*Nx;
dzb(k) = (Zb(indumm) - (Nz-1)/Nz)*Nz;
for i = indumm+1:indump-1
    k = k+1;
    dxb(k) = 1;
    dzb(k) = (Zb(i) - (Nz-1)/Nz)*Nz;
    inb(k) = i;
    jnb(k) = Nz;
end
k = k+1;
inb(k) = indump;
jnb(k) = j;
dxb(k) = (gridX(indump)-Xbp(j))*Nx;
dzb(k) = (Zb(indump) - (Nz-1)/Nz)*Nz;

clear GridX GridZ

%*********************************************
%************* (5) Coefficients ******************
%*********************************************
%                                                *
% The fractional differences dx/dx are used to write  *
% finite difference expressions for Uzz, Uz, Uxx.     *
% The coefficients are arrange in matrices:           *
% Cm,Cp,Cb - coefficients for Uxx                     *
% D2m,D2p,D2b - coefficients for Uzz                  *
% D1m,D1p,D2b - coefficients for Uz                   *
%                                                *
%*********************************************
clear Cm Cp Cb D2m D2p D2b D1m D1p D1b

k = dxm';
Cm(:,1:4) = [6./(k.*(k+1).*(k+2)) (k-3)./k -2*(k-2)./(k+1) (k-1)./(k+2)];

k = -dxp';
Cp(:,1:4) = [(k-1)./(k+2) -2*(k-2)./(k+1) (k-3)./k 6./(k.*(k+1).*(k+2))];

k = dxb(1:length(dxb)-1)';
Cb(:,1:4) = [6./(k.*(k+1).*(k+2)) (k-3)./k -2*(k-2)./(k+1) (k-1)./(k+2)];

k = -dxb(length(dxb));
Cb(length(dxb),1:4) = [(k-1)/(k+2) -2*(k-2)/(k+1) (k-3)/k 6/(k*(k+1)*(k+2))];

k = dzm';
a = 1./(k.*(k+ones(length(k),1)));
b = [-k.^2 k.^2-ones(length(k),1) ones(length(k),1)];
D1m(:,1:3) = [a.*b(:,1) a.*b(:,2) a.*b(:,3)];
D2m(:,1:4) = [6./(k.*(k+1).*(k+2)) (k-3)./k -2*(k-2)./(k+1) (k-1)./(k+2)];
```

```
k = dzp';
a = 1./(k.*(k+ones(length(k),1)));
b = [-k.^2 k.^2-ones(length(k),1) ones(length(k),1)];
D1p(:,1:3) = [a.*b(:,1) a.*b(:,2) a.*b(:,3)];
D2p(:,1:4) = [6./(k.*(k+1).*(k+2)) (k-3)./k -2*(k-2)./(k+1) (k-1)./(k+2)];

k = dzb';
a = 1./(k.*(k+ones(length(k),1)));
b = [-k.^2 k.^2-ones(length(k),1) ones(length(k),1)];
D1b(:,1:3) = [a.*b(:,1) a.*b(:,2) a.*b(:,3)];
D2b(:,1:4) = [6./(k.*(k+1).*(k+2)) (k-3)./k -2*(k-2)./(k+1) (k-1)./(k+2)];

%***********************************************
%***************** (6) Equation ****************
%***********************************************
%                                              *
% The interior points are done first.          *
% Then the boundary points are added.          *
%                                              *
%***********************************************

%preallocate

A = sparse(zeros((Nx+1)*(Nz+1),(Nx+1)*(Nz+1)));
B = sparse(zeros((Nx+1)*(Nz+1),(Nx+1)*(Nz+1)));

% Hydrostatic approximation when r = 0

r = 1;

% ************* body (rows 2 to Nz-1) *************

for j = 2:Nz-1
    for i = Im(J(j))+1:Ip(J(j))-1
        A((j-1)*(Nx+1)+i,(j-2)*(Nx+1)+i) = a2*DELM(j);   % for j=2, this point is deleted when
        A((j-1)*(Nx+1)+i,(j-1)*(Nx+1)+i-1) = r;          % the matrix is packed
        A((j-1)*(Nx+1)+i,(j-1)*(Nx+1)+i) = -2*(r+a2);
        A((j-1)*(Nx+1)+i,(j-1)*(Nx+1)+i+1) = r;
        A((j-1)*(Nx+1)+i,(j)*(Nx+1)+i) = a2*DELP(j);

        B((j-1)*(Nx+1)+i,(j-1)*(Nx+1)+i-1) = N2(j);
        B((j-1)*(Nx+1)+i,(j-1)*(Nx+1)+i) = -2*N2(j);
        B((j-1)*(Nx+1)+i,(j-1)*(Nx+1)+i+1) = N2(j);
    end
end

% ************* left (rows 2 to Nz-1) *************

for j = 2:length(jnm)
```

```
    if jnm(j) > 2
        A((jnm(j)-1)*(Nx+1)+inm(j),(jnm(j)-3)*(Nx+1)+inm(j)) = D2m(j,4)*a2;
    end
    A((jnm(j)-1)*(Nx+1)+inm(j),(jnm(j)-2)*(Nx+1)+inm(j)) =
                    a2*(D2m(j,3)+N2(jnm(j))/g*delZ*D1m(j,3));
    A((jnm(j)-1)*(Nx+1)+inm(j),(jnm(j)-1)*(Nx+1)+inm(j)) =
                    r*Cm(j,2)+a2*(D2m(j,2)+N2(jnm(j))/g*delZ*D1m(j,2));
    A((jnm(j)-1)*(Nx+1)+inm(j),(jnm(j)-1)*(Nx+1)+inm(j)+1) = r*Cm(j,3);
    A((jnm(j)-1)*(Nx+1)+inm(j),(jnm(j)-1)*(Nx+1)+inm(j)+2) = r*Cm(j,4);
    A((jnm(j)-1)*(Nx+1)+inm(j),(jnm(j))*(Nx+1)+inm(j)) =
                    a2*(D2m(j,1)+N2(jnm(j))/g*delZ*D1m(j,1));

    B((jnm(j)-1)*(Nx+1)+inm(j),(jnm(j)-1)*(Nx+1)+inm(j)) = Cm(j,2)*N2(jnm(j));
    B((jnm(j)-1)*(Nx+1)+inm(j),(jnm(j)-1)*(Nx+1)+inm(j)+1) = Cm(j,3)*N2(jnm(j));
    B((jnm(j)-1)*(Nx+1)+inm(j),(jnm(j)-1)*(Nx+1)+inm(j)+2) = Cm(j,4)*N2(jnm(j));
end

% ************* right (rows 2 to Nz-1) *************

for j = 2:length(jnp)
    if jnp(j) > 2
        A((jnp(j)-1)*(Nx+1)+inp(j),(jnp(j)-3)*(Nx+1)+inp(j)) = D2p(j,4)*a2;
    end
    A((jnp(j)-1)*(Nx+1)+inp(j),(jnp(j)-2)*(Nx+1)+inp(j)) =
                    a2*(D2p(j,3)+N2(jnp(j))/g*delZ*D1p(j,3));
    A((jnp(j)-1)*(Nx+1)+inp(j),(jnp(j)-1)*(Nx+1)+inp(j)-2) = r*Cp(j,1);
    A((jnp(j)-1)*(Nx+1)+inp(j),(jnp(j)-1)*(Nx+1)+inp(j)-1) = r*Cp(j,2);
    A((jnp(j)-1)*(Nx+1)+inp(j),(jnp(j)-1)*(Nx+1)+inp(j)) =
                    r*Cp(j,3)+a2*(D2p(j,2)+N2(jnp(j))/g*delZ*D1p(j,2));
    A((jnp(j)-1)*(Nx+1)+inp(j),(jnp(j))*(Nx+1)+inp(j)) =
                    a2*(D2p(j,1)+N2(jnp(j))/g*delZ*D1p(j,1));

    B((jnp(j)-1)*(Nx+1)+inp(j),(jnp(j)-1)*(Nx+1)+inp(j)-2) = Cp(j,1)*N2(jnp(j));
    B((jnp(j)-1)*(Nx+1)+inp(j),(jnp(j)-1)*(Nx+1)+inp(j)-1) = Cp(j,2)*N2(jnp(j));
    B((jnp(j)-1)*(Nx+1)+inp(j),(jnp(j)-1)*(Nx+1)+inp(j)) = Cp(j,3)*N2(jnp(j));
end

% ************* second-to-last row **************

%j = Nz
for i = 1:length(inb)-1
    base = (Nz-1)*(Nx+1);
    A(base+inb(i),(Nz-3)*(Nx+1)+inb(i)) = D2b(i,4)*a2;
    A(base+inb(i),(Nz-2)*(Nx+1)+inb(i)) = a2*(D2b(i,3)+N2(Nz)/g*delZ*D1b(i,3));
    A(base+inb(i),(Nz-1)*(Nx+1)+inb(i)-1) = r*Cb(i,1);
    A(base+inb(i),(Nz-1)*(Nx+1)+inb(i)) = r*Cb(i,2)+a2*(D2b(i,2)+N2(Nz)/g*delZ*D1b(i,2));
    A(base+inb(i),(Nz-1)*(Nx+1)+inb(i)+1) = r*Cb(i,3);
    A(base+inb(i),(Nz-1)*(Nx+1)+inb(i)+2) = r*Cb(i,4);
```

```
    B(base+inb(i),(Nz-1)*(Nx+1)+inb(i)-1) = Cb(i,1)*N2(Nz);
    B(base+inb(i),(Nz-1)*(Nx+1)+inb(i)) = Cb(i,2)*N2(Nz);
    B(base+inb(i),(Nz-1)*(Nx+1)+inb(i)+1) = Cb(i,3)*N2(Nz);
    B(base+inb(i),(Nz-1)*(Nx+1)+inb(i)+2) = Cb(i,4)*N2(Nz);
end

% very last point
i = length(inb);
A(base+inb(i),(Nz-3)*(Nx+1)+inb(i)) = D2b(i,4)*a2;
A(base+inb(i),(Nz-2)*(Nx+1)+inb(i)) = a2*(D2b(i,3)+N2(Nz)/g*delZ*D1b(i,3));
A(base+inb(i),(Nz-1)*(Nx+1)+inb(i)-1) = r*Cb(i,4);
A(base+inb(i),(Nz-1)*(Nx+1)+inb(i)) = r*Cb(i,3)+a2*(D2b(i,2)+N2(Nz)/g*delZ*D1b(i,2));
A(base+inb(i),(Nz-1)*(Nx+1)+inb(i)+1) = r*Cb(i,2);
A(base+inb(i),(Nz-1)*(Nx+1)+inb(i)+2) = r*Cb(i,1);

B(base+inb(i),(Nz-1)*(Nx+1)+inb(i)-1) = Cb(i,4)*N2(Nz);
B(base+inb(i),(Nz-1)*(Nx+1)+inb(i)) = Cb(i,3)*N2(Nz);
B(base+inb(i),(Nz-1)*(Nx+1)+inb(i)+1) = Cb(i,2)*N2(Nz);
B(base+inb(i),(Nz-1)*(Nx+1)+inb(i)+2) = Cb(i,1)*N2(Nz);


%*****************************************
%************* (7) Pack Matrix, *************
%********** Compute Eigenvalues ************
%*****************************************

non0 = find(diag(A) ~= 0);      % find non-zero diagonals
is0 = find(diag(A) == 0);       % find zero diagonals

AP = A(non0,non0);
BP = B(non0,non0);

CM = full(AP\BP);
[V,D] = eig(CM);
clear CM            % save space

for i = 1:length(D)  % move eigenvalues to a vector
  l(i) = D(i,i);     % the l(i) correspond to omega^2
end

clear D
```